

# DEVELOPMENT OF A PROTON INDUCED X-RAY EMISSION (PIXE) MATERIAL ANALYSIS SYSTEM

By

James William Eisenmann III

May 2019

Director of Thesis: Jefferson L. Shinsaugh, PhD

Major Department: Physics

A material analysis system using particle-induced x-ray emission (PIXE) has been developed to measure trace element composition in a wide range of samples. The system was constructed in the particle accelerator laboratory in the Department of Physics at East Carolina University, and includes a new high-vacuum beamline on the 2-million-volt tandem Pelletron ion accelerator, which utilizes a modified multi-sample target chamber.

PIXE analysis can provide sensitivities to the parts-per-million level or better for many elements. In this method, a sample is irradiated with protons in the energy range of 1 – 3 MeV from the particle accelerator. Characteristic x-rays emitted from the sample are detected with an x-ray spectrometer, and the emission spectrum is fit using known spectral line energies to determine the energy calibration of the system. The PIXE analysis system was then tested by analyzing various sample materials –

including pure elements and multielement compounds – that ultimately confirmed the validity of the system.



DEVELOPMENT OF A PROTON INDUCED X-RAY EMISSION (PIXE)  
MATERIAL ANALYSIS SYSTEM

A Thesis Presented to  
the Faculty of the Department of Physics  
East Carolina University

In Partial Fulfillment  
Of the Requirements for the Degree  
Master of Science in Physics

By  
James William Eisenmann III

May 2019

© James William Eisenmann III, 2019

DEVELOPMENT OF A PROTON INDUCED X-RAY EMISSION (PIXE)  
MATERIAL ANALYSIS SYSTEM

by

James William Eisenmann III

APPROVED BY:

DIRECTOR OF THESIS:

\_\_\_\_\_  
Jefferson Shinpaugh, PhD

COMMITTEE MEMBER:

\_\_\_\_\_  
Regina DeWitt, PhD

COMMITTEE MEMBER:

\_\_\_\_\_  
Michael Dingfelder, PhD

COMMITTEE MEMBER:

\_\_\_\_\_  
Eli Hvastkovs, PhD

CHAIR OF THE DEPARTMENT OF PHYSICS:

\_\_\_\_\_  
Jefferson Shinpaugh, PhD

DEAN OF THE GRADUATE SCHOOL: \_\_\_\_\_

Paul J. Gemperline, PhD

## Acknowledgments

I would like to extend my great appreciation, admiration, and thanks to Dr. Jefferson Shinpaugh. The tumult of working on this project was buffered by his extensive knowledge of particle physics; without his guidance none of this would have been possible. Problems that we faced were always met with his calm, poised, and sincerely polite demeanor, and his effective resolutions were always made quickly and decisively. I have gleaned wise counsel from Dr. Shinpaugh academically and personally, and I consider it a privilege to have had the opportunity to work so closely with him.

I am particularly grateful to Dr. Regina DeWitt, and Dr. Eli Hvastakovs for agreeing to be members of my thesis committee. Without their feedback this thesis would not be as polished as it is.

I thank Dr. Michael Dingfelder for his paternal-like guidance and advice. As one of my professors, he taught me multitudes about our universe. As my advisor, he continually kept me on track, he always listened even when he was overburdened with his own responsibilities, and he always went out of his way to keep me on my feet. He really made my journey through graduate school a much smoother ride.

My thanks to Chris Bonnerup, William Holland, and Gene Riggs. I learned a lot from these gentlemen. They were always there to understand my ideas, challenge them, then bring them to fruition. These are all extremely talented men, they are an asset to ECU's physics department, and I absolutely respect everything that they do.

I need to specifically mention Wilson Hawkins and Dr. Eric Maertz, both men offered some of the most expert and insightful guidance that I received during my time in the lab, and I would like to thank them for generously offering their time, expertise, and guidance.

Next, I would like to thank my teacher, advisor, and friend Dr. Martin Bier. As my professor, he was continually patient with me, and he was always there to offer guidance and support – especially during some of the most difficult years of my life. Dr. Bier taught me some of the most interesting and important things that I will ever know. He also convinced me to make a major life decision that ultimately got me to this point. For all these things I will be endlessly grateful.

I also wish to offer my sincere gratitude to Whitney Spivey. Whitney motivated me and helped me with this work; she is a genuine inspiration. She is brilliant, lovely, and a joy to be with. She refines me, focuses me, compliments me, but most of all she makes me absolutely happy. The words “thank you” are simply not enough in expressing my appreciation for her.

Finally, I would like to thank Ocean Elissa Eisenmann, my daughter. I settled upon this path because I thought she would have a better life if I did. She indirectly drove my efforts; she was, and is, my primary driving force in life. She is a smart, beautiful, empathetic, funny, and, truly, a kind person. She makes me completely proud that I am her father. A wish for a more perfect child would never be granted, because I already have her. Ocean is the love of my life, and that will remain true forever.

## TABLE OF CONTENTS

LIST OF TABLES.....	<i>ix</i>
LIST OF FIGURES.....	<i>x</i>
1. Introduction.....	1
1.1 XRF and an Introduction to PIXE.....	1
1.2 History.....	3
1.3 PIXE.....	6
1.3.1 Quantum Numbers.....	6
1.3.2 Transitions.....	8
1.3.3 Detection Limits.....	17
1.3.4 Fluorescent Yields.....	17
1.3.5 Ionization Cross Sections.....	22
1.3.6 Spectral Background.....	23
1.3.7 Mechanical, Electrical, and Thermal Noise.....	27
1.3.8 Sample Composition and Attenuation.....	30
2. Experimental Methods.....	35
2.1 Proton Beam Creation.....	35
2.1.1 Cesium Sputter Source.....	35
2.1.2 Pelletron Tandem Particle Accelerator.....	42
2.1.3 PIXE Beam Requirements.....	51
2.2 Target Chamber.....	52

2.2.1 Chamber Specifications.....	52
2.2.2 Chamber Monitoring.....	63
2.2.3 Collimators.....	65
2.2.4 Detector Positioning.....	66
2.3 XR-100 Fast Silicon Drift Diode Detector.....	66
2.3.1 SDD Detector Theory and Operation.....	67
2.3.2 Temperature Control.....	70
2.3.3 Resolution.....	72
2.3.4 Efficiency.....	75
2.3.5 Multi-Layer Collimator.....	79
2.3.6 PX5 Digital Pulse Processor.....	79
2.3.7 Energy Calibration.....	81
2.3.7.1 Pulse Shaping.....	87
2.3.7.2 PX5 Electronics.....	89
2.3.8 Detector Specifications and Construction.....	90
2.3.9 Data Display and Analysis.....	93
2.3.10 Electrical and Software Interfaces.....	93
2.3.11 System Gain.....	94

2.3.12 Standard Operating Procedure.....	96
3.3.12.1 Energy/Channel Calibration.....	98
3. Results/Discussion.....	99
3.1 Target Chamber Results.....	99
3.2 Fe-55 Spectral Data.....	100
3.3 PIXE Spectral Data.....	114
4. Conclusion.....	121
5. References.....	122

## LIST OF TABLES

1. K shell fluorescent yields (Z= 6-92) .....	20
2. L shell fluorescent yields (experimental).....	21
3. Gamma ray yields for select targets.....	26
4. Proton energy attenuation in air and vacuum.....	50
5. Gain adjustment parameters.....	95
6. Gain eV/Channel.....	108

## LIST OF FIGURES

1. Energy Level Diagram and X-Ray Emission Nomenclature.....	11
2. XRF K shell vacancy.....	12
3. XRF $K_{\alpha}$ transition.....	13
4. XRF $L_{\alpha}$ transition.....	14
5. XRF $L_{\gamma}$ transition.....	15
6. Auger emission.....	16
7. FWHM noise vs. peaking time of SDD.....	29
8. General illustration of PIXE analysis.....	31
9. Diagram of cesium sputter source.....	37
10. Diagram of Particle accelerator and PIXE system.....	41
11. (a – d) Images of exterior of target chamber.....	48-49
12. Bird's eye view of the PIXE target chamber.....	52
13. Image of PIXE Sample Carousel.....	55
14. Image of filter and sample wheels.....	58
15. Electrical diagram of motor and optical interrupter switch.....	60
16. Diagram of Lemo connector to electrical feedthrough.....	61
17. Lab VIEW motor control interface.....	62
18. View from PIXE CCD camera.....	64
19. SDD detector.....	69
20. Operation and construction of the XR-100 Fast SDD.....	69
21. SDD detector core.....	71
22. FWHM vs. count rate frequency.....	72
23. $Fe - 55$ FWHM resolution vs. peaking time and temperature.....	74
24. Model of detector efficiency.....	77
25. Efficiency vs. energy for Fast SDD.....	78
26. Block Diagram: Detector, Preamp, Digital pulse processor.....	80
27. Energy scale, Gain:5.....	82
28. Energy scale, Gain:10.....	82
29. Energy scale, Gain:15.....	83
30. Energy scale, Gain:20.....	83
31. Energy scale, Gain:25.....	84
32. Energy scale, Gain:30.....	84
33. Energy scale, Gain:35.....	85
34. Energy scale, Gain:40.....	85
35. Energy scale, Gain:45.....	86
36. Fast SDD dimensions.....	92
37. XR-100 Fast SDD.....	92
38. $Fe - 55$ , $Cs - 137$ calibration data.....	101
39. Gain vs. full scale energy range.....	103
40. $Fe - 55$ Gain:5.....	104
41. $Fe - 55$ Gain:10.....	104
42. $Fe - 55$ Gain:15.....	105
43. $Fe - 55$ Gain:20.....	105

44. <i>Fe</i> – 55 Gain:25.....	106
45. <i>Fe</i> – 55 Gain:30.....	106
46. <i>Fe</i> – 55 Gain:35.....	107
47. <i>Fe</i> – 55 Gain:40.....	107
48. Electronic noise vs. peaking time.....	110
49. <i>Fe</i> – 55 spectra @ 1 $\mu A$ .....	111
50. <i>Fe</i> – 55 spectra @ 4 $\mu A$ .....	111
51. <i>Fe</i> – 55 spectra @ 11.2 $\mu A$ .....	112
52. <i>Fe</i> – 55 spectra @ 25.6 $\mu A$ .....	112
53. Count rate vs. dead time.....	113
54. <i>Au</i> spectra @ 2 <i>MeV</i> , 2.5 <i>nA</i> .....	114
55. <i>Au</i> spectra @ 3 <i>MeV</i> , 1 <i>nA</i> .....	115
56. <i>GaP</i> spectra @ 3 <i>MeV</i> , 1 <i>nA</i> .....	116
57. <i>GaP</i> spectra @ 3 <i>MeV</i> , 1 <i>nA</i> (linear scale) .....	116
58. Superconductor material spectra, 2 <i>MeV</i> , 2.1 <i>nA</i> .....	117
59. Superconductor material spectra, 2 <i>MeV</i> , 2.1 <i>nA</i> (linear scale).....	117
60. Superconductor material spectra, 3 <i>MeV</i> , 1 <i>nA</i> .....	118
61. <i>FeO<sub>3</sub></i> on <i>Al</i> Mylar, 2 <i>MeV</i> , 2.6 <i>nA</i> .....	119
62. <i>FeO<sub>3</sub></i> on <i>Al</i> Mylar, 2 <i>MeV</i> , 12 <i>nA</i> .....	119

## **1. Introduction**

### **1.1 XRF and an Introduction to PIXE**

X-ray fluorescence, or XRF, is a common analytical technique used to assess the elemental makeup of materials. High energy electron beams, x-rays, alpha particles, and protons can all be used to induce XRF. XRF is a preferred method for analysis because of its expeditious and non-destructive nature in determining elemental composition which may then be used in the determination of the origin, dating, purity, or authenticity of a given sample. Many disciplines such as archaeology, metallurgy, chemistry, biology, geology, and even art conservation have an interest in using XRF for analysis.

PIXE, or Particle (or proton) induced x-ray emission is an XRF process that occurs when a material is exposed to an MeV ion beam. The procedure begins when a particle accelerator sends charged particles, typically protons, into an evacuated analysis chamber containing the material impending evaluation. Electrons found in the innermost shells of the target atoms are expelled and vacancies are created, but outer shell electrons transition in to replace these vacancies. Consequently, electromagnetic radiation is emitted that possesses frequencies found in the x-ray region of the EM spectrum; this radiation is unique to certain elements found in the material. The x-rays are analyzed through a detection system, such as a Lithium drifted Silicon, or Si(Li), detector, then the pulses from the detector are interpreted. As there are numerous and overlapping data peaks, many are indistinguishable from one another, the presence of certain elements in the sample are specified and quantified by means of computer software used to deconvolute the spectra.

There are several procedures that involve the use of ion beam for the examination of individual chemical elements that make up a given substance. All these techniques rely on the same two fundamentals. High energy charged particles bombard a material, and they subsequently lose energy at precise and recognizable rates while passing through the sample. As ions traverse a material there is a probability for nuclear interaction. The results of these atomic collisions include the emission of different forms of energy that are dependent on the probability of interaction specific to the individual characteristics of the targeted atom. These energy emissions can be released by means of charged particles or as a quantum of distinct electromagnetic radiation, and each emission can be used to identify the chemical composition of a given study sample.

PIXE spectroscopy, is a highly practical method used in the determination of the chemical composition of a substance. PIXE is achievable when charged particles are given energy with a particle accelerator, the ions are focused, collimated, and then forced to irradiate a specimen. As the target material is bombarded, the protons, or other heavy ions, interact with target atoms in a series of inelastic collisions, primarily Coulomb interactions. According to the specific energy loss, or stopping power of the target material, an incoming ion will encounter a steady decrease in velocity as its energy is transferred to the target. With a probability dictated by the interaction cross-section, some of these ionized atoms will emit characteristic x-rays upon their return to ground state. With the help of a suitable x-ray spectrometer, analysis of photons generated by the de-excitation of ionized atoms is performed, and accurate elemental identification can be accomplished. [1]

## 1.2 History

James Chadwick proved in 1912 that electrons and alpha particles produced from a radioactive source could induce x-ray emission. The x-ray intensity generated from alpha particle collisions was so low, however, that the specifics of the emission spectra could not be distinguished; therefore, it could not yet be used for purposes of material analysis. [2]

In 1914, using a demountable x-ray tube and flat crystal spectrometer, Henry Mosely laid the groundwork for PIXE when he bombarded a variety of elements and observed the emission of distinctive x-ray frequencies. [3] He also found that there was a mathematical relationship between the wavelengths of x-rays and the atomic numbers of the metals that emitted the photons.

During 1922, Hadding, a Swedish geologist with the University of Lund, detected 10-12 differing elements through an x-ray spectral analysis of an assortment of minerals [4]. When a positive reconciliation between x-ray emission data and a chemical analysis of these minerals occurred, the scientific community quickly saw that x-ray spectroscopy would allow for effective multielemental analysis.

In 1950, Raimond Castaing, at the University of Paris, made a breakthrough in x-ray emission spectrometry when he demonstrated that a specimen being analyzed with an electron microscope emitted x-rays that could be appropriated for multielemental analysis. [5] Using a 1  $\mu\text{m}$  diameter electron beam, and a focusing crystal spectrometer equipped with a Geiger counter detector, Castaing used mostly metallurgical samples positioned to study spatial composition, this method evolved when a scanning electron

microscope was outfitted with an x-ray spectrometer. The brightness of a CRT was modulated by incoming x-rays as a function of energy, and the intensity of the created image gave a visual indication of the distribution of a given element as the electron probe scanned the sample. [5]

Nuclear physics research greatly expanded during the 1950s, and, therefore, the use of particle accelerators increased as well. X-rays were prevalent as background in many nuclear and atomic physics experiments, so it was logical for physicists to gravitate toward theoretical and experimental research surrounding this phenomenon. With theoretical knowledge that bremsstrahlung radiation is produced in greater amounts through the use of electron beam versus proton beam, and with information concerning cross sections regarding x-ray production as a function of particle energy and atomic number, the prospect of utilizing heavy charged particles for analysis started to become of interest. [5] With respect to MeV protons and 10 keV electrons, the cross section for x-ray production is roughly the same. This means that bremsstrahlung background is the main determinant in the sensitivity of x-ray analysis. It is found experimentally that, background induced by protons is negligible; rather, the main source of background is from the bremsstrahlung given off by the secondary electrons created by the proton beam. This fact caused physicists to be inclined to use protons as the preferred projectile in x-ray emission analysis.

In the early 1960s, [6] at the Lawrence Radiation Laboratory in Livermore California, Khan, Potter, and Worley attempted to utilize proton induced x-ray emission as an elemental analysis technique. They used a proportional counter and a low energy proton beam that ranged 100 to 500 *keV* in efforts to measure the thickness of thin

films. [6] The resolution was inadequate in determining contiguous elements though, and reliable multi-elemental analysis could not be implemented. Khan did find that the peak to background ratio for Aluminum was 10,000/1 with protons; whereas, electrons were known to give a 1000/1 peak to background. In the late 1960s, Poole and Shaw verified this at the Harwell Atomic Energy Research Establishment, after they analyzed the x-rays emitted by pure metals and alloys with a crystal spectrometer induced by a proton-probe with a beam collimated to a diameter of 100  $\mu m$ . [7]

During this same period, Ge(Li) Lithium doped Germanium, and Si(Li) solid state surface barrier detectors were being developed. The Ge(Li) detector became the benchmark for gamma ray detection, while the Lithium Drifted Silicon detector was the standard for energy-dispersive x-ray detection. For 5.9 *keV* x-rays, the Si(Li) detector has an average energy resolution of  $\sim 150$  eV; this made distinguishing *K* x-rays from adjacent elements feasible. The Si(Li) detector design allowed for mounting the detector very close to the source of x-ray emission, thus permitting the detector to span a larger solid angle. The close positioning offered superior detection efficiency compared to that provided by a crystal spectrometer.

During 1970, at the Lund Institute of Technology, Johansson et al. [8] equipped with a Si(Li) detector and a 2 MeV proton beam, demonstrated the groundbreaking analytical technique that allowed for the multi-elemental analysis of trace elements. This system of analysis became known as PIXE, or proton induced x-ray emission.

PIXE developed rapidly in many nuclear physics laboratories after Johansson showed its usefulness. During the 1970s there was great concern about environmental

problems, and the sensitivity of PIXE prompted many laboratories to study air pollution and the measurement of toxic elements in humans and their surroundings.

High energy nuclear physics was becoming of more interest at this time, for which small accelerators were being rendered obsolete. These machines were perfect for PIXE analysis though, so rather than disposing of them they were used in PIXE research applications. Electronics, detectors, and computers that could be used in conjunction with PIXE were already available in these nuclear physics labs – this made the transition to this particular analysis technique an obvious choice.

Today many organizations, such as the CSIRO lab in Australia and the Louvre Museum in France, have invested large sums of money in setting up dedicated PIXE laboratories committed to specialized applications. This is a testament to PIXE's ability to compete with differing analytical methods, and it will likely be a favored analysis technique far into the future.

### **1.3 PIXE**

Particle induced x-ray emission occurs as fast ions enter a specimen. Target atoms undergo inelastic collisions with charged projectiles, then, relative to the stopping power and distinctive attenuation properties of the sample, characteristic x-rays are emitted.

#### **1.3.1 Quantum Numbers**

To realize the actions of an electron, the Schrödinger equation can be solved to determine the wave functions for differing electron states. The various states will have associated quantum numbers which correspond to the physical parameters of the

system i.e. momentum and energy. These numbers consist of the principle quantum number  $n$  which is representative of the primary electron shell,  $l$  which characterizes the shape of the orbital and number of subshells,  $m_l$  is the magnetic quantum number, and it specifies the number of energy levels within a subshell thus showing the electron's position in space, and finally  $s$  the quantum number that tells us an electron's half spin orientation – up or down. For a single electron ion, the allowed values for quantum numbers are as follows:

$$n = 1, 2, 3, 4 \dots \quad (1)$$

$$l = 0, 1, 2, \dots, (n - 1) \quad (2)$$

$$m_l = l, (-l + 1), (-l + 2), \dots, -2, -1, 0, 1, 2, \dots, (l - 1), (l - 2), +l \quad (3)$$

$$s = +1/2, -1/2 \quad (4)$$

The first inner shell of an atom ( $n = 1$ ) is referred to as the K shell, and a maximum of two electrons can be found there. A maximum of eight electrons can be found in the L shell ( $n = 2$ ), and the M shell,  $n = 3$ , can house a maximum of 18 electrons. The maximum number of electrons that can be found in a given atomic shell is given by:

$$\text{max}\#_{e^-} = 2n^2 \quad (5)$$

$l$ ,  $m_l$ , and  $s$  states take effect in atoms with electron shells higher than  $n = 1$  as they have more than two permissible electron conditions.

To accurately describe the angular distribution and shape of an orbital, there are several values of the orbital angular momentum quantum number  $l$ , and they are all

dependent on the principle quantum number  $n$ . When  $l = 0, 1, 2, 3, 4, 5, 6$  the states are conventionally referred to as  $s, p, d, f, g, h,$  and  $i$  subshells respectively, each subshell has a distinguishing shape representative of the electron probability distribution. The number of orbitals and their position inside a subshell is given by the magnetic quantum number  $m_l$ . This value is dependent on the angular momentum quantum number and can be a negative integer, a positive integer, or zero. Sub-states indicating the fine electron structure within an atom are designated by electron spin orientation. These are important to know because the electrons in an atom are subject to the Pauli exclusion principle. This principle forbids certain electron transitions within the atom; the same quantum numbers cannot exist for any two electrons within an atom.

### **1.3.2 Transitions**

As depicted in figures (1 – 6), a proton with enough energy (typically MeV) and an inner shell electron found within a sample atom experience a Coulomb interaction. As a result, the inner shell electron is attracted to, and thus, may be pulled out of the atom by, the impinging proton. A vacancy is produced within the inner shell leaving the atom to be in an excited and unstable state. Electrons from outer shells transition to the inner shells causing the atom to return to its ground state. As the atom becomes stable through the transition process, excess energy – the difference between the binding energy of the inner and outer shells – may be released as a photon. The fluorescence yield, or the probability of emission of an x-ray quantum, for heavy elements is close to 100%, but just a few percent for light elements. In general, the fluorescence yield is given by the expression:

$$\omega = \frac{\Gamma_{x-ray}}{\Gamma_{Auger} + \Gamma_{x-ray}} \quad (6)$$

Where  $\omega$  represents the fluorescence yield and  $\Gamma$  is the probability of either an Auger or x-ray emission. There is a certain nomenclature to these transitions. Energy levels of the electrons within an atom determine the x-ray spectra. To indicate the shells they came from, characteristic x-rays are given the designation of  $K$ ,  $L$ ,  $M$ ,  $N$ , and so on. The transitions that end in the K-shell are designated  $K$  x-rays, those going to the L-shell are called  $L$  x-rays, etc. An additional classification is the subscript alpha, beta, or gamma ( $\alpha$ ,  $\beta$ , or  $\gamma$ ). These indicate electron transitions originating from higher energy shells. For example, if an electron fills a K-shell vacancy, but it came from the L-shell, the transition is classified as  $K_\alpha$ . An electron jump from the M-shell to the K-shell is called a  $K_\beta$  transition, and a transition from the N-shell to the L-shell is denoted by  $L_\gamma$ . Again, the Pauli Exclusion Principle cannot be violated, and there is a fine structure due to spin-orbit coupling. These doublets have approximately the same energy since the shells have multiple orbits of higher and lower binding electrons, and they may appear unresolved in a single peak in the spectrum. These fine structure transitions are assigned further designations of  $\alpha_1$ ,  $\alpha_2$ , or  $\beta_1$ ,  $\beta_2$ , etc. In a PIXE spectrum light and medium-heavy elements typically give only two specific peaks  $K_\alpha$  and  $K_\beta$ , while in the  $L$  x-ray spectrum of heavy elements there are four predominant resolved peaks and four weaker peaks. [5, 9] Therefore, depending on the element undergoing a transition to ground state, an assortment of x-ray energies may emanate from a target while under proton bombardment. Therefore, a multitude of elements composing a sample can be identified as they all have differing, or characteristic, x-ray energies.

Once ionized, excited atoms have the probability of depositing energy directly into an outer shell electron instead of emitting a photon. The excited electron can deexcite by returning to a state of lower binding energy by emitting an electron from a more loosely bound state; in turn, excess energy is carried off with the ejected electron. This nonradiative transition is known as the "Auger effect", and the ejected electrons are known as "Auger" electrons. [10,11] If an atom was originally excited when the proton carried away an inner shell electron, and the atom rids itself of excess energy through an Auger emission, the atom has lost a total of two electrons, and is now found in a doubly charged state. The doubly charged atom can return to its steady state by emitting a third Auger electron from the M shell, or by single- or double-electron transitions that emit weaker "satellite" x-ray lines. Auger emission tends to be more probable for lower atomic number elements, since the effect increases as the difference in corresponding energy states become smaller.

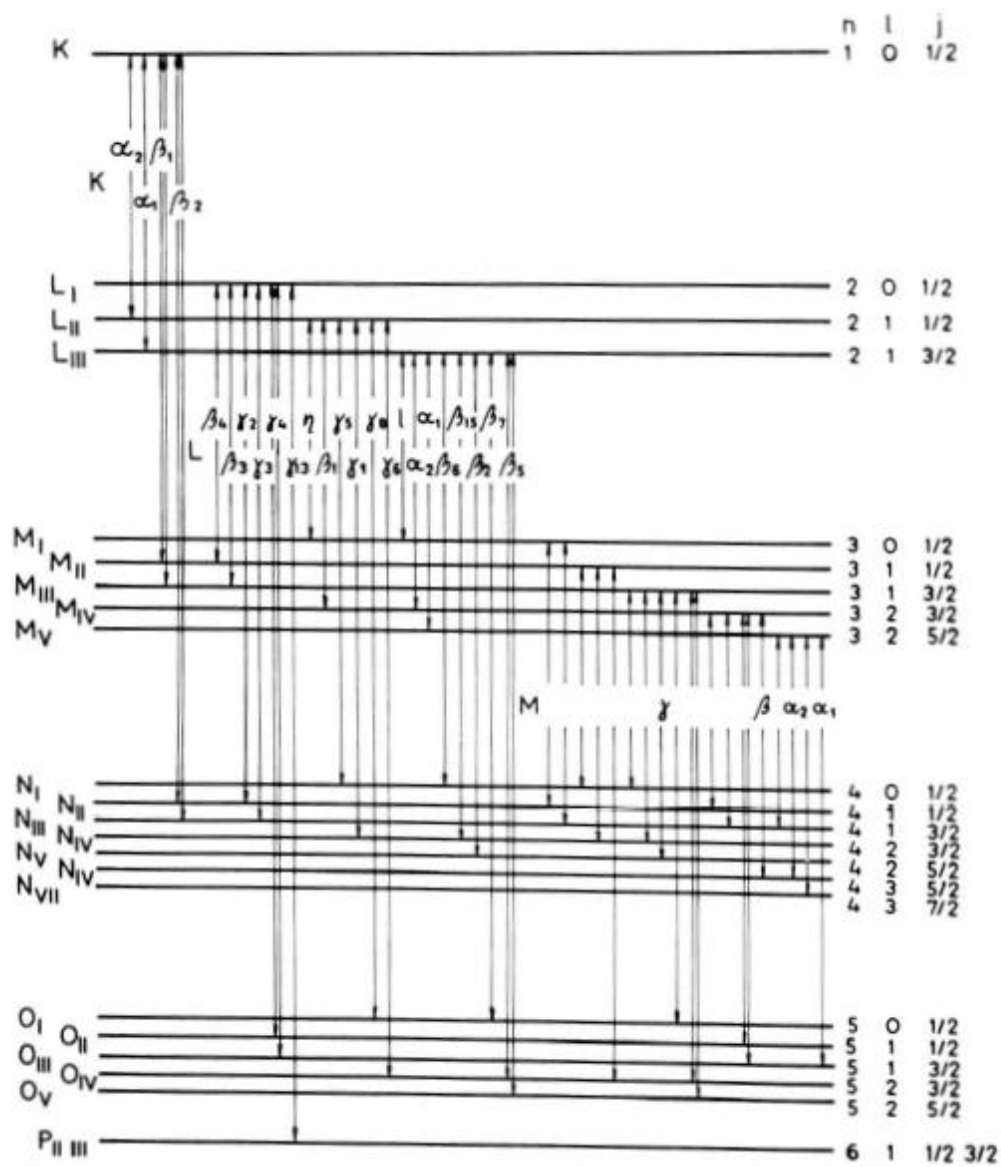
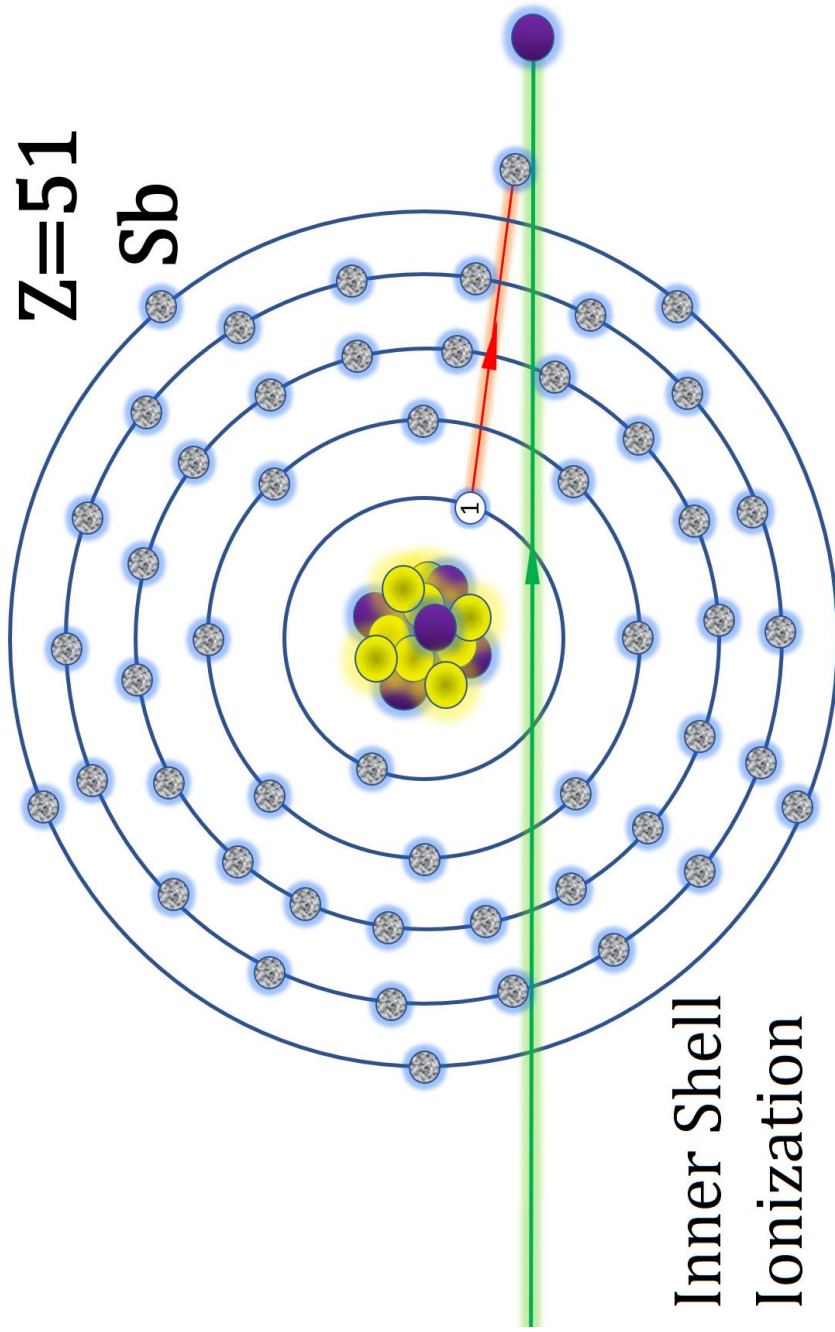


Figure (1). Nomenclature for x-ray lines and energy levels. [12]



## Inner Shell Ionization

- 1) A K-shell electron is dislodged from an Antimony atom through Coulomb interaction with a proton, and a vacancy is created.

Figure (2) XRF.

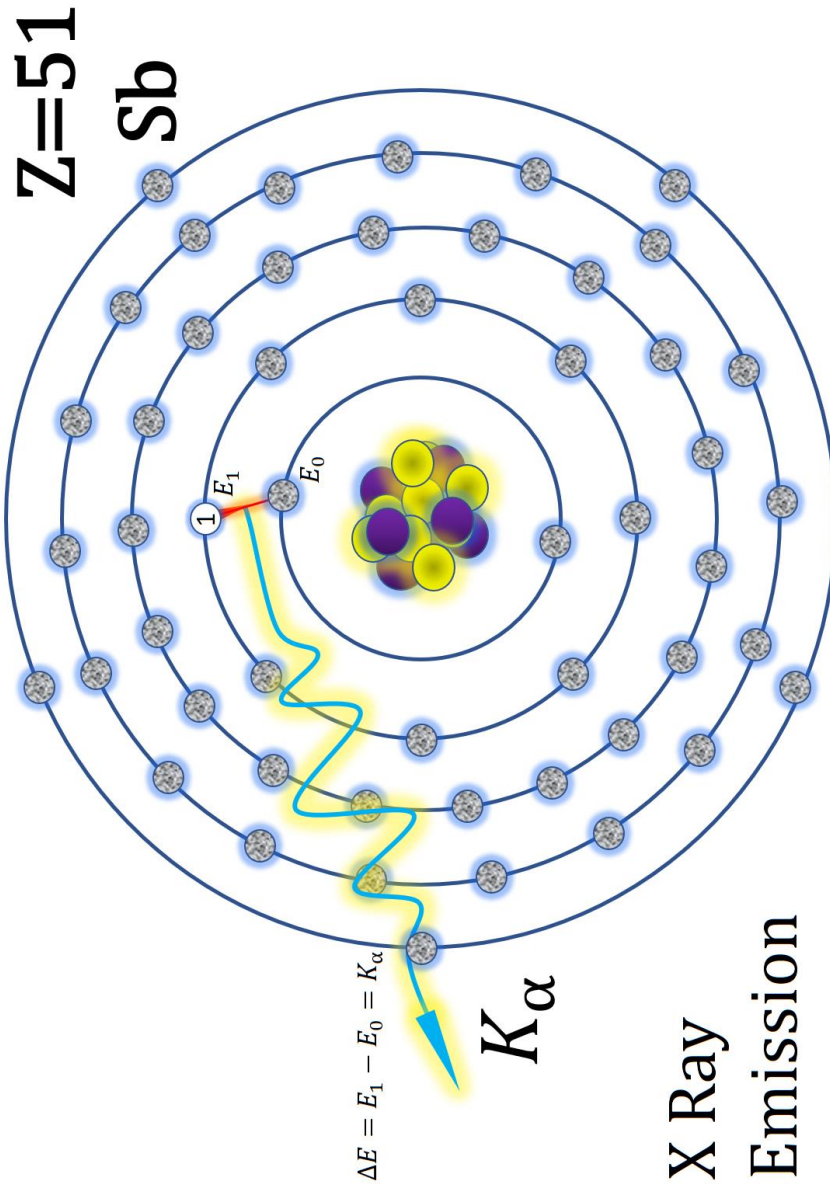


Figure (3) XRF.

- 2) An L-shell electron transitions into the vacant K-shell, and it emits a characteristic  $K_\alpha$  x-ray unique to this element; a vacancy is created in the L-shell.

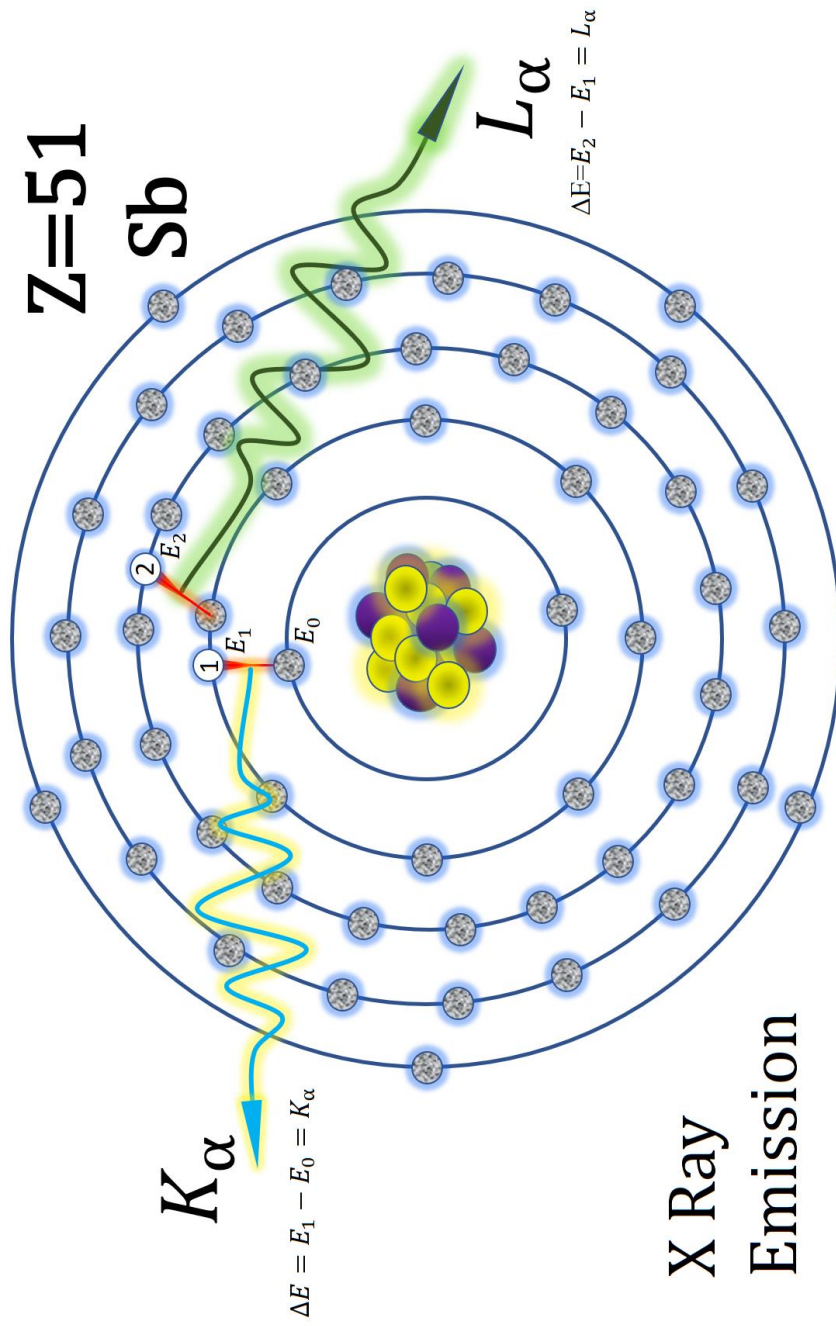


Figure (4) XRF.

3) The vacancy created in the L-shell and is filled by an M-shell electron inducing an  $L\alpha$  x-ray

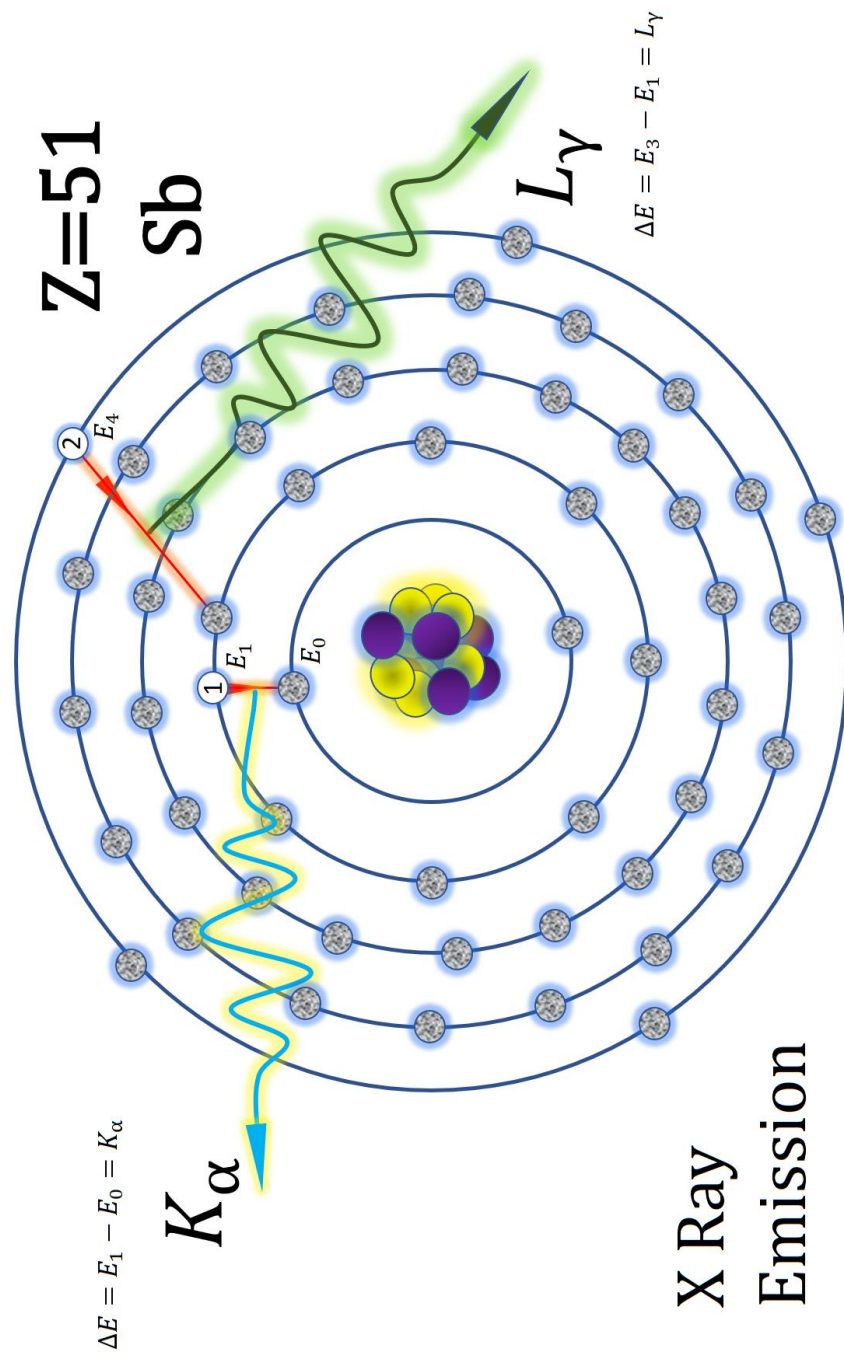


Figure (5) XRF.

4) It is also probable that an N-shell electron transitions into the vacant L-shell of Antimony; a characteristic  $L_\gamma$  x-ray is produced.

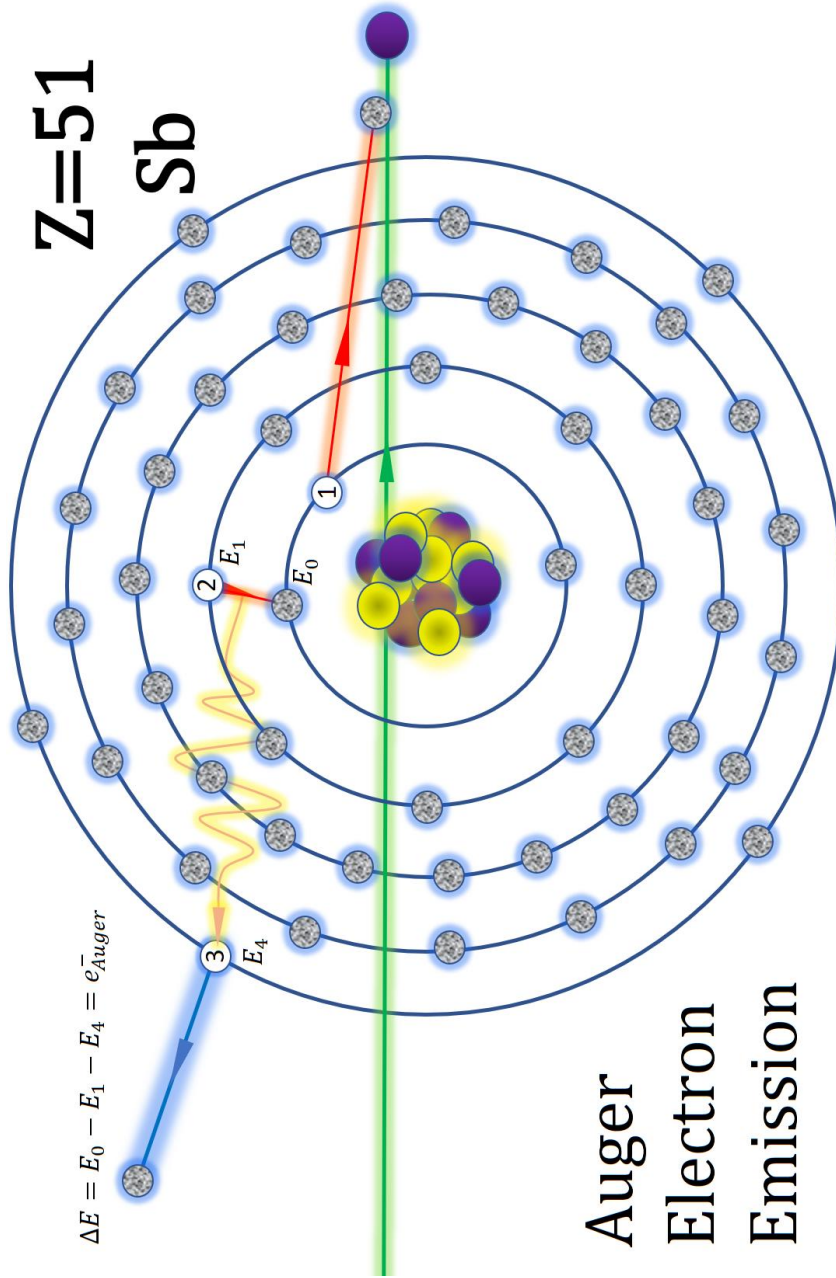


Figure (6) Auger Emission.

5) Energy from the atom's inner shell is transferred to an outer shell electron causing its expulsion from the atom in the "Auger" electron emission process.

### 1.3.3 Detection Limits

Most detectors have a very thin Beryllium window, this dictates the lower detection limit for any XRF analysis system. Fluorine ( $Z=9$ ) and below are not usually detectable, since x-rays emitted by these elements are highly attenuated by the beryllium detector window. The ionization cross section of an element is the determinant in the upper detection limit. The elements within the interval of  $20 < Z < 50$  typically allow for successful detection of  $K$  x-rays with a Si(Li) detector (ECU's SDD detector has successfully shown  $Z=11$  spectral data). Typically,  $K$  x-rays of lower  $Z$  elements are buried in the background spectra, but with the advent of superior detector technology, low  $Z$  element x-ray emission energies can be detected.  $L$  x-rays are detected as four distinct peaks in elements above  $Z=50$ . Heavy elements are detected by their  $L$  x-rays, and the medium-heavy to light elements can be identified by their characteristic  $K$  x-rays. Beam current, run time, and detector efficiency all influence effective x-ray detection. [5]

### 1.3.4 Fluorescence yields

As an electron is torn from the inner shell of an atom by fast proton interaction, it would be intuitive to assume that the XRF would equal the amount of inner shell vacancies being filled by stabilizing transitions. The probability of a vacant atomic shell or subshell receiving an electron transitioning from a higher energy shell and producing radiative emission is termed fluorescence yield, but it is not found to be unity. The Auger emission process competes with XRF when it facilitates energy being carried off as electrons are ejected from their outer shells. This lowers the probability of a photon

emission by the same probability of an Auger emission. The expression for  $\omega_K$ , the fluorescence yield of the K shell, is

$$\omega_K = \frac{I_K}{n_K} \quad (7)$$

Where the total number of  $K$  x-rays emitted from a target are given by  $I_K$ , while  $n_K$  denotes the number of primary K shell vacancies. The Auger emission and fluorescence yields for vacancies produced in the K shell add to one.

The fluorescence yield brought about by higher shell transitions is more intricate though, because, unlike the K shell, the L and M shells possess more than one subshell, and, depending on how the shells are ionized, the average fluorescence yield will change. Additionally, nonradiative, Coster-Kronig transitions take place within the subshells of atomic shells of identical principal quantum numbers. [13,14]

By neglecting Coster-Kronig transitions, the fluorescence yield would be of the  $i^{th}$  subshell of a principal quantum shell of  $X = L, M, \dots$ , etc. and it is shown by:

$$\omega_i^X = \frac{I_i^X}{n_i^X} \quad (8)$$

However, primary vacancy distributions are altered by Coster-Kronig transitions, since the ionization from one subshell of a higher energy transitions to a subshell of lower energy. A more accurate expression for transition probabilities is as follows:

$$\omega_i^X + \alpha_i^X + \sum_{j=1}^k f_{ij}^X = 1 \quad (9)$$

Where Auger emission probability of the  $i^{th}$  subshell in shell  $X$  is expressed by  $\alpha_i^X$ , when a nonradiative electron transition occurs.  $k$  represents the number of

subshells and  $f_{ij}^X$  stands for Coster-Kronig transition probability for a shift from a lower to higher subshell, specifically  $X_i$  to  $X_j$ . The last variables to note are the fluorescence yields found in the L shell:  $\omega_{L1}$ ,  $\omega_{L2}$ ,  $\omega_{L3}$ . K, L, and M shell fluorescence yields and Coster-Kronig transition probabilities are given in tables 1 and 2.

Fluorescence yields and Coster-Kronig transition probabilities.

Atomic number	Element	$\omega_K$	Atomic number	Element	$\omega_K$
6	C	0.0009	45	Rh	0.81
7	N	0.0015	46	Pd	0.82
8	O	0.0022	47	Ag	0.83
10	Ne	0.0100	48	Cd	0.84
11	Na	0.020	49	In	0.85
12	Mg	0.030	50	Sn	0.86
13	Al	0.040	51	Sb	0.87
14	Si	0.055	52	Te	0.875
15	P	0.070	53	I	0.88
16	S	0.090	54	Xe	0.89
17	Cl	0.105	55	Cs	0.895
18	Ar	0.125	56	Ba	0.90
19	K	0.140	57	La	0.905
20	Sc	0.165	58	Ce	0.91
21	Ca	0.190	59	Pr	0.915
22	Ti	0.220	60	Nd	0.92
23	V	0.240	61	Pm	0.925
24	Cr	0.26	62	Sm	0.93
25	Mn	0.285	63	Eu	0.93
26	Fe	0.32	64	Gd	0.935
27	Co	0.345	65	Tb	0.94
28	Ni	0.375	66	Dy	0.94
29	Cu	0.41	67	Ho	0.945
30	Zn	0.435	68	Er	0.945
31	Ga	0.47	69	Tm	0.95
32	Ge	0.50	70	Yb	0.95
33	As	0.53	71	In	0.95
34	Se	0.565	72	Hf	0.955
35	Br	0.60	73	Ta	0.955
36	Kr	0.635	74	W	0.96
37	Rb	0.665	75	Re	0.96
38	Sr	0.685	76	Os	0.96
39	Y	0.71	77	Ir	0.96
40	Zr	0.72	78	Pd	0.965
41	Nb	0.755	79	Au	0.965
42	Mo	0.77	80	Hg	0.965
43	Tc	0.785	82	Pb	0.97
44	Ru	0.80	92	U	0.97

Table (1). K shell fluorescence yields  $\omega_K$  for Z=6 through Z=92. [15]

Fluorescence yields and Coster-Kronig transition probabilities.

Atomic number	Element	$\omega_1$	$\omega_2$	$\omega_3$
54	Xe			$0.10 \pm 0.01$
56	Ba	0.06		$0.05 \pm 0.01$
65	Tb	0.18	$0.165 \pm 0.018$	$0.188 \pm 0.016$
67	Ho			$0.22 \pm 0.03$
68	Er		$0.170 \pm 0.055$	$0.169 \pm 0.030$
70	Yb		$0.185 \pm 0.060$	$0.21 \pm 0.03$
71	Lu		$0.188 \pm 0.011$	$0.172 \pm 0.032$
72	Hf			$0.20 \pm 0.02$
73	Ta		$0.25 \pm 0.02$	$0.183 \pm 0.011$
			$0.257 \pm 0.013$	$0.22 \pm 0.03$
				$0.251 \pm 0.035$
				$0.22 \pm 0.03$
				$0.228 \pm 0.025$
				$0.27 \pm 0.01$
				$0.25 \pm 0.03$
				0.191
				$0.228 \pm 0.013$
				$0.254 \pm 0.025$
74	W			0.207
				$0.272 \pm 0.037$
75	Re			$0.284 \pm 0.043$
76	Os			$0.290 \pm 0.030$
77	Ir			0.244
				$0.262 \pm 0.036$
78	Pt		$0.331 \pm 0.021$	0.262
				$0.31 \pm 0.04$
				$0.317 \pm 0.029$
				$0.291 \pm 0.018$
79	Au			0.276
				$0.31 \pm 0.04$
				$0.317 \pm 0.025$
80	Hg		$0.39 \pm 0.03$	$0.40 \pm 0.02$
			$0.319 \pm 0.010$	$0.32 \pm 0.05$
				$0.367 \pm 0.050$
				$0.300 \pm 0.010$
81	Tl	$0.07 \pm 0.02$	$0.319 \pm 0.010$	$0.37 \pm 0.07$
			$0.373 \pm 0.025$	$0.386 \pm 0.053$
				$0.306 \pm 0.010$
				$0.330 \pm 0.021$
82	Pb	$0.07 \pm 0.02$	$0.363 \pm 0.015$	0.337
		$0.09 \pm 0.02$		$0.315 \pm 0.013$
				0.32
				$0.35 \pm 0.05$
				$0.354 \pm 0.028$
83	Bi	$0.12 \pm 0.01$	$0.32 \pm 0.04$	0.367
		$0.095 \pm 0.005$	$0.38 \pm 0.02$	0.36
				$0.37 \pm 0.05$
				$0.362 \pm 0.029$
				$0.40 \pm 0.05$
				$0.340 \pm 0.018$

Table (2). Experimental L shell fluorescence yields  $\omega_i$ . [15]

### 1.3.5 Ionization Cross Sections

To express the probability that a particle induced K or L shell ionization occurs, we refer to ionization cross sections. A larger cross section is representative of a larger probability for ionization to occur. Cross section can be conceptualized as a two-dimensional area that represents the probability of fast ion interaction with a target atom. Nuclear cross sections are typically measured in units of “barn”. One barn equals  $10^{-28}m^2$ . The atomic cross section, traditionally given in units of  $cm^2$ , decreases as atomic number increases, and a higher proton energy will cause a decrease in the cross section of a given target.

The geometric cross section is not of much concern as it can be either smaller or larger than the nuclear (interaction) cross section of the target atom. Originally, the Plane Wave Born Approximation (PWBA) model was used to estimate inner shell ionization cross sections. However, Brandt and Lapicki laid the groundwork for the Energy-Loss Coulomb-Repulsion Perturbed-Stationary-State Relativistic (ECPSSR) theory, which was a great improvement to the PWBA model, and is closer in predicting the ionization cross section of an atom. The ECPSSR model addresses critical interaction factors such as the increase in binding energy caused by the fast ion, and the Coulomb deflection forces the ion experiences as it approaches the target nucleus. To exclude very low Z materials, the ECPSSR model K-shell calculations reconcile within a few percent of the most reliable cross section ionization data. [16, 17]

### 1.3.6 Spectral Background

The Detection limit in x-ray spectroscopy is primarily governed by the continuous background found within PIXE spectra. Inbound fast ions interacting with material surrounding the sample, or other materials found within the chamber, can incite background rays. A halo effect from a poorly collimated beam can produce x-rays in the target holder or chamber walls. The graphite collimator and Faraday cup can also be sources of background x-rays if the detector is within line-of-sight to these components. To detect background x-ray peaks, while the Faraday cup is in normal operating position, the proton beam should pass through an empty target holder during the performance of a data acquisition run. Close placement between the sample and collimator, and proper beam alignment ensures that no material, excluding sample targets, will be irradiated by fast ions; ECU's PIXE apparatus has an imperceptible amount of x-ray induced background during data acquisition.

It is important to note that the key promoters of background with PIXE are proton induced primary bremsstrahlung, electron bremsstrahlung, and  $\gamma$ -ray emission. Primary bremsstrahlung produced by a charged particle is proportional to the square of its deceleration. [18] The electron and proton experience the same Coulombic forces, but their masses have a ratio of 1836:1, so primary projectile bremsstrahlung associated with incoming protons is negligible compared to the radiation produced by secondary electrons. [18] Regarding PIXE, the main generator of x-ray background is then the bremsstrahlung associated with the electrons that are ejected from the atom as a result of inelastic collisions. As the Coulomb field of a target nucleus scatters, or accelerates, secondary electron induced atomic bremsstrahlung emission occurs.

When a resting electron of mass  $m_e$  encounters a head-on-collision with a charged projectile of mass  $M_p$  having an energy of  $E_0$ , the electron can receive no more energy than  $T_m$ ; the maximum amount of kinetic energy that can be transmitted to the electron is approximately:

$$T_m = 4E_0 \left( \frac{m_e}{M_p} \right) \quad (10)$$

Where secondary electron energies have values of 2.2 keV for a 1MeV proton beam, 4.4 keV for 2 MeV protons, and 6.535 keV for 3 MeV protons. When an energetic charged particle is decelerated, the excess kinetic energy is given off as electromagnetic energy; this radiative process is referred to as Bremsstrahlung radiation. [18]

Secondary electrons are ejected inelastically in the same forward direction as the proton beam. Bremsstrahlung peaks at  $90^\circ$  with respect to the direction of the ejected electrons and is at a minimum in the direction of the incoming beam. Ideally the detector would be perpendicular to the sample (as far away from  $90^\circ$  as possible), but the chamber's geometry prevents this. ECU's SDD detector is located  $135^\circ$  degrees from the forward direction of the ion beam, or, in other words,  $45^\circ$  to the normal of the sample. Even though, at photon energies beyond 6 keV, atomic bremsstrahlung is the primary contributor to the continuous PIXE spectrum, the bremsstrahlung is practically unnoticeable in the x-ray fluorescence spectra and was of little consequence during system calibration.

$\gamma$ -rays are much less visible in the PIXE spectrum and are more difficult to detect than background x-rays.  $\gamma$ -rays typically have energies in the hundreds of keV, a flat

background in the 1-30  $keV$  range is usually recorded due to the Compton scattering of  $\gamma$ -rays in the detector. Table (3) shows elements that will yield the highest amounts of  $\gamma$ -rays. If these elements (e.g. lithium, boron, or sodium) are sited within a sample, a substantial quantity of  $\gamma$ -rays will be created in the target itself. With organic compounds, at proton energies below 3 MeV, Johansson demonstrated that Carbon-13 was the primary source of  $\gamma$  radiation. [19] Fluorine, however, because of the element's large cross section for  $(p, p\gamma)$  and  $(p, \alpha\gamma)$  reactions, has the highest  $\gamma$ -ray yield; therefore, it is advisable to avoid Teflon sample holders when performing PIXE. Typically, when carrying out proton induced x-ray emission, the most common source of  $\gamma$ -ray production is brought about by the aluminum used to achieve collimation within the beam line. [18]

Element	E $\gamma$ (keV)	$\gamma$ ray yield (x 10 <sup>6</sup> counts/ $\mu$ C Sr)			Reaction
		1.7 MeV	2.4 MeV	3.1 MeV	
Li	429	-	-	9.2	<sup>7</sup> Li(p,n $\gamma$ ) <sup>7</sup> Be
	478	8.6	26.0	56.0	<sup>7</sup> Li(p,p $\gamma$ ) <sup>7</sup> Li
Be	3562	-	0.02	2.5	<sup>9</sup> Be(p, $\alpha$ $\gamma$ ) <sup>6</sup> Be
B	429	0.9	3.5	7.2	<sup>10</sup> B(p, $\alpha$ $\gamma$ ) <sup>7</sup> Be
	718	-	0.12	1.3	<sup>10</sup> B(p,p $\gamma$ ) <sup>10</sup> B
	2125	-	-	4.8	<sup>11</sup> B(p,p $\gamma$ ) <sup>11</sup> B
F	110	0.1	7.2	11.0	<sup>19</sup> F(p,p $\gamma$ ) <sup>19</sup> F
	197	0.2	20.0	37.0	<sup>19</sup> F(p,p $\gamma$ ) <sup>19</sup> F
	1236	-	3.0	5.4	<sup>19</sup> F(p,p $\gamma$ ) <sup>19</sup> F
	1349	-	1.3	2.1	<sup>19</sup> F(p,p $\gamma$ ) <sup>19</sup> F
	1357	-	1.4	4.2	<sup>19</sup> F(p,p $\gamma$ ) <sup>19</sup> F
	1459	-	0.9	3.9	<sup>19</sup> F(p,p $\gamma$ ) <sup>19</sup> F
	6129	2.6	67.0	95.0	<sup>19</sup> F(p, $\alpha$ $\gamma$ ) <sup>16</sup> O
Na	440	0.8	9.6	16.0	<sup>23</sup> Na(p,p $\gamma$ ) <sup>23</sup> Na
	1634	0.2	9.9	19.0	<sup>23</sup> Na(p, $\alpha$ $\gamma$ ) <sup>20</sup> Ne
Mg	1369	0.1	0.9	5.1	<sup>24</sup> Mg(p,p $\gamma$ ) <sup>24</sup> Mg
Al	844	-	0.1	2.3	<sup>27</sup> Al(p,p $\gamma$ ) <sup>27</sup> Al
	1014	-	0.3	4.6	<sup>27</sup> Al(p,p $\gamma$ ) <sup>27</sup> Al
Si	1779	-	-	1.2	<sup>28</sup> Si(p,p $\gamma$ ) <sup>28</sup> Si
P	1266	-	1.6	5.2	<sup>31</sup> P(p,p $\gamma$ ) <sup>31</sup> P
Cl	1219	-	0.2	1.5	<sup>35</sup> Cl(p,p $\gamma$ ) <sup>35</sup> Cl

Table (3). Gamma Ray yields for select light element targets with 10<sup>6</sup> counts/ $\mu$ C-Sr or higher. [20]

Nuclear interactions brought about by impinging protons or x-rays within the Pelletron accelerator can be a contributor to  $\gamma$ -ray emissions. As electrons are stripped from the  $H^-$  ion they accelerate back to the positively charged accelerator terminal, in turn, bremsstrahlung transpires. During the calibration of ECU's PIXE system, no significant sources of background x or  $\gamma$ -rays were observed.

A smaller contributor to background is brought about by naturally occurring  $\gamma$ -rays. If this background were significant, lead shielding could be wrapped around the detector to attenuate the naturally occurring  $\gamma$ -rays before they reach the silicon diode.

Sample charging caused by high energy protons can also result in background. If a sample has no route to dispel accumulated charge, the target will spark as it gives up its charge to an object with the nearest conduction path. The small electrical discharges will cause x radiation, for this reason, the sample wheel has a copper grounding brush that constantly contacts the electrically isolated target carousel; it provides a conduction path for accumulated charges. If the specimens are electrically isolated from the target carousel, it is suggested to apply a thin coating of conducting carbon spray onto both the sample and the carousel to create electrical continuity between them.

### **1.3.7 Mechanical, Electrical, and Thermal Noise**

Mechanical noise can be brought about by vibrations and accelerator noises in and about the specimen chamber, this can diminish the efficacy of the Silicon Diode Drift detector; vibrations from the accelerator may contribute to background noise in the spectrum. While the sound of the accelerator is intense during operation, it occurs at a high frequency and there has been no evidence of a decrease in detector resolution

because of it. A more notable source of vibration that may affect the detector stems from the turbomolecular pump located on the bottom of the chamber, but again, there was no real indicator that these vibrations influenced detector performance.

Ripple, and electrical noise, can come from several sources. The connectors attached to the detector hardware and digital pulse processor are shielded to minimize noise resulting from electromagnetic fields. However, with ECU's PIXE configuration the most drastic sources of EMF are located far from the detector. There are some unshielded wires within the chamber (motor control terminal blocks and wires), but these wires should never be in use during active data collection; these conductors should have no effect on SDD detector performance.

The outer shielding of the cables provide continuity between the component housings and ground. These instrument chassis (the target chamber, the SDD detector, the PX5 digital pulse processor, and data acquisition PC) are all grounded closely through the same point (the accelerator itself), and there has been no ground loop noise detected in the circuitry. If spectral data shows degraded energy resolution, an oscilloscope can be used to test for noise pickup when it is connected to the auxiliary output of the PX5.

Thermal noise is reduced with the cooling circuitry of the detector and becomes insignificant below 233K. ECU's SDD has been shown to operate between 196 and 210 K – there has been no witness to thermal noise during calibration runs.

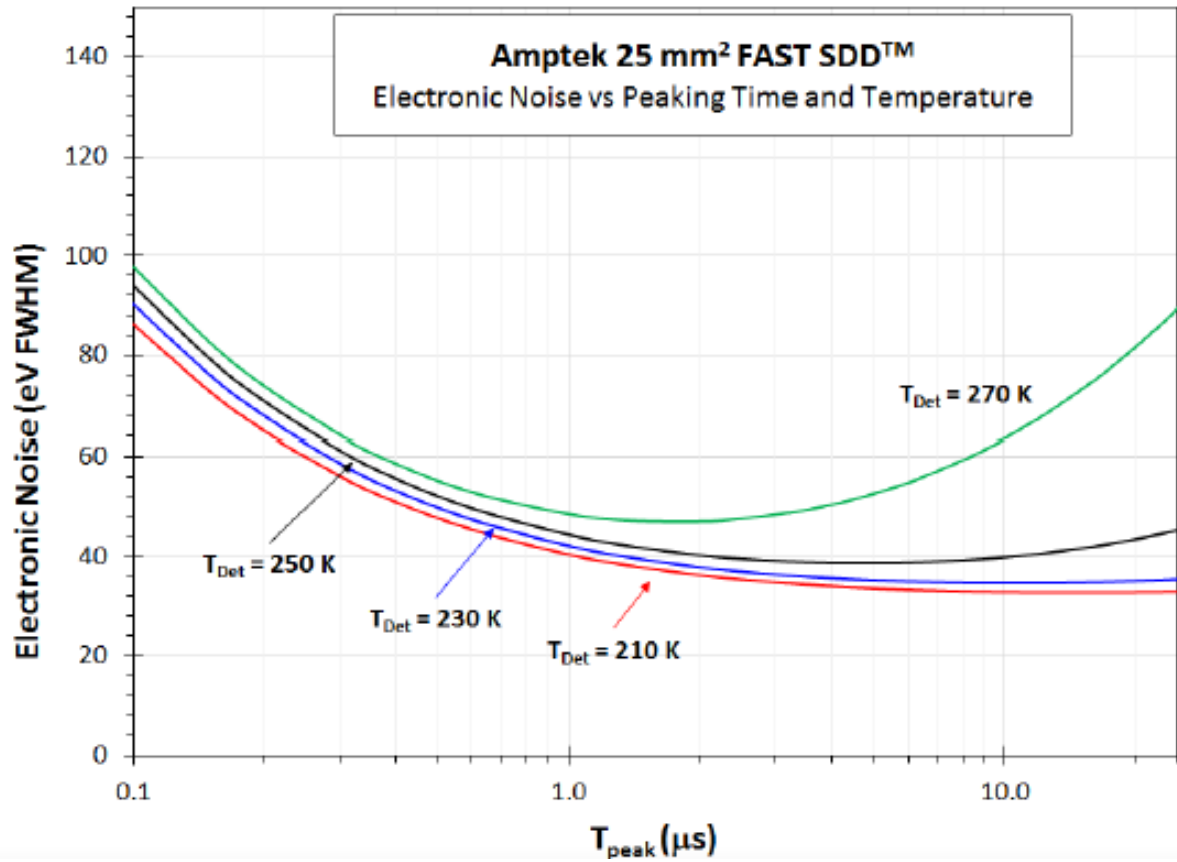


Figure (7). The full width half max noise verses peaking time for the Fast SDD. [21]

### 1.3.8 Sample Composition and Attenuation

The probability of x-ray production is not the only aspect in effective PIXE analysis. Target composition also influences x-ray attenuation and proton energy loss. The x-ray, or fluorescence, yield ( $Y_i$ ) for an  $i^{th}$  element contained within a sample towards the direction of the detector is shown as:

$$Y_i = \frac{Q}{e} \int_0^d c(x) \sigma_i(E(x)) e^{-\mu \frac{x}{\cos \theta}} dx \quad (11)$$

Where  $Q$  denotes the total exposure of the sample by the incoming particle beam, and  $d$  stands for the thickness of the sample. While passing through the target material, the projectiles lose energy by:

$$E(x) = \int_0^x S(E) dx \quad (12)$$

Where the particle stopping power,  $S(E)$  is

$$S(E) = \frac{dE}{dx} \quad (13)$$

If the concentration  $c(x)$  of the  $i^{th}$  element does not change throughout the sample, the connection between elemental concentration and x-ray intensity is provided by

$$I_i = QC_i K_i \quad (14)$$

Where the  $I_i$  represents the statistical uncertainty in the determination of peak area, and the calibration constant ( $K_i$ ) is independent of the sample if both the target matrix and experimental geometry ( $\theta$ ,  $\varphi$ ) remain constant.

$$K_i = \varepsilon \int_0^d \sigma_i(E(x)) e^{-\mu \frac{x}{\cos \theta}} dx \quad (15)$$

To quantify, a fundamental parameter approach can be applied by using the x-ray fluorescence cross sections ( $\sigma_i$ ), x-ray attenuation ( $\mu$ ), and particle stopping power in calculating the calibration constant. [20]

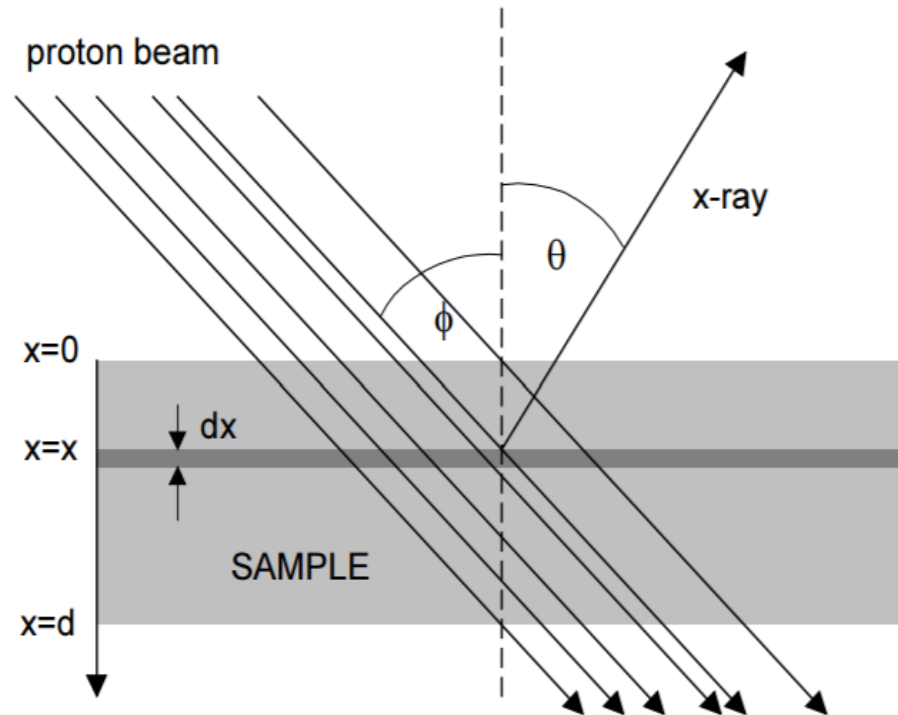


Figure (8). Typical schematic for PIXE analysis. [20]

PIXE targets fall into two main categories: thin and thick specimens. Thin targets (usually films) are classified as such, because only a small portion of beam energy is lost while passing through the sample making analysis relatively simple. [18] In contrast, thick specimens (specimens that completely stop the beam) are typically easier to prepare for analysis, but other factors, such as a smooth and flat impact surface with a known thickness and matrix structure, along with a controllable and reproducible experimental environments, are ideal. As mentioned, the impact surfaces of thick targets should be as smooth and flat as possible while offering precise and duplicable angles to the particle beam; the sample should be perpendicular with respect to the beam, and at a  $45^\circ$  with respect to the direction of x-ray emission. An impeccably flat and polished surface will yield higher x-ray intensities in contrast to samples with substantial irregular rough patches in relation to the x-ray attenuation length of a target. The effects of curvature and coarseness of a sample have been meticulously calculated with considerable accuracy. [22,23] An unblemished surface allows the assumption of a uniform dispersion of elements within the sample during analysis. If the surface is irregular, uncertainties in the elemental distribution should be accounted for. But equations (11) and (12) make it evident that dependable PIXE relies on several more factors that determine a well-defined sample. Factors such as statistical uncertainty in the determination of peak area  $I_i$ , detector efficiency  $\epsilon$ , particle energy  $E_0$ , and the total exposure of the sample to the incoming proton beam are additional criteria for successful PIXE analysis. [20]

Specimens can be heterogeneous in their original state and may need to be reduced and homogenized either physically or chemically before proton irradiation. Geological samples typically qualify for this treatment. It is noteworthy that homogenizing a sample will make the analysis of spatial variations within the target impossible. These specimens can be ground and mixed with a binding agent, carbon works well as a binding agent due to its conductive properties.

A colloidal suspension of powdered target material can be pipetted onto a substrate such as chemically treated Mylar® that will form a film for analysis after the liquid dries on the filter material. Solids can be dissolved through acid reduction and deposited on the filter to dry. This method offers impartial analysis by guaranteeing a standardized sample of a large portion of primary specimen material. This method also allows for the addition of known elements within the solution used to set internal standards within the sample. The drawback to this method is that the sample thickness is not always uniform. For example, when a bead of solution evaporates, the suspended particles become thicker in the last place evaporation occurred. However, with substances like dried blood, it tends to dry thicker on the outer ring of the droplet. An acceptable remedy is to pretreat the substrate to cause a hydrophilic inclination within the substrate. [24] A solution of nitric acid and polyvinylpyrrolidone (PVP) can be used to etch and create a hydrophilic surface on the polyethylene terephthalate film (Mylar®).

Particulate matter from the atmosphere can be collected with polycarbonate filters like a clean mylar film left in a desired environment for several hours.

Specimen heating caused by beam energy being lost within a sample can cause the vaporization of organic and trace element targets. It is recommended that for thin

specimens under vacuum, the proton beam current density should not surpass  $5nA/mm^2$ . [24] Radiation damage to polycarbonate substrates is largely unnoticeable after proton irradiation, but after oxygen is reintroduced to the evacuated target chamber, it diffuses into the polycarbonate filter and reacts with free radicals caused by proton irradiation. [18] Radiation damage becomes evident, when holes form in the filter.

Between the elements of atomic number  $20 \leq Z \leq 30$ , detection limit for  $K$  x-rays is at its lowest, but  $L$  x-rays are prevalent between  $70 \leq Z \leq 80$ . These limits get slightly higher in atomic number as proton energy increases. PIXE analysis is an inadequate technique for many of the rare earth elements ( $Z=57-69$ ), as they fall between the two windows of optimal detection. [18]

## **2. Experimental Methods**

### **2.1 Proton Beam Creation**

Creating an ion beam capable of reaching energies of several *MeV* necessitates many phases of beam manipulation that begins at the ion source and ends at the experimental apparatus. Ions must be created, selected, focused, accelerated, and guided through a high vacuum environment before it ever reaches an experimental target chamber. To begin, it is appropriate to start with a consideration of how ions are created.

#### **2.1.1 Cesium Sputter Source**

Ions are created through a sputtering process involving cesium vapor. The sputter process ensues when a solid target material is bombarded by energetic particles. As this method occurs, atoms from the solid target are ejected due to the transfer of momentum between the energetic particles and the target's atoms which cause collision cascades within the target material. Upon recoil of these cascades, and when reaching the target surface, if the particle has an energy above the surface binding energy, atoms are liberated from the material. Since a great amount of momentum is needed for this reaction to occur, the heavy cesium ion is preferred over other elements. Additionally, cesium has an abundance of free electrons that are available to donate to the sputtered atoms. ECU uses a High Intensity General Ionics Corporation 860 A Cesium sputter ion source which was founded by Middleton in the early 80's. [25] This source can create ions from nearly all elements, excluding noble gasses, and can achieve currents in the range of hundreds of  $\mu$ -amps. [26, 27] To

generate the proton ( $H^+$ ) beam required for PIXE, it is necessary to create  $H^-$  ions with the source. To accomplish this, a small amount of  $TiH_2$  powder is firmly packed into a copper target cathode. The sputtering process begins when solid cesium is heated in an oven set around 350 K. To ensure that no cesium condensation can clog the valve, the valve is held at a higher temperature than oven itself. Consequently, cesium vapor is released into a chamber containing a cooled cathode held at a -7.5-kV bias and an extremely hot ( $\sim 1375$  K) tantalum ionizing coil. [25] These components are arranged opposite of the sputter chamber with respect to each other. The cathode is held at a lower temperature so that some of the cesium vapor will condense on it. On the other end of the chamber, through the process of thermal emission, cesium vapor is ionized as the tantalum coil boils off electrons from the cesium vapor by means of thermal ionization. As the cesium vapor is changed into positively charged  $Cs^+$  ions, they are accelerated through a potential difference of  $\sim 2$  kV where they are forced to bombard the cooled and negatively biased sputter cathode. This phenomenon occurs as per Coulomb's law

$$F_C = Eq' \quad (16)$$

where,

$$E = \frac{\Delta V}{d} \quad (17)$$

Where  $F_C$  represents Coulomb force,  $E$  denotes electric field,  $q'$  is a charge immersed in the electric field,  $\Delta V$  denotes the voltage potential difference between two charged objects, and the distance between the charged objects is given by  $d$ .

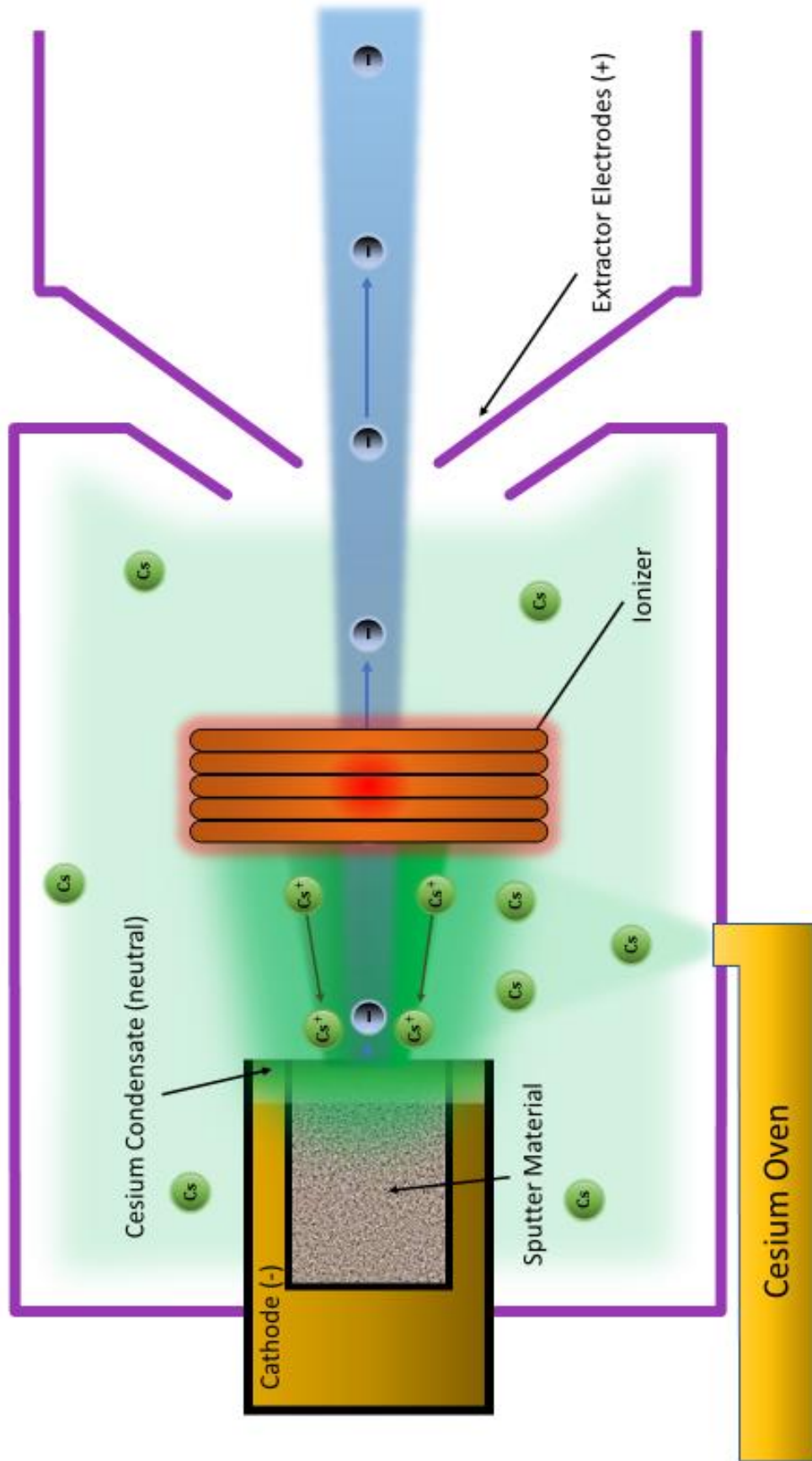


Figure (9). Diagram of Cesium Sputter Source.

After ionized cesium is accelerated through the potential difference, the positive cesium ions slam into the copper sputter cathode packed with titanium hydride; consequently, a multitude of differing molecular species are sputtered from the  $TiH_2$  and the copper housing. [28] Many of these sputtered particles are atoms that become negatively charged when they pick up electrons after collisions with cesium atoms previously condensed on the cooled surface of the cathode. Since the cathode is held at a negative potential, the newly created negatively charged ions accelerate away from the cathode, and by means of extractor electrodes held at a higher voltage potential with respect to the cathode; subsequently, the ions have an approximate energy of 6  $keV$  at this stage. Following this, without altering beam energy, an electrostatic unipotential lens, or Einzel lens, is used to focus the ions before passing through the 30- $kV$  acceleration tube.

After vertical guidance of the ion beam through use of a magnetic field, it is necessary that the  $\sim 36 keV H^-$  ions are isolated from the unwanted molecular species emitted from the previous sputtering process. The ions that emerge from the linear accelerator all have different momenta including the  $H^-$  ions. To capitalize on this, the beam line encounters a  $25^\circ$  bend selector magnet. The magnet ensures that only certain species of specific mass and velocity can negotiate the arc of the turn. The intensity of the magnetic field determines which ion species passes the  $25^\circ$  deflection successfully. Essentially, the inflection magnet selects ions that have the same magnetic rigidity by:

$$Br = \sqrt{2mE/q^2} \quad (18)$$

Where  $mE$  indicates particle mass and energy,  $q$  is the ionic charge,  $r$  denotes radius of curvature, and  $B$  designates the magnetic induction field.

The manipulation of the beam is brought about by Lorentz forces, and can be understood by the equation:

$$F_L = q[E + (v \times B)] \quad (19)$$

The Lorentz force  $F_L$  acts on a particle of electric charge  $q$  with a velocity  $v$  due to an external electric field  $E$  – in this case,  $0 \text{ N/C}$  – and magnetic field  $B$ .

With ECU's inflection magnet setup, the desired ions need to acquire a counterclockwise trajectory as they round the bend. Therefore, an adjustable upward oriented magnetic field is used to “filter” out the undesired particles, while allowing the sought after  $H^-$  ions to pass through the bend. The Lorentz force can be equated to a centripetal force in this instance by:

$$F_C = qvB \sin \theta = m \frac{v^2}{r} \quad (20)$$

Where  $m$  indicates the mass of the ion,  $r$  represents the radius of the ion's trajectory while in the magnetic field, and  $\theta$  being the orientation of the magnetic field with respect to the velocity of the particle, namely  $90^\circ$ . Ion momentums are all different upon entrance into the selector magnet's field, and therefore the Lorentz force serves to isolate the proper ion species. This is exhibited with a rearrangement of the cyclotron formula:

$$B = \frac{mv}{qr} \quad (21)$$

To allow effective passage of  $H^-$  ions through the bend, the correct magnetic field is tuned using the inflection magnet. Other unwanted ions travel with too large of a radius and end their flight by striking the walls of the beam line; the nonessential ions are basically “filtered” out by the selector magnet. At this juncture, the  $H^-$  ions encounter a second, low energy, Einzel lens, and an electrostatic steerer to augment beam transmission into the tandem accelerator, as shown in figure (10).

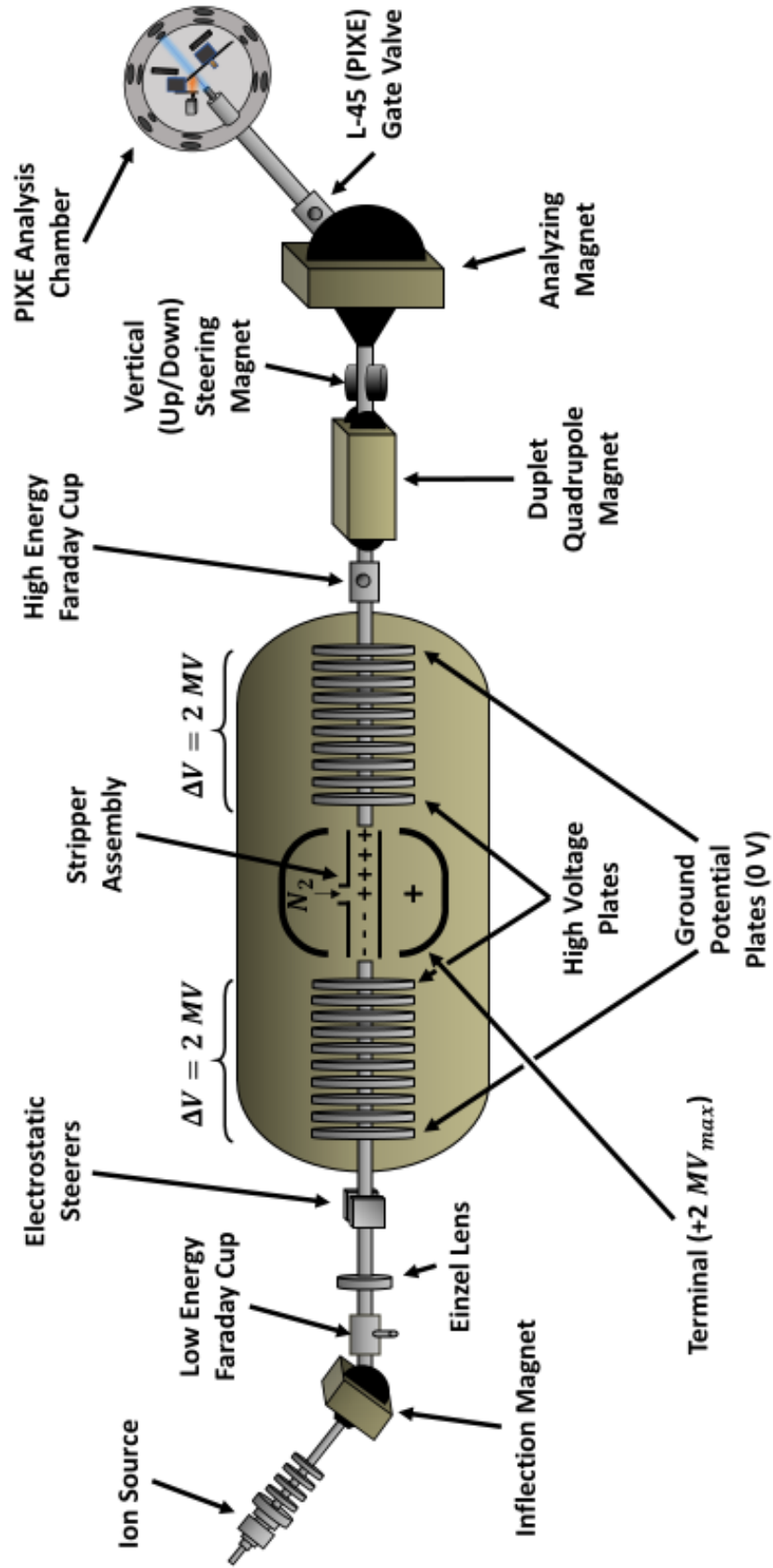


Figure (10). Diagram of ECU's Particle accelerator and PIXE system.

### 2.1.2 Pelletron Tandem Particle Accelerator

The Tandem NEC 6SDH-2 Pelletron model 2AA0&2310 Accelerator used in the calibration of East Carolina University's PIXE apparatus, is capable of operating at a charged terminal voltage of 2 MV. As shown schematically in figure (10). The accelerator is made up of multiple systems including charging chains, high voltage plates, a high voltage terminal, vacuum pumps, water cooling components, a beam line, and a gas circulation system. All this, among other mechanisms that make up the accelerator, are contained in a large 4 m long cylindrical tank.

The Pelletron is very similar to a Van de Graaff accelerator in that it operates on the same physical principles. The difference between the Pelletron design and the Van de Graaff design is that the Pelletron has a pellet chain, short conductive tubes joined by electrically insulated links, whereas the Van de Graaff generator uses a charging belt. The Pelletron chain design is superior to a charging belt, since it allows for a more uniform charge distribution, which allows for a higher stability of the terminal voltage, and, therefore, allows for a more stable particle energy. The chain can also move at much higher velocities than a belt; naturally, this leads to more accumulation of charge on the terminal. This increased up-charge allows for higher beam currents.

The Pelletron chains are made up of links containing metal pellets coupled with nylon links that have electrically insulative properties. By means of an induction system that does not incorporate corona discharges or brushing contacts, the high voltage terminal of ECU's Pelletron is positively charged. The charging process begins when the negatively-charged inductor electrode forces electrons off the metal pellets while they have electrical continuity with the grounded drive pulley. Since they are still in the

negative induction field, as the pellets lose contact with the pulley they continue to hold a net positive charge. Subsequently, the chain delivers the positive charge to the high-voltage terminal, as the chain arrives at the terminal, the chain once again passes through a negatively biased suppressor electrode to impede arcing as it becomes electrically common with the terminal pulley. While in the negatively biased suppressor region, the pellets efficiently deposit charge on the pulley, in turn, giving the terminal a net positive charge. [29-31]

To develop a uniform electric potential gradient within the accelerator beam tube, on either side of the central high voltage terminal, there is a series of high voltage plates that are sequentially located to progressively step the voltage down to 0 V on both ends of the accelerator tank, as shown in figure (10).

The hollow terminal will accumulate positive charge which is controlled by the up-charge and the column currents, along with the current from beam loading. Sparking will occur if until there is enough potential to overcome the breakdown voltage of the gas that it is immersed in. The breakdown voltage of air at STP is  $\sim 2.38 \times 10^6 \text{ V/m}$  between two plane surfaces at 5 mm apart. In this type of electric field, air will ionize becoming conductive plasma, and accumulated charge will arc to the nearest object of lower potential. The breakdown voltage of gas is specific to the chemical makeup of the gas, and a charged terminal can be held at higher potentials depending on the insulative properties and pressure of the gas surrounding it. With the high voltages that the terminal can achieve, and in consideration of the proximity of the terminal relative to other conductive components of differing voltage potentials, at a pressure of about 550

$kPa$ , the volume of space containing the accelerator's high voltage components and ground points is flooded with sulfur hexafluoride gas.

$SF_6$  is a gaseous dielectric that acts as a superior electrical insulator, it is also nontoxic and chemically stable. ECU's accelerator utilizes this gas to prevent corona discharges; arcing will give way to an unstable terminal voltage and will inevitably cause damage to internal components.  $SF_6$  has an electrically insulative property that allows for a very high breakdown voltage – approximately three times that of air at STP (2.95 @ 5 mm between charged surfaces). The breakdown voltage for  $SF_6$  is increased even further by pressurizing the gas.

The pressure of the  $SF_6$  gas is limited to the vacuum seals that are installed on the beamline and, primarily, the pressure seals of the tank; if the  $SF_6$  pressure is too great this will create a high-pressure differential and the high vacuum environment in the beam line may be breached by the  $SF_6$ . Consequently, the ion beam will become scattered and eventually stopped by collisions with the  $SF_6$  molecules found within the beam line.  $SF_6$  gets hot during normal operation, and a temperature increase of the insulating gas will lend itself to a degraded breakdown voltage, so a water-cooling system is used to regulate the temperature of the insulating gas.

The tandem accelerator is so named because it has two stages of acceleration. The negative ions are accelerated toward the positive terminal as they enter the tank. When the ions reach the geometric center of the tank, they enter a gas assembly containing  $N_2$  gas which is used to strip them of their electrons. Nitrogen gas is used because of its high electronegativity (affinity for electrons) and low-cost.

This electron stripping process occurs when an  $H^-$  ion beam enters the gas assembly, and after subjection to nitrogen gas, the negative ion beam becomes a positive ion, or proton ( $H^+$ ), beam. The newly formed proton beam is subsequently accelerated away from the positive terminal in the second stage of the acceleration. This means that if the terminal was adjusted to have a potential of 2 MV, the singly charged  $H^-$  ion would be given 2 MeV of energy during its first stage of acceleration. After the negatively charged ion is stripped of electrons it becomes a proton, and it is forced away from the positively charged terminal and moves downstream toward the grounded high-energy side of the accelerator. The second acceleration gives the proton an additional 2 MeV of energy, and this yields a total proton energy of 4 MeV upon emergence from the accelerator.

The proton beam is focused before it arrives downstream at the experimental apparatus. A quadrupole magnet acts much like a lens to a beam of light. Through a duplet configuration of quadrupole magnets, the beam is constrained both horizontally (width) and vertically (height) resulting in a highly focused proton beam. The focused protons will allow for a higher beam current that will cause more collisions with target material. Conversely, if the ion beam current is too high the quadrupole can be used to defocus the beam yielding fewer proton-target interactions, which may decrease the count rate within the detector.

After leaving the field generated by the two quadrupole magnets, the beam undergoes a final vertical alignment through use of a vertical steering magnet. The vertical steering magnet ensures that the beam will be vertically aligned with the target as shown in figure (10).

Following the vertical alignment, the protons encounter a final magnetic field that is induced by a switching, or analyzing, magnet. This magnet essentially selects one of the seven experimental beam lines for the protons to travel down. The PIXE apparatus is located on the leftmost 45-degree beamline (L-45); the switching magnet guides the ions in this direction. After clearing the magnet, the beam must pass through a manually operated gate valve which is purposed to isolate the PIXE apparatus from the tandem accelerator and other experimental beam lines. This valve protects the other experiments and the accelerator from vacuum failure within the PIXE chamber or anywhere beyond the switching manifold. If the valve is open, the beam travels down the last segment of drift tube and appears in the proton induced x-ray emission analysis chamber, as shown schematically in figure (10). Beam current can be measured at this point with the Faraday cup located in the back of the chamber if the sample wheel is empty and in the correct position.

At several points between the source and experiment, the beam's physical shape and beam current can be monitored using quartz crystal scintillators and Faraday cups. Scintillators that can be moved in and out of the beam path will fluoresce when irradiated with charged particles, this allows for the observation of the physical shape of the beam profile. Faraday cups are conductive metal cups that are used to measure the beam current. Faraday cups allow for the measurement of beam current at the low energy side of the line (before the accelerator) and the high energy side of the line (after the accelerator), and also inside the PIXE chamber. Like the quartz viewers, the Faraday cups can be positioned in or out of the path of the ion beam. The transmission

rate has been observed at an approximate maximum of 80% between  $H^-$  ions and protons collected in ECU's low and high energy Faraday cups.

By utilizing several turbomolecular pumps situated at different points along the drift line. High energy ions can be transported from the source to the experimental chamber via high vacuum conduit. To minimize collision probability between protons and gas molecules in the beam line, a vacuum is maintained at pressures of approximately  $10^{-7}$  Torr ( $10^{-5}$  Pa) inside the chamber. At  $10^{-1}$  to  $10^{-2}$  Pa, beam loss for protons is insignificant. However, in efforts to increase the mean free path of fast ions, the beam lines, starting from sputter source and ending at the target, are held under high vacuum, typically on the order of  $10^{-8}$  Torr ( $10^{-6}$  Pa).

To prevent collisions with residual gas, the PIXE target chamber vacuum is maintained between  $10^{-6}$  and  $10^{-7}$  Torr ( $\sim 10^{-4}$  Pa). Beam halo brought about by scattering inside of the target chamber will distort the beam profile and may increase the intensity of background peaks in the spectra. [20]

The experimental chamber and drift tube are made from rigid materials that can withstand high pressure differentials all while maintaining low outgassing rates and vapor pressures; specifically, stainless steel, aluminum, and plexiglass as depicted in figures (11a -- d). [20]

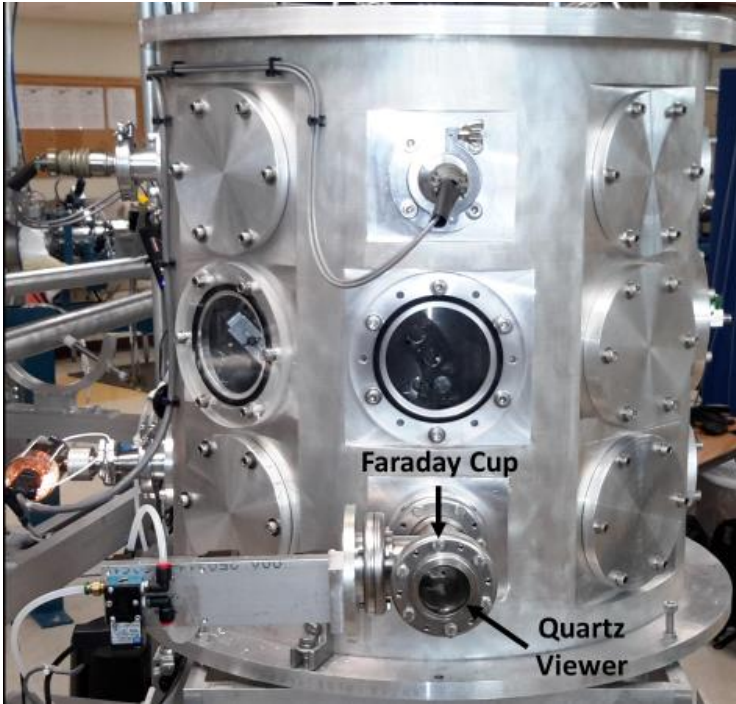


Figure (11a). Exterior view of the target chamber.

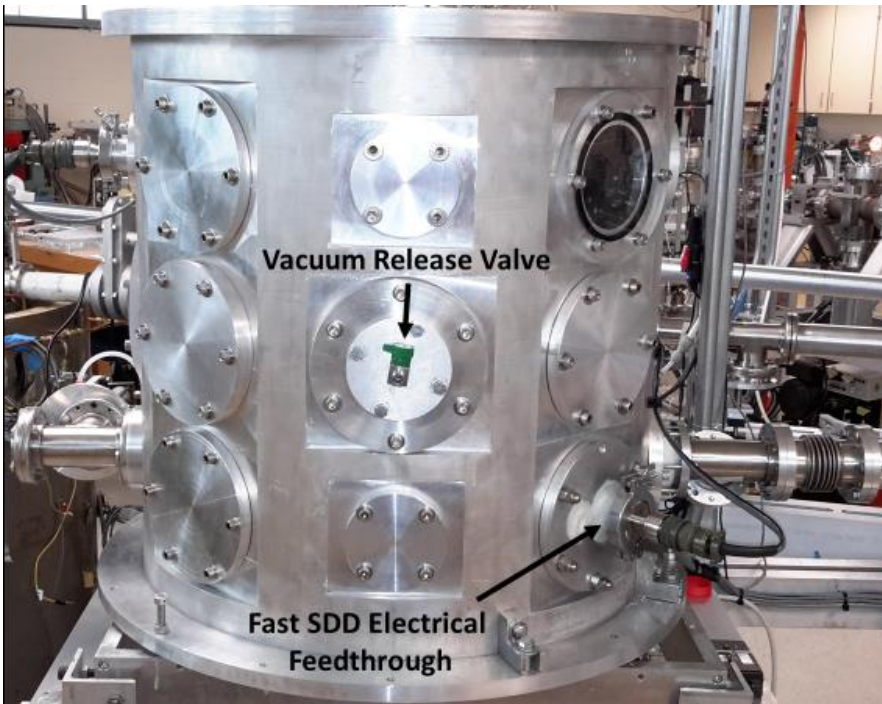


Figure (11b). Exterior view of the target chamber.

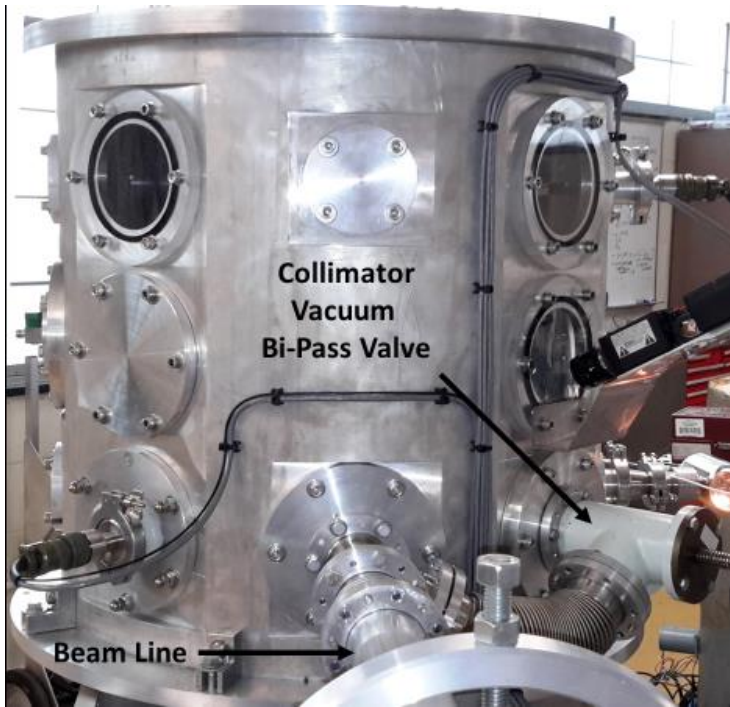


Figure (11c). Exterior view of the target chamber.

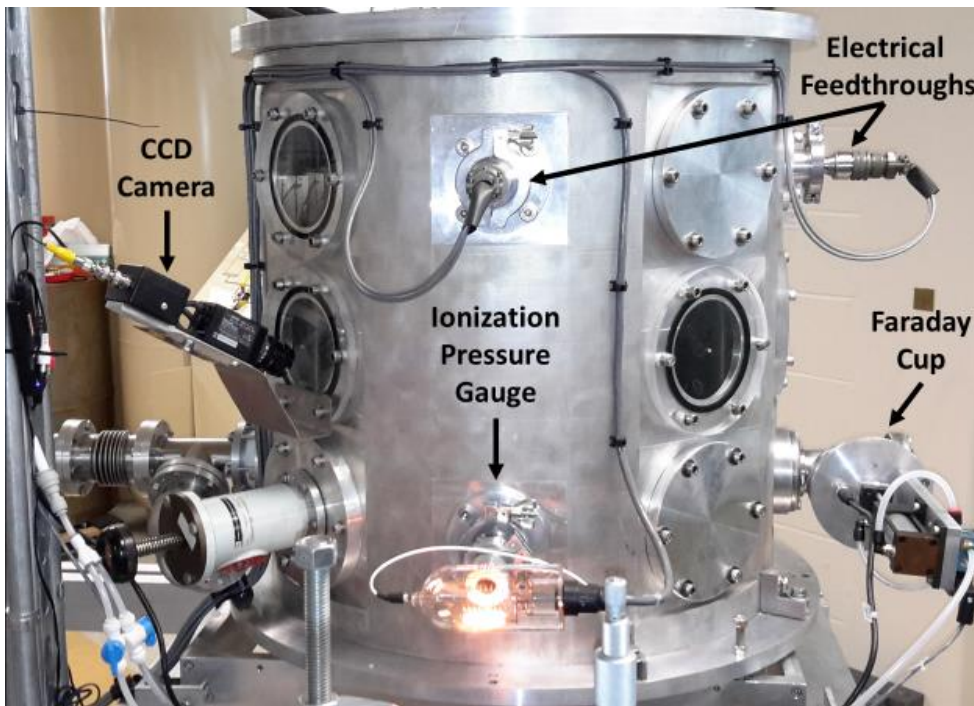


Figure (11d). Exterior view of the target chamber.

To bring the chamber down to  $10^{-4}$  Pa, a mechanical pump is used for rough and exhaust pumping, while a turbomolecular pump brings the PIXE apparatus to its operational pressure. The Turbomolecular pump is a good option as it does not risk chamber/sample contamination like an oil diffusion pump, and it can bring the chamber to vacuum relatively quickly – this is important if many samples are expected to be analyzed quickly. A disadvantage to the turbomolecular pump: while under operation, the mechanical bearings of the turbomolecular pump cause vibrations throughout the PIXE chamber, and this can potentially affect the energy resolution of the Silicon Drift Diode detector. [20]

Ion/energy	Range in air (mm)	$\Delta E$ (keV/ $\mu\text{m}$ ) in air, or $\Delta E$ (eV/m) in vacuum $10^{-4}$ Pa
p, 1 MeV	23.25	0.0273
p, 2 MeV	71.25	0.0169
p, 3 MeV	140.52	0.0126

Table (4). Proton energy attenuation in air and vacuum.

### 2.1.3 PIXE Beam Requirements

Protons with energies between 1-3 *MeV* are typically used in PIXE analysis. The beam current correlates directly with count rate. Less than 1  $\mu A$  of beam current is needed for successful PIXE analysis. [20] Some specimens, such as those prepared from powder or solution, have irregular thicknesses and nonhomogeneous surfaces, so it is important to attain a uniform intensity distribution across the beam. [18] This can be achieved by defocusing the beam with the magnetic quadrupole, and then collimating its gaussian intensity distribution in such a way that the charge flux will be nearly uniform within the cross-sectional area of the proton beam. This technique causes a diminished beam current at the sample, so the accelerator needs to supply several hundred nanoamperes on the high energy side.

## 2.2 Target Chamber

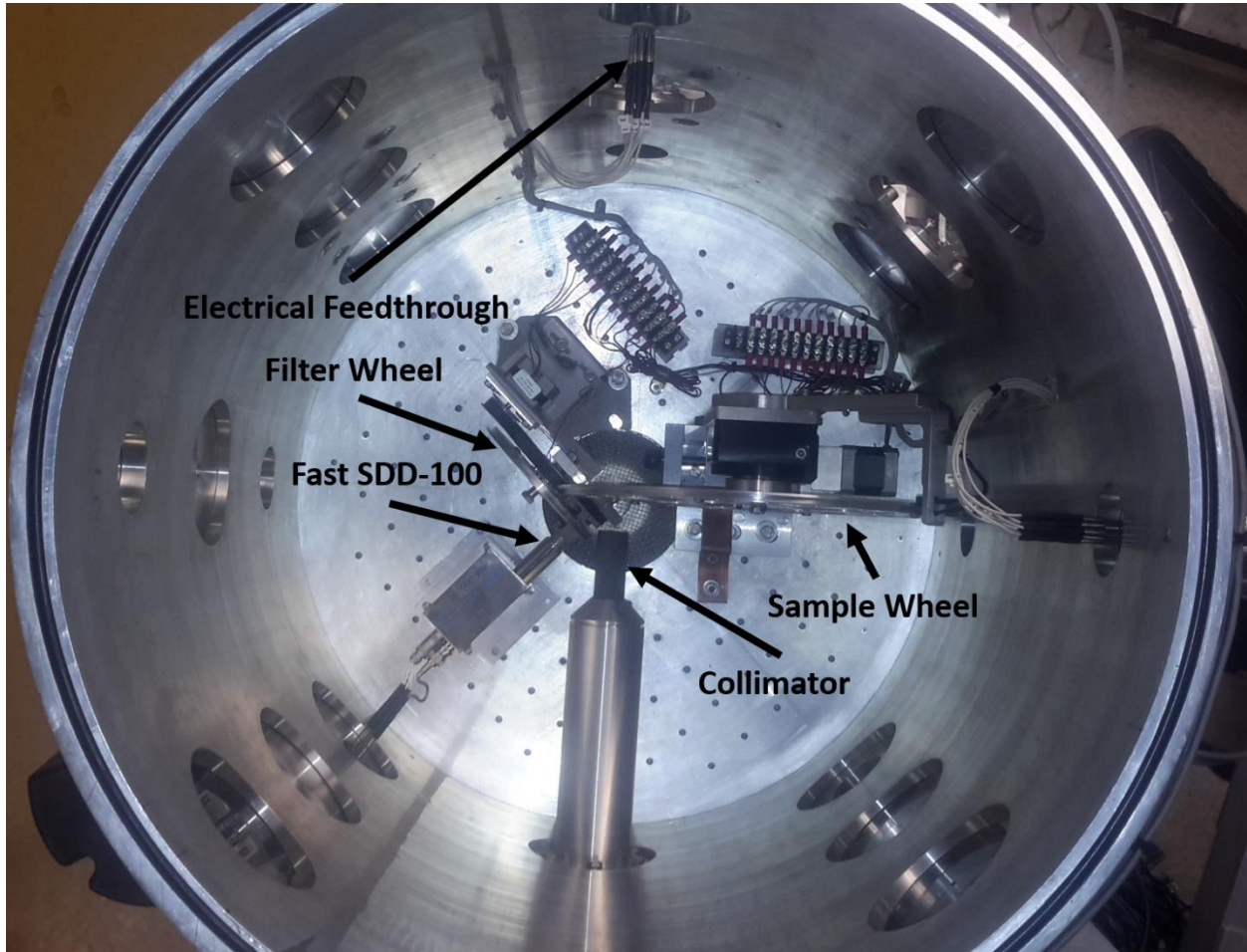


Figure (12). Bird's eye view of the inside of the PIXE target chamber.

### 2.2.1 Chamber Specifications

The chamber and metal flanges are all made from aluminum and held together with stainless steel hex head bolts. There are nine blank flanges, but the other flanges accommodate five portholes, five adapters, two valves, and a drift tube; these are all attached directly to the chamber, and they maintain vacuum through the use of Viton O-rings. The base and lid are also outfitted with Viton O-rings. The ion gauge, Faraday cup, and all Electrical feedthroughs rely on KF vacuum fittings. The only Conflat fitting is

located between the gate valve and the L-45 PIXE drift line. All the components within the chamber are bolted down to the aluminum base of the chamber. The PIXE apparatus uses a Kurt J. Lesker G075K Ion Gauge that is controlled with a Varian BA2 SENTORR gauge controller to monitor pressure within the chamber.

The chamber uses an Agilent Technologies DS 302 Roughing pump to evacuate the fore-line. The chamber is brought to high vacuum with a Leibold and Harris TURBOVAC 360 turbomolecular pump that is controlled with a Turbotronic NT 150/360 turbomolecular pump controller. The turbomolecular pump is located at the base of the chamber with the intake facing up. Only a very coarse screen separates the volume of the chamber from the blades of the pump, so care should be taken in preventing debris from falling into the pump.

There are four valves associated with the PIXE chamber. Attached between the selector magnet manifold and the drift tube attached to the PIXE chamber is a manually operated gate valve. The gate valve serves to isolate the accelerator and other experiments from the PIXE beam line. In a situation where vacuum is lost within the PIXE chamber during a period of non-use, other experimental lines, and the accelerator itself, will be protected. The second safeguard is a pneumatic valve located on the turbomolecular pump's exhaust port. This valve isolates the fore-line from the turbomolecular pump and is of convenient configuration when performing maintenance to the fore-line while desiring to keep vacuum in the chamber. An additional valve is located under the CCD camera mounted on the chamber. This should be open during initial evacuation of the chamber. This allows gas to travel from the drift line directly to the chamber in lieu of evacuating gas through only the small hole of the collimator.

Leaving this valve open will reduce evacuation time. A relief valve is used to *gradually* bring the chamber back up to atmosphere. This is important because the air velocity entering the chamber when the valve is completely open can disturb and fleck off pieces of delicate samples into the blades of the precision turbomolecular pump.

In the interests of economic analysis, most chambers have multi-specimen capability. ECU's sample carousel arrangement allows for the analysis of up to 24 specimens as shown in figure (13).



Figure (13). Image of ECU's PIXE Sample Carousel.

The target chamber houses an automated target wheel driven by stepper motors connected to LabView Software installed on the data acquisition computer. The wheel is positioned orthogonal to the incoming ion beam and this geometry is held constant. The cross section of the collimated beam is significantly smaller than the cross section of the sample holder frame, this serves to minimize background. The sample wheel contains 24 individual sample positions and can be moved translationally (it can move the sample laterally with respect to the beam), and rotationally (clockwise and counterclockwise) to select the desired target. The graphite beam collimator is approximately 0.635 cm in diameter and is located approximately 2.858 cm away from the sample wheel. The wheel is secured with a thumbscrew and can be easily removed after the filter wheel is taken off its mount. There are 24 small (1 mm diameter) holes in the outer circumference of the wheel. These holes allow the optical interrupter switch (H21B1) to detect target positioning. The samples are held with an outer steel ring. Before samples are loaded into the wheel this ring must be removed, as shown in figure (13).

The original construction of the sample wheel isolates it from earth ground. If steps are not taken to provide continuous discharge of the specimens then they will undergo a cyclic buildup of charge. This discharge occurs as a spark. The positive potential attracts electrons, whose interaction results in an intense additional bremsstrahlung background contribution in the x-ray spectrum. To remedy this, a copper grounding brush was attached to the base of the chamber. Without impeding sample wheel operation, the brush slides along the wheel as it rotates, yet it maintains continuity with the sample wheel in any position. It may be beneficial to coat specimens

with a thin conducting layer of carbon if they do not achieve electrical continuity with the sample wheel, or earth ground. [18]

With specimens thick enough to stop the beam entirely, the specimen holder must be insulated from the chamber, and the specimen should be connected directly to a charge integrator. [18]

Provision is necessary for the insertion of a suite of x-ray absorbing filters between specimen and detector. By filtering intense x-ray peaks, other trace elements can be identified, and pile up can also be reduced. The use of such filters emphasize certain spectral energy regions at the expense of other regions of low information content. [19]

The filter wheel has similar features to the sample wheel. The filter holder has six positions and can be rotated counter and clockwise. Like the sample wheel, position alignment for the filter wheel is detected with an optical interrupter switch, as shown in figure (14).

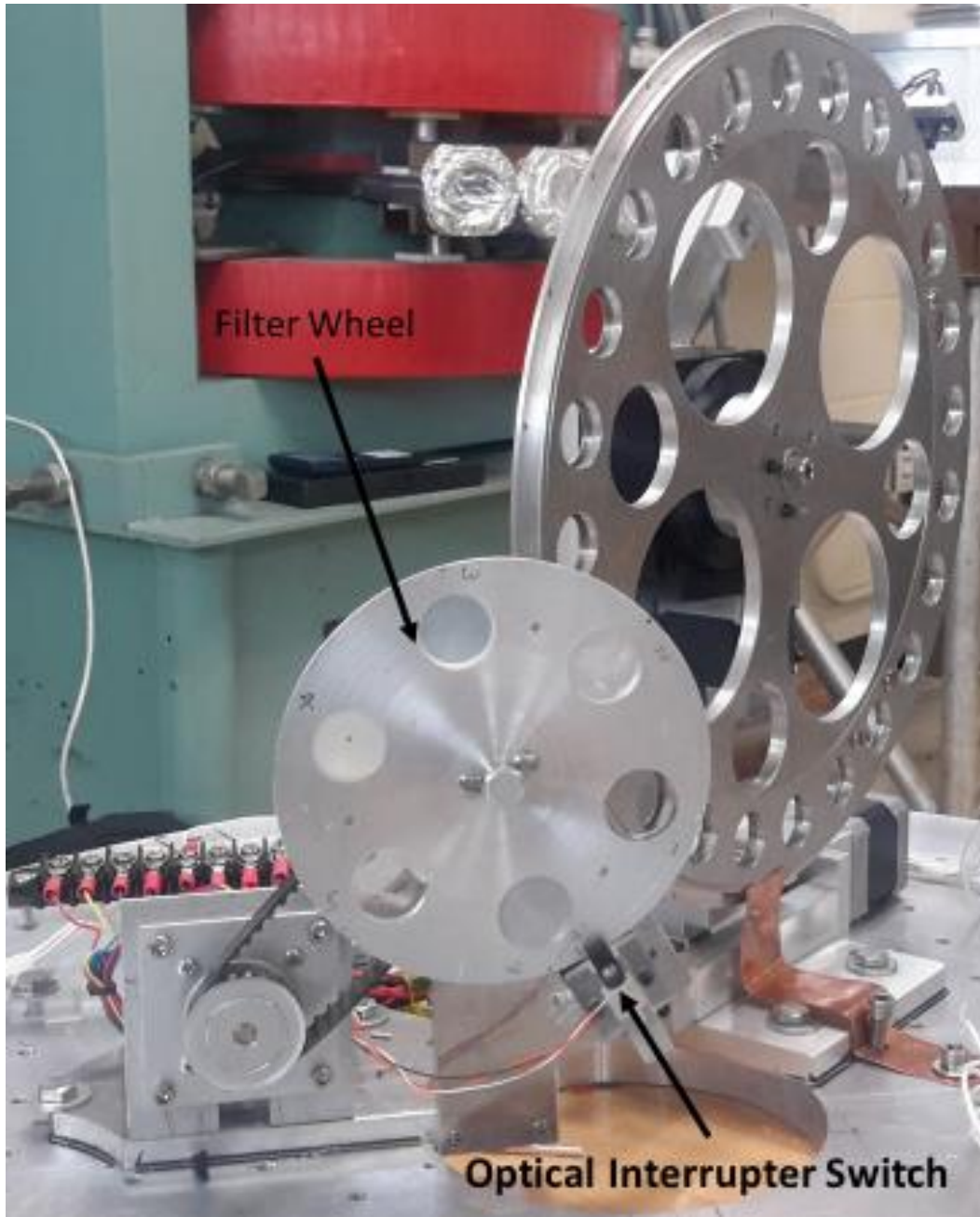


Figure (14). Filter wheel and sample wheel in background.

The sample and filter wheels are rotated by means of a stepping motor, and the translational movement of the sample wheel is controlled by a Vexta PK245-03AA, 12V, 0.4 A motor. Motor speed and direction can be controlled remotely by means of the Lab View 2017, Version 17.0.1F1 (64-bit) interface. Lab View communicates with optical sensors mounted on the sample and filter wheels to indicate if the sample or filter is in its correct position. A green indicator light turns on when the target is lined up, and a green alarm light flashes if the translational motor reaches its boundary limits. Going beyond the sample wheel's translational constraints can damage the translational motor, the filter, or sample wheel. To operate the motors, the National Instruments USB X-series USB-6341 USB hub must be turned on first, and then the motor driver module must be switched on. The Lab View software should be initiated last.

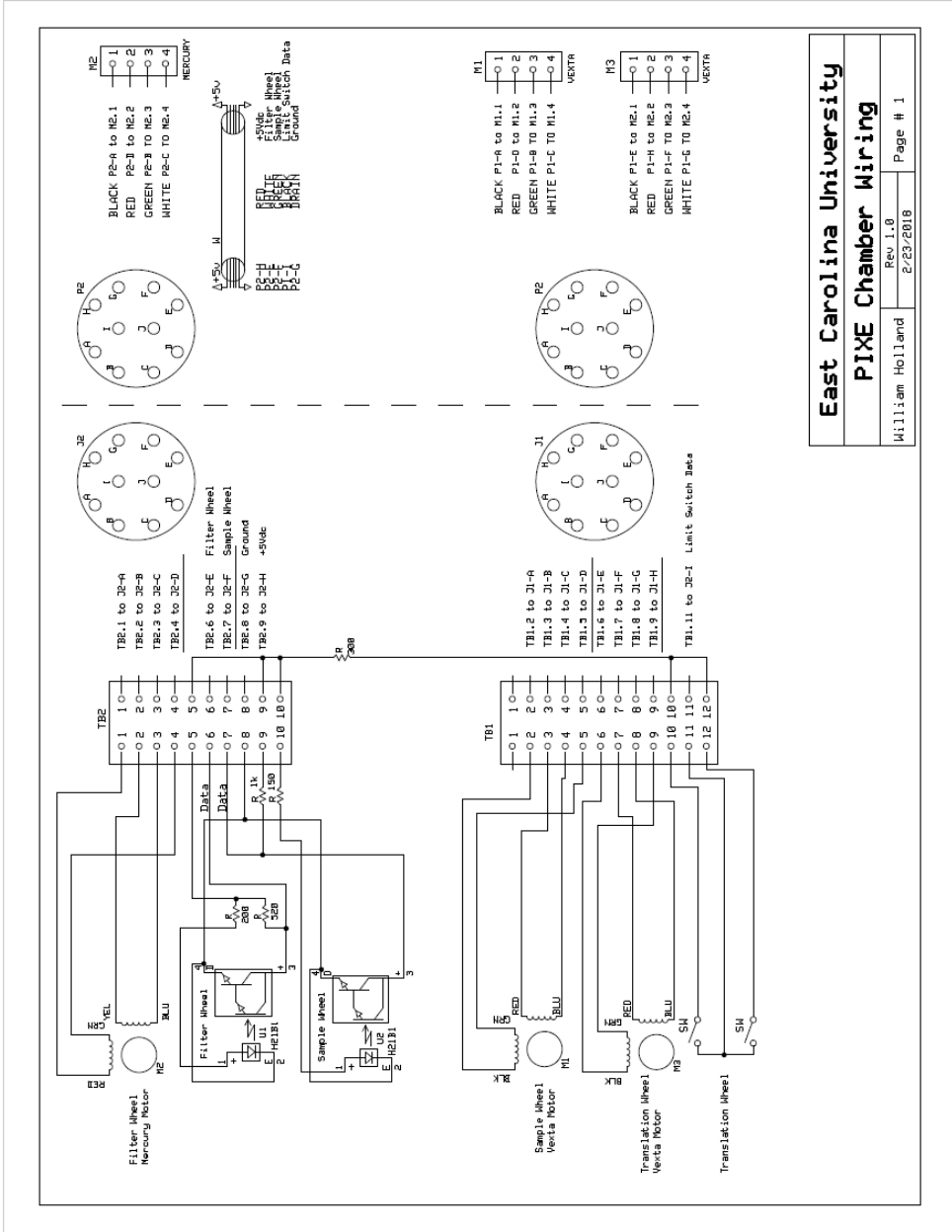


Figure (15). Motor and optical interrupter switch electrical diagram.

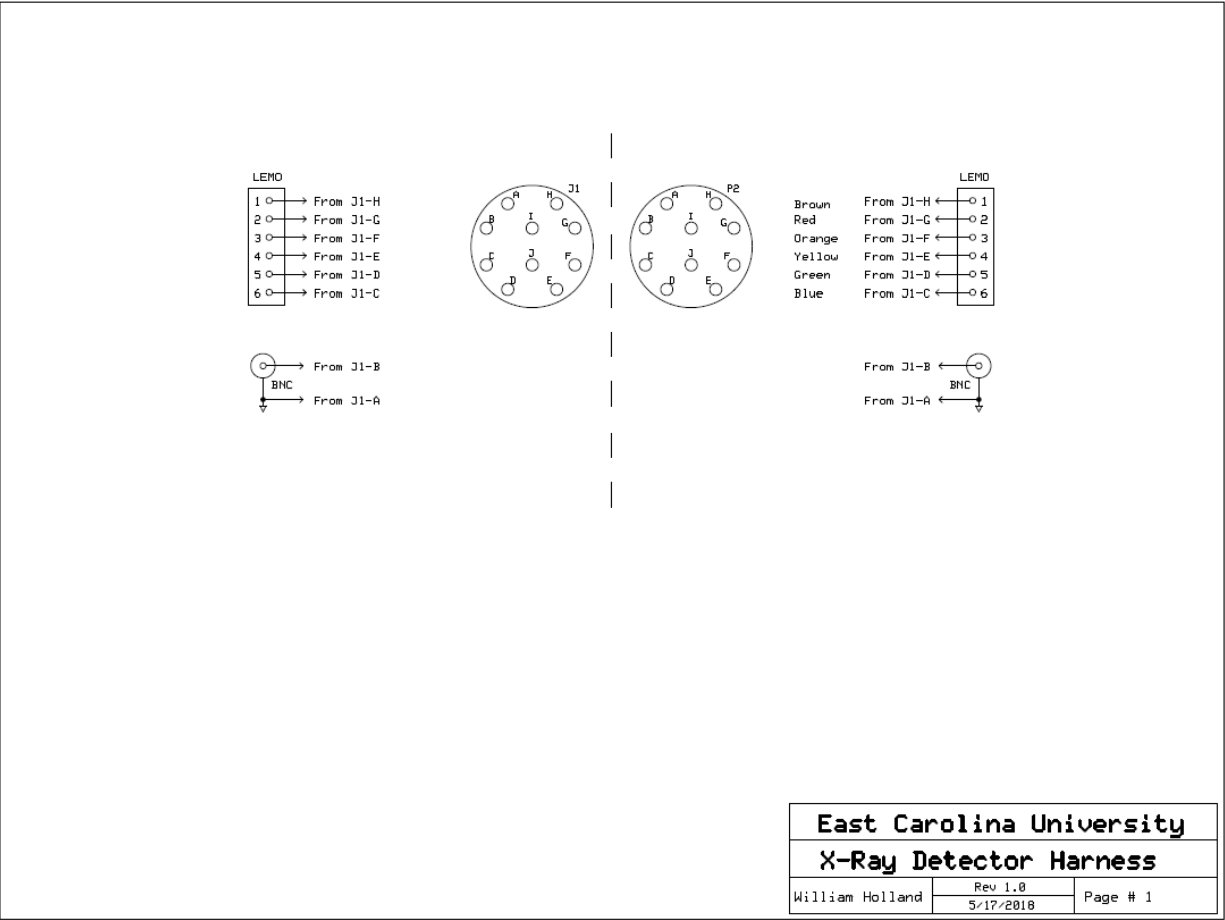


Figure (16). Lemo connector to electrical feedthrough diagram.

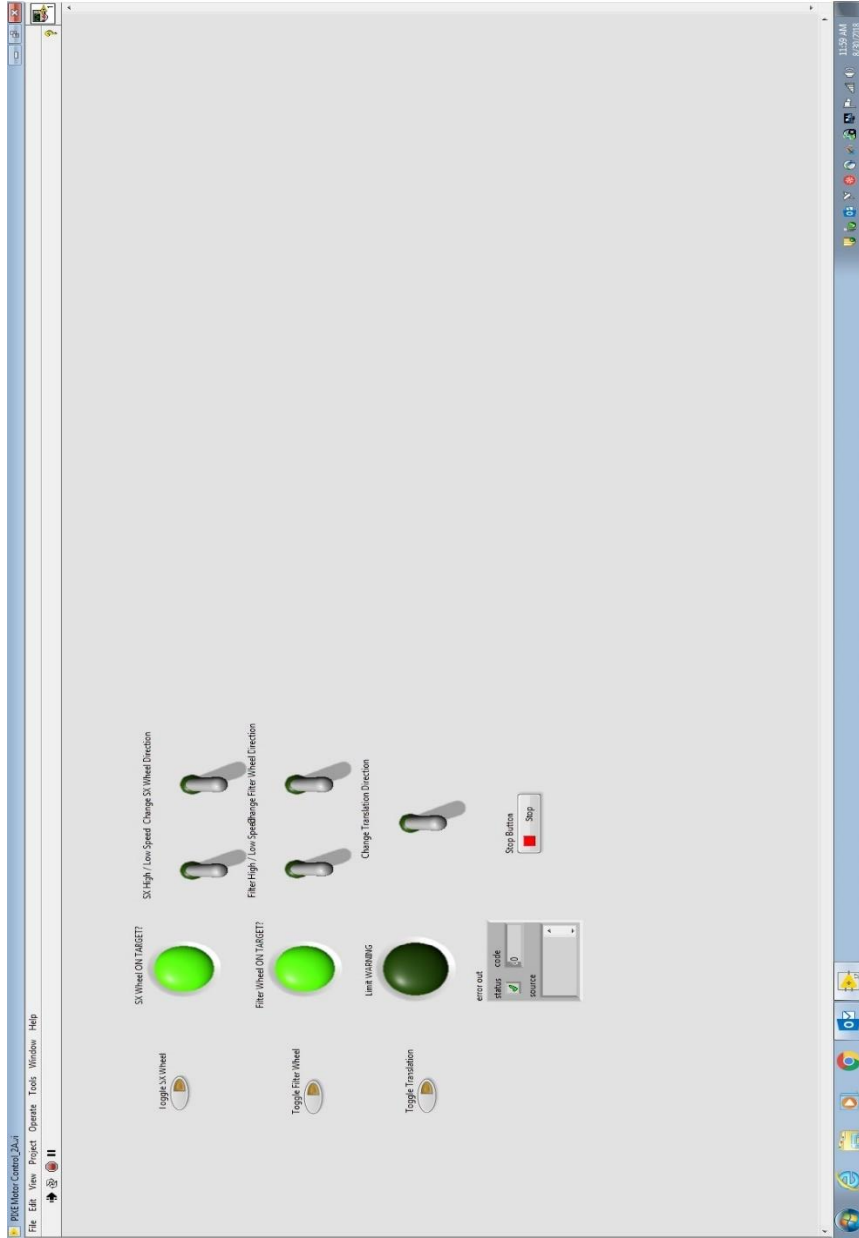


Figure (17). Lab VIEW motor control interface.

### 2.2.2 Chamber Monitoring

Five portholes are strategically mounted on the chamber walls to allow for direct visual inspection of the chamber environment. To attain precise sample positioning with respect to the beam, a CCD camera is positioned to view the sample surface. With EZ Grabber V3.0 software and a Panasonic GP-MF552 B/W CCD camera attached to the center porthole on the northeast side of the chamber, the operator is allowed remote viewing at the data acquisition PC. The black and white camera is focused at the point where the proton beam meets the target. The sample wheel, sample number, filter wheel, collimator and beryllium detector window can all be viewed from this vantage point. This camera configuration allows for efficient and safe viewing of the sample while under analysis and between runs; this arrangement lets the operator see the beam, aids in selecting the target, and helps in adjusting the physical position of the target.

To monitor beam current, a Faraday cup is located at the back of the chamber. The cup itself is made from carbon, and it is operated with a pneumatic valve that allows motion into or out of the beam path. The Faraday cup can be controlled, and the beam current data can be viewed, remotely with the accelerator interface software. A quartz viewer is located directly downstream of the faraday cup. The cup must be moved out of the beam path to view the beam spot at the back of the chamber.

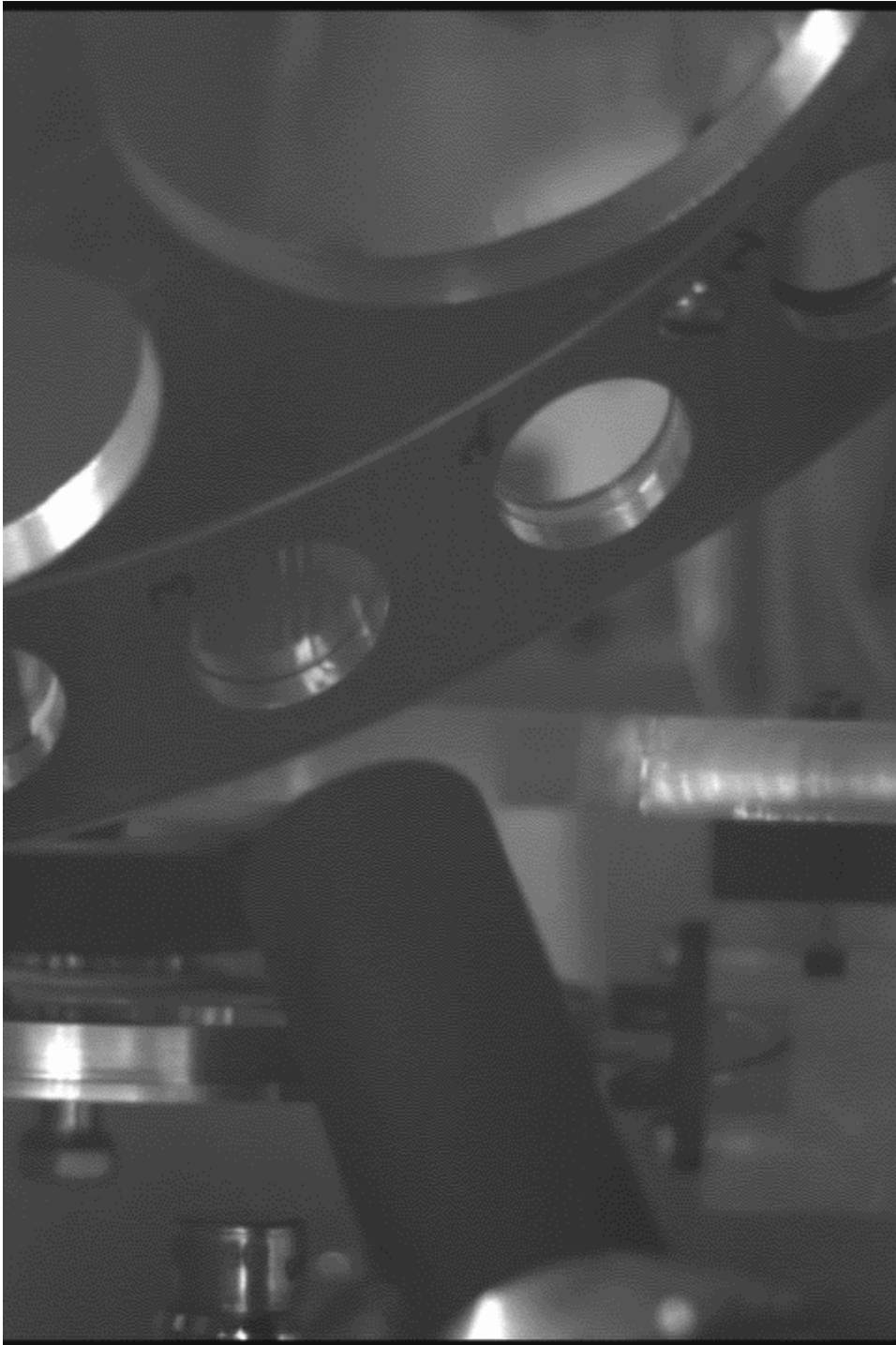


Figure (18). View from ECU's PIXE CCD camera

### 2.2.3 Collimators

To create an appropriate beam spot in probing the target composition, it is necessary to focus and collimate the beam. The profile of the ion beam should ideally have a uniform distribution upon emergence into the chamber, but it is collimated to achieve a uniform current distribution along the cross section of the beam. A series of collimators dictate the shape of the beam's cross section. In ECU's PIXE apparatus, the first collimator is located inside the incoming beam tube; it adjusts the shape of the beam. The second collimator acts as an anti-scattering collimator that will shear off disbanding protons. Failing to collimate a second time will result in x-rays being emitted from chamber materials that are in line-of-sight to the beryllium window of the detector. This can negatively affect spectra. Since much of the beam is collimated before hitting a sample, it is important to generate a much higher current from the low energy side of the accelerator.

Collimators are preferably fabricated from elements that do not give rise to unwanted x or  $\gamma$ -rays via the  $(p, \gamma)$  reaction. x and  $\gamma$ -rays will increase the continuous background within a given x-ray detector. [18]

Near the detector, carbon (graphite), which emits no detectable x-rays, is the general choice for beam collimation. Even though proton energies above 3.236 MeV are out of the typical range for PIXE, protons at these energies will cause neutron production in the carbon collimator.

### **2.2.4 Detector Positioning**

The geometrical arrangement of components located within the PIXE chamber will greatly affect x-ray attenuation, beam energy loss, and bremsstrahlung emissions brought about by secondary electrons. Maximum beam penetration into the sample will occur when the beam is perpendicular to the target. Ideally, the detector would be placed at the same position as the collimator, but this is physically impossible. Therefore, the next preferred location for the detector is at  $135^\circ$  to the beam direction. Here the intensity of bremsstrahlung background is significantly less than it would be at  $90^\circ$  relative to the direction of the beam. [18]

### **2.3 XR-100 Fast Silicon Drift Diode Detector**

A Silicon Drift Diode is a type of photodiode that operates much like a Si-PIN photodiode. The difference is the SDD's special electrode arrangement. The electrodes induce an electric field that optimizes charge collection with a minimal input capacitance. A planar detector has a significantly higher capacitance than the SDD, and, therefore, suffers greatly from electronic noise at short shaping times. Electronic noise caused by short shaping times has a direct relationship with capacitance, so the SDD is capable of a better resolution, specifically for low energy x-ray spectra. This also applies to SDDs with large surface areas.

### 2.3.1 SDD Detector Theory and Operation

The prevalent noise in silicon x-ray Spectroscopy is pink noise. This noise increases with input capacitance and high frequency shaping times, but the low capacitance silicon drift detector offers lower noise at very fast shaping times. The Silicon Drift Detector has cylindrical symmetry. The design is like a planar, or Silicon-PIN, detector in that the SDD has a negatively biased ( $-50\text{ V}$ ) front implanted P+ cathode (region that intercepts incident x-rays), but what differs is the anode. The anode is just a small plate just microns in diameter; this offers a phenomenally low capacitance. With this very small anode much of the SDD would not be used, and the collection efficiency would be greatly reduced. This problem is overcome by placing several concentric annular drift electrodes around the anode. This increases the active volume of the diode, yet it continues to maintain an extremely low capacitance. Essentially, the rings ensure that the useful area of the detector diode is independent of the input capacitance.

The p+ implanted electrode rings are negatively biased with resistive dividers in between. The outer ring is held at  $-100\text{ V}$ , and the voltage progressively steps down by increments of  $10\text{ V}$  ending at the inner ring which is held at virtual ground. This creates an electric field that sweeps charge carriers radially toward the anode. Electrons drift for several microseconds and, for the total drift time, a current is induced within the diode. As the holes and electrons move from locations of higher to lower concentrations, a diffusion current occurs causing the charge cloud to grow. This increases the collection time for interactions occurring at the outer edge of the active volume of the drift diode which causes the risetime in the preamplifier to fluctuate. The preamplifier risetime

remains very fast though because the virtual ground electrode acts as a shield to the anode; only drift motion occurring after the final electrode will serve to deliver the signal current to the anode. Operationally, the SDD has the same resolution as a Si-pin detector but at 10 to 20 times higher peaking frequency. This allows for the processing of 10 to 20 times the count rate while maintaining quality data acquisition; statistics can be obtained very quickly.

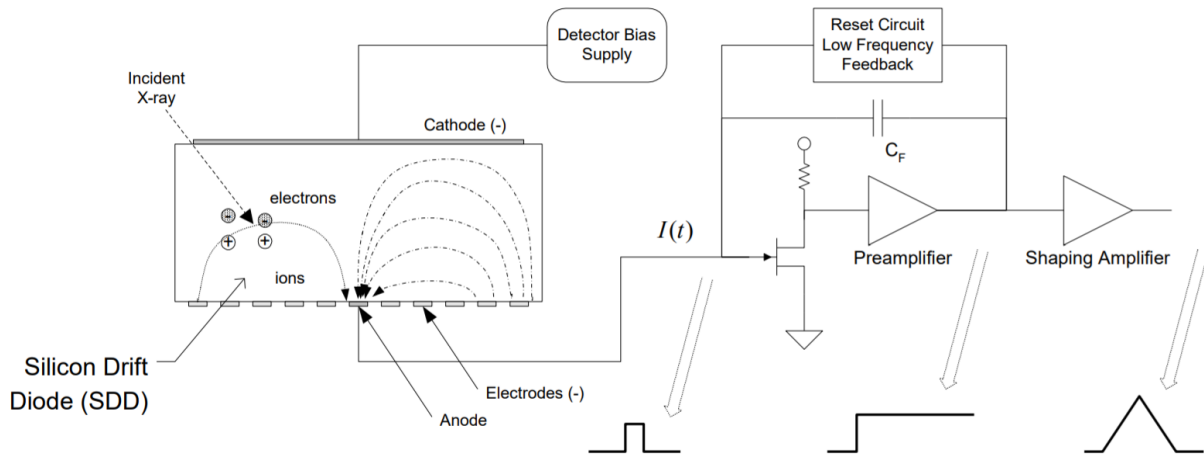


Figure (19). Illustration of the operation of a silicon drift diode (SDD). [32]

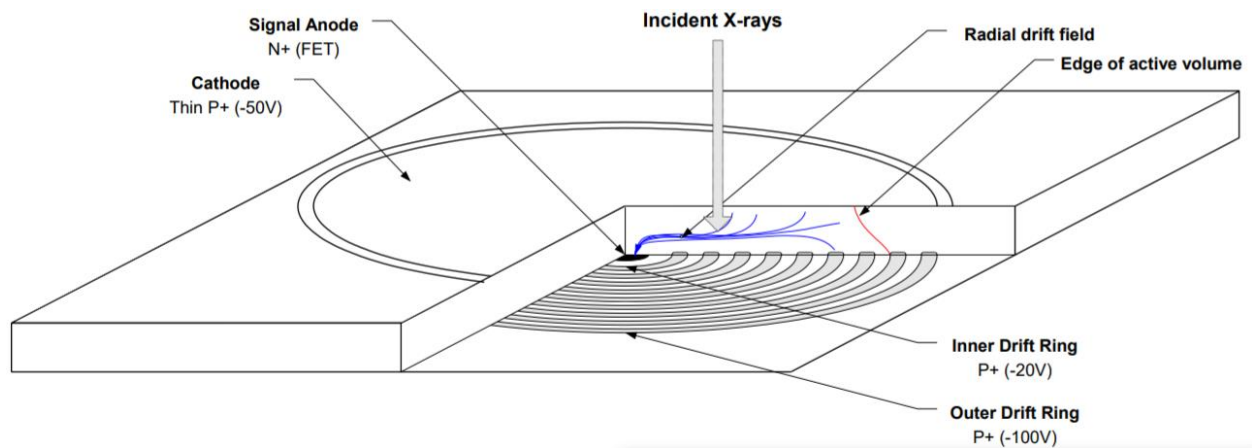


Figure (20). Illustration of the operation and construction of the XR-100 Fast Silicon Drift Diode. [32]

### 2.3.2 Temperature Control

The XR-100 FAST SDD's temperature is controlled by a closed-loop temperature control and does not require LN<sub>2</sub>. Temperatures between 210 and 230 K can be reached at maximum cooling. Decreasing detector temperature will increase energy resolution. An increase in the operating temperature of the detector causes an increase in leakage current; as a result, the data will have a degraded energy resolution. [33] The FAST SDD dissipates about 1 Watt during operation. To adapt the detector to the evacuated environment and lower the detector's operational temperature, which reduces noise from signal, a large portion of the detector's casing surface area was placed in contact with, and conducts heat to, an aluminum mount located inside the target chamber. The detector stabilizes after getting below 233 K, small temperature fluctuations below this point will not hinder detector performance.

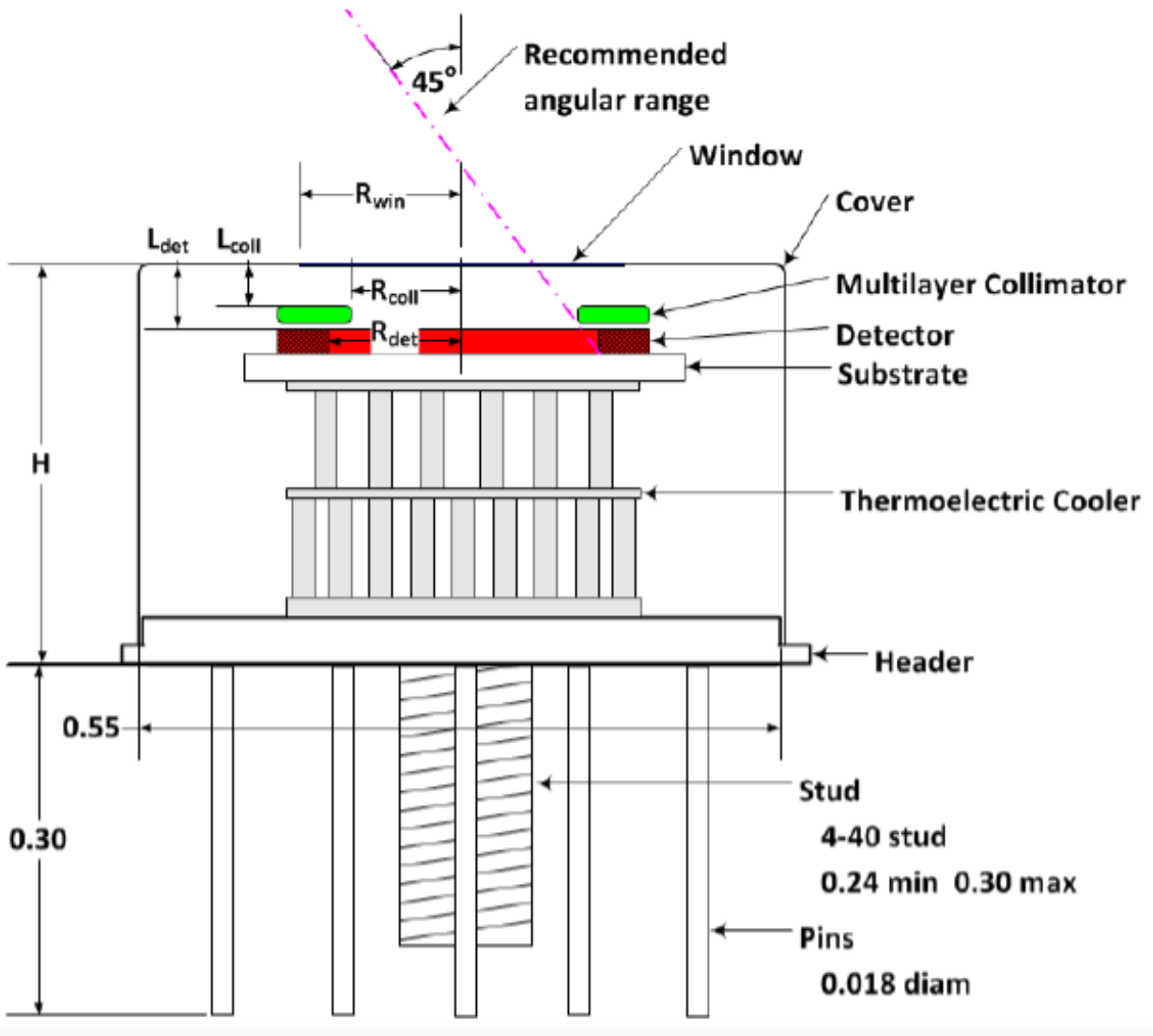


Figure (21). Diagram of the SDD detector core. [21]

### 2.3.3 Resolution

Good energy resolution is important for resolving peaks in the x-ray spectra. At short shaping times the SDD has a very low electronic noise. The area of the SDD does not contribute significantly to resolution; the SDD provides high resolution with a large surface area. Lower noise at a high-count rate gives way to better resolution, this is especially true at energies below 5 keV.

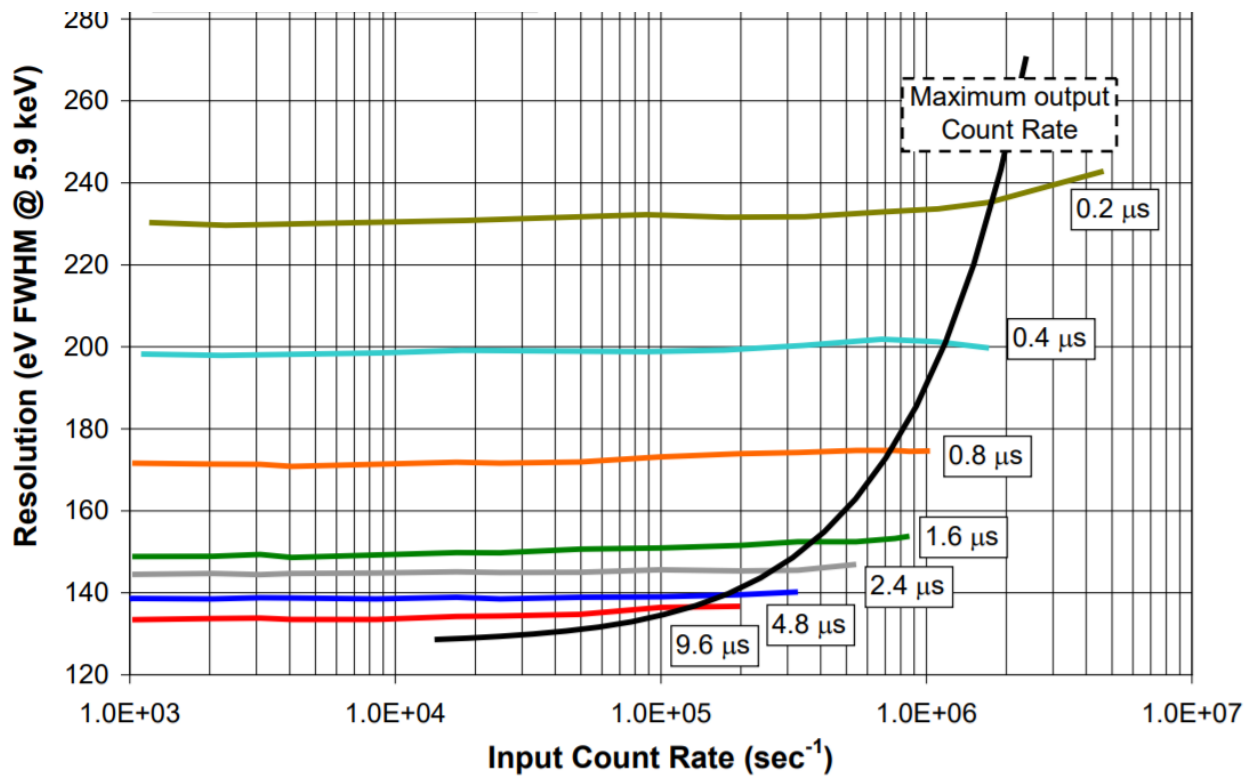


Figure (22). Full Width Half-Max resolution in eV vs. Input Count Rate Frequency for various pulse shaping times. [34]

At standardized settings, ECU's XR-100 FAST SDD was factory tested using an  $Fe^{55}$  radioactive source, which decays by electron capture by the nucleus, emitting a characteristic Mn K x-ray. With a 4  $\mu s$  peaking time the Mn 5.9 keV  $K_{\alpha}$  line had a resolution of 131.8 eV FWHM. Temperature, flat top width, and peaking time all affect the detector's energy resolution. If there is a high-count rate the peaking time can be shortened to provide narrow peaks. This will allow more events to be counted, but the spectra will be noisier. If the count rate is low, the peaking time can be increased, in turn, improving resolution (less noise), but venturing out of the noise corner will be costly to resolution. Short peaking times decrease dead time, offer high throughput, and deal well with high count rates, the tradeoff is the electronic noise associated with fast peaking times. Peaking times that are too long with respect to the incoming counts will cause pulse pile-up. A certain peaking time where electronic noise is at its least is called the "noise corner". As peaking times move away from the noise corner resolution becomes inferior in quality. Ideally, the detector should be operated at the peaking time that corresponds with the noise corner, or a little bit faster to resolve higher count rates. The proper peaking time depends largely on the exact detector and preamplifier.

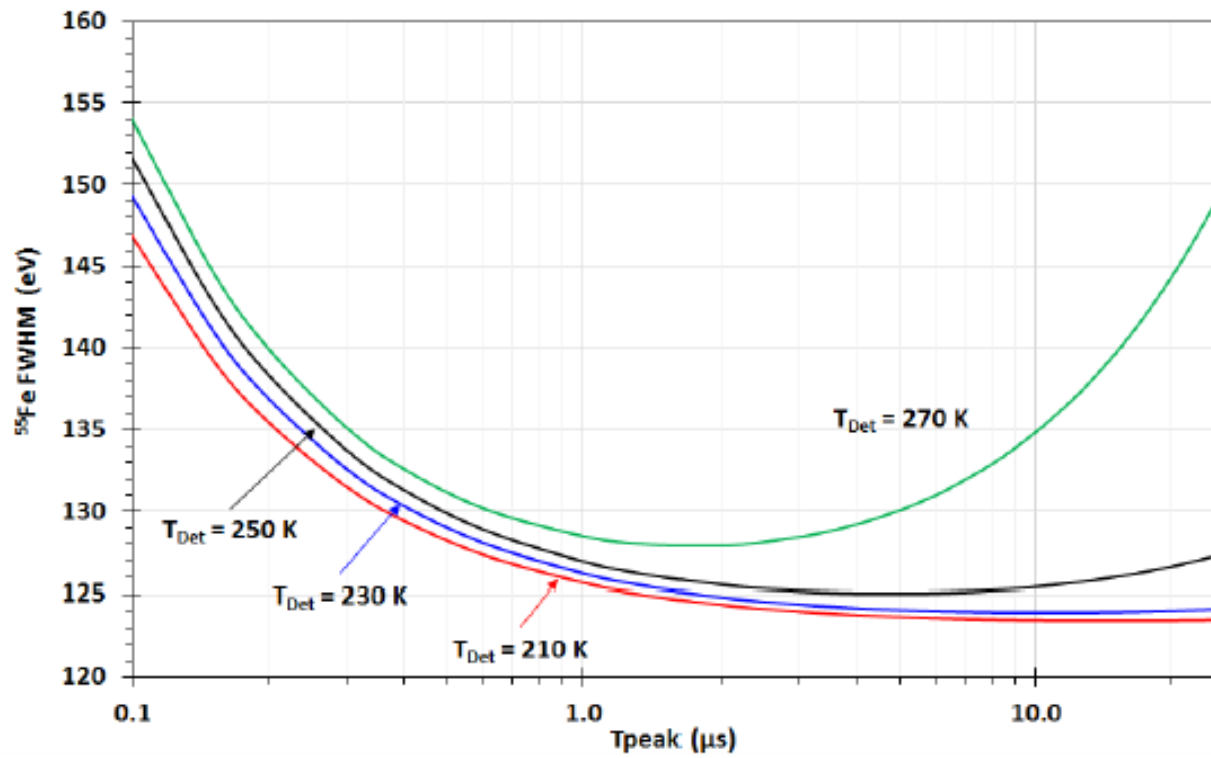


Figure (23). Iron-55 FWHM resolution vs. Peaking Time and Temperature of the XR-100 Fast SDD. [21]

### 2.3.4 Efficiency

Low energy x-ray detection is mostly limited by the depth of the 12.5  $\mu\text{m}$  beryllium window. At low energies, air molecules, the beryllium window, contact material at the front of the detector, and the dead layer can interact with the photons, so they will not be detected. The dead layer is a thin layer of oxide about 400  $\text{\AA}$  thick and a subsequent layer about 200  $\text{\AA}$  thick where the E-field is weak. This leaves a total dead layer of 600  $\text{\AA}$ , which is relatively shallow, and is not a major factor in x-ray attenuation. High energy x-ray detection is subjugated by the depth of the silicon detector. High energy x-rays pass through the detector without interacting if the active volume is not thick enough to attenuate them.

With a 0.5 mil (12.5  $\mu\text{s}$ ) beryllium window, about 90% of incident x-rays with energies between 2-3  $\text{keV}$  enter the detector. The efficiency starts to drop off at 10-12  $\text{keV}$  where an approximate 90% are detected. Efficiency drops off below 10% after 30  $\text{keV}$  where they are Compton scattered, or simply pass through the detector. To view spectra above 80  $\text{keV}$  it is probable that the data acquisition will take a very long time.

Regarding figure (23), the beryllium window makes up the first layer of the detector, while the second layer is made up by a dead layer, active volume of the detector comes next, then the final layer is comprised by the inactive volume of the detector. There are several scenarios that may transpire as an x-ray encounters the detector. Incoming x-rays may interact with the beryllium window, the contact material, or the dead layer, and will never reach the detector (blue arrows), which causes efficiency loss at low energies. The red arrow depicts a photon interacting with the

active volume of the detector which will cause an output signal. When this occurs, the x-ray energy may be entirely absorbed by the active volume and will be counted as a full energy peak. When an x-ray is attenuated by the active volume, the total energy of the event may be reduced if the x-ray scatters out of the active volume, or if the x-ray Compton scatters another particle out of the active volume. If the x-ray is not attenuated by the active volume (green arrows) the event is never counted, this causes a loss of efficiency at high energies. [35] Elemental analysis of light elements such as Na and Mg call for a very thin beryllium window with no other absorbers present. At 3 *MeV*, protons will backscatter into the detector; therefore, light-element analysis can be performed using protons with energies around 0.5 to 1 *MeV*. Backscattered ions will be absorbed by an 8-12  $\mu m$  thick beryllium window.

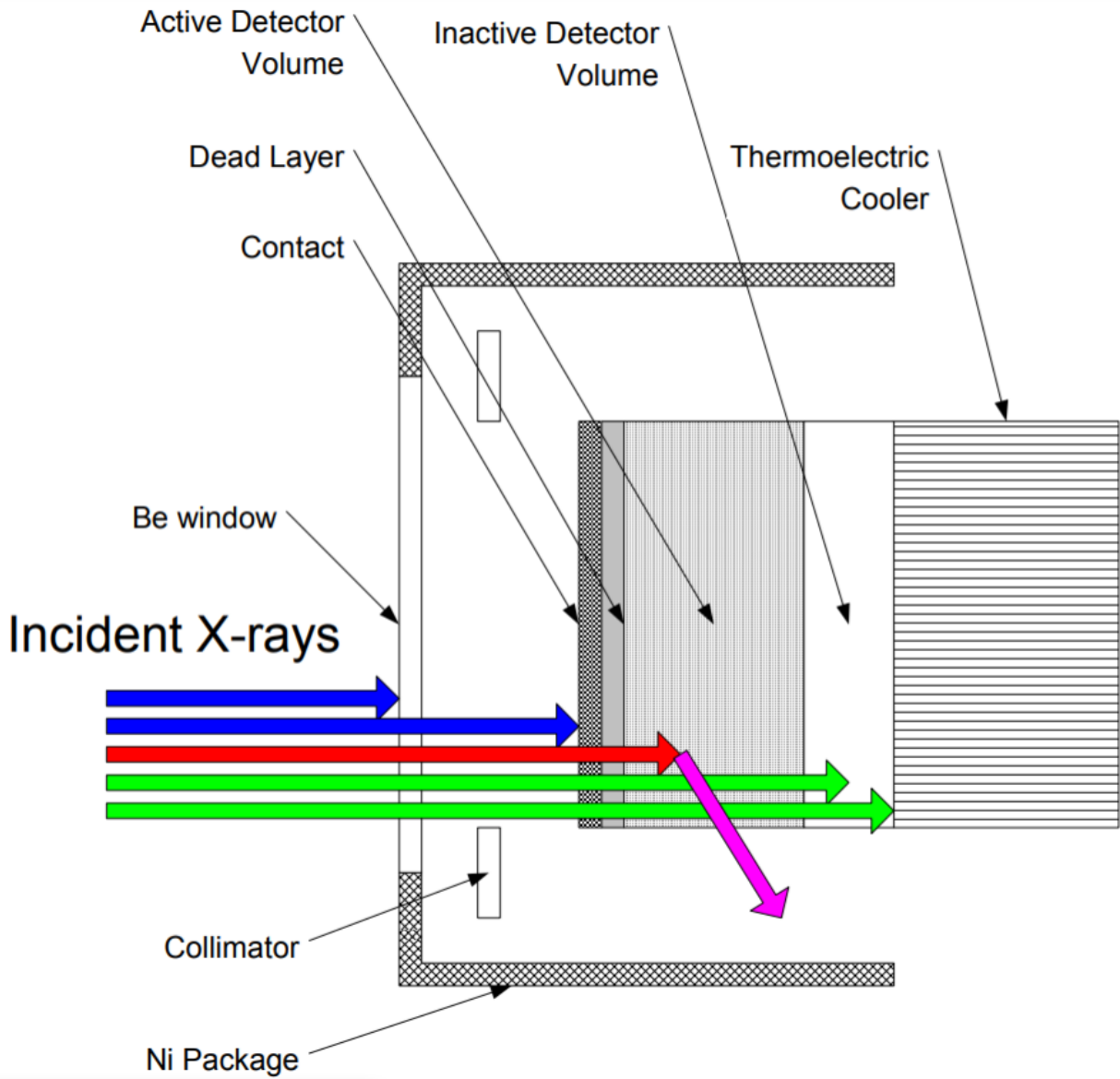


Figure (24). Schematic drawing of the detector illustrating the parameters that determine the efficiency. [35]

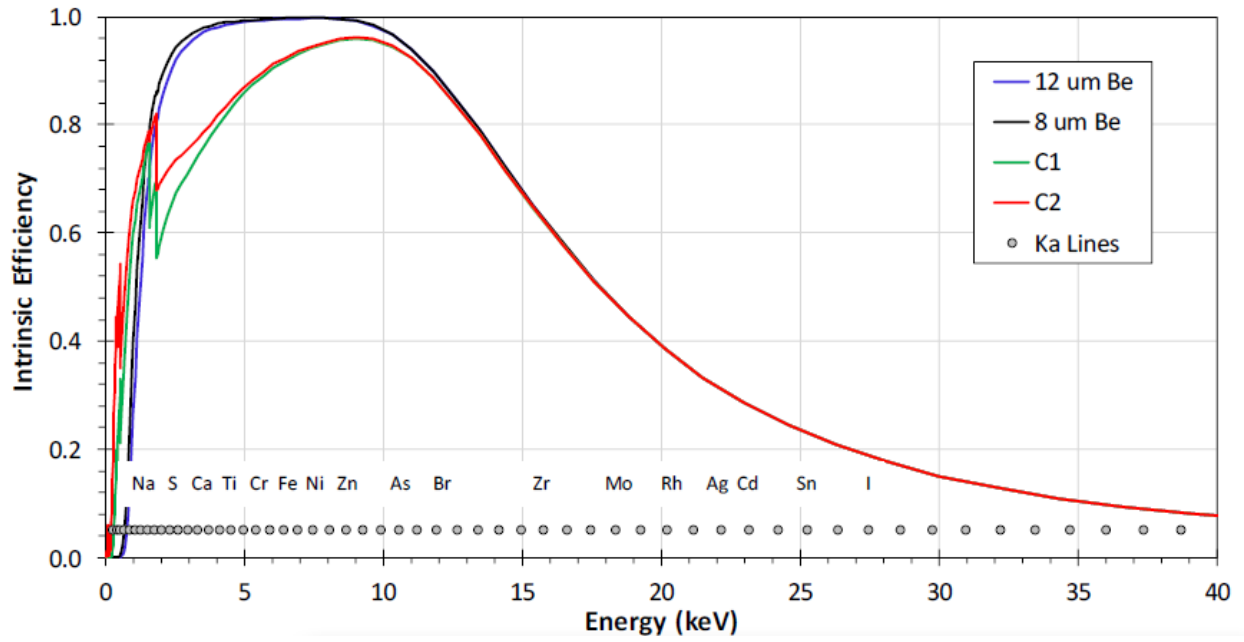


Figure (25). Efficiency vs. Energy Fast SDD (ECU detector: 12µm Be window).

[35]

### **2.3.5 Multi-Layer Collimator**

To reduce aberrations in the spectra, a 17  $mm^2$  multi-layer collimator is located behind the beryllium window of the XR-100 FAST SDD. The collimator shields edges of the SDD to limit, or completely stop, potential interactions from occurring outside the active volume. The collimator is layered in order of descending Z materials: tungsten, chromium, titanium, and aluminum. The fluorescence peaks of previous layers are absorbed by the succeeding layers. After passing through the lowest Z material the undesired x-rays are far below the detection limit. The same materials used for multi-layer collimation are also good materials for attenuation and collimation filters.

### **2.3.6 PX5 Digital Pulse Processor**

The PX5 offers superior resolution under higher count rates. The multichannel analyzer and shaping amplifier found in analog detection electronics are replaced by the PX5 digital pulse processor. The DPP digitizes preamplifier output, tracks peak amplitude, and bins data to send to the user interface. PX5 settings are all configured through the DPPMCA software.

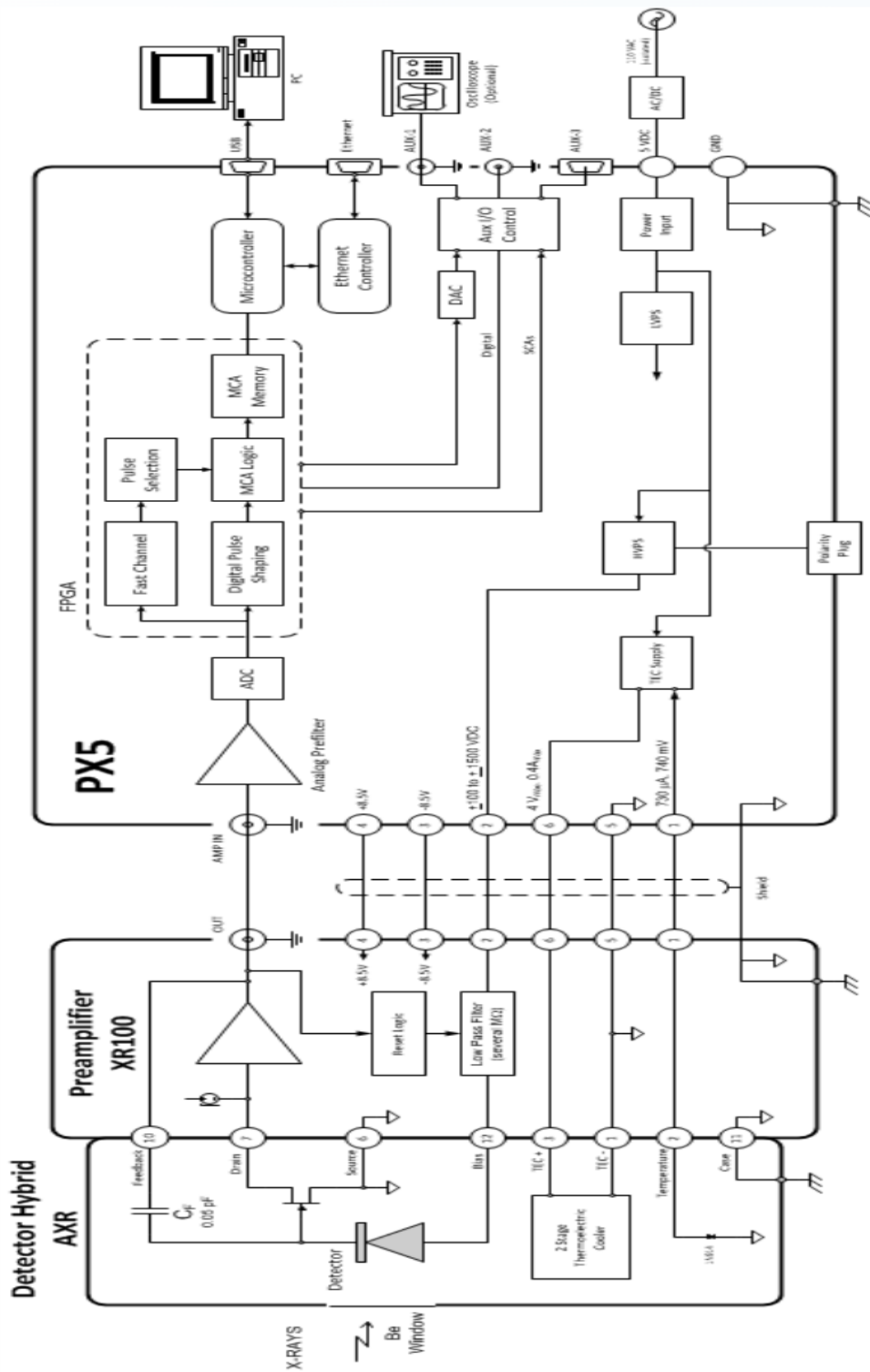


Figure (26). Block Diagram of the detector, the preamplifier and the digital pulse processor. [36]

### 2.3.7. Energy Calibration

Energy calibration is the most common task when readying the PX5 for data acquisition. Energy calibration is achieved by setting the gain with the DPPMCA software. Gain settings determine the full-scale energy range of the spectra. Even though most high energy x-rays will not be caught by the thin SDD, and it is rare to see them in the statistics, the gain should be set to include all possible x-ray peaks in the energy spectrum; failing to do so can negatively affect dead time. For high energy x-rays to appear in the spectra, longer run times are required, as the probability for attenuation inside the SDD increases with time.

The energy range can be determined by taking an initial spectrum of a known substance, assign certain peaks their known energies, then use the software to calibrate. This will determine the energy range and will provide information that can aid in making gain adjustments. After tuning the gain for the desired energy scale the thresholds should be adjusted – it is advisable to update thresholds any time a parameter is altered. The following is the gain energy per channel data taken with ECU's Fast SDD.

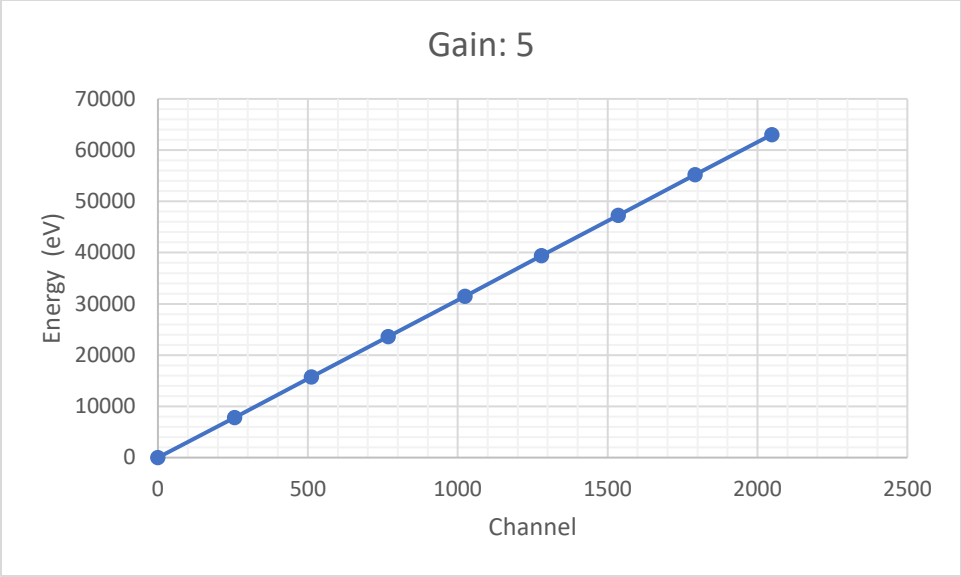


Figure (27). Gain = 5, Energy vs. Channel Number.

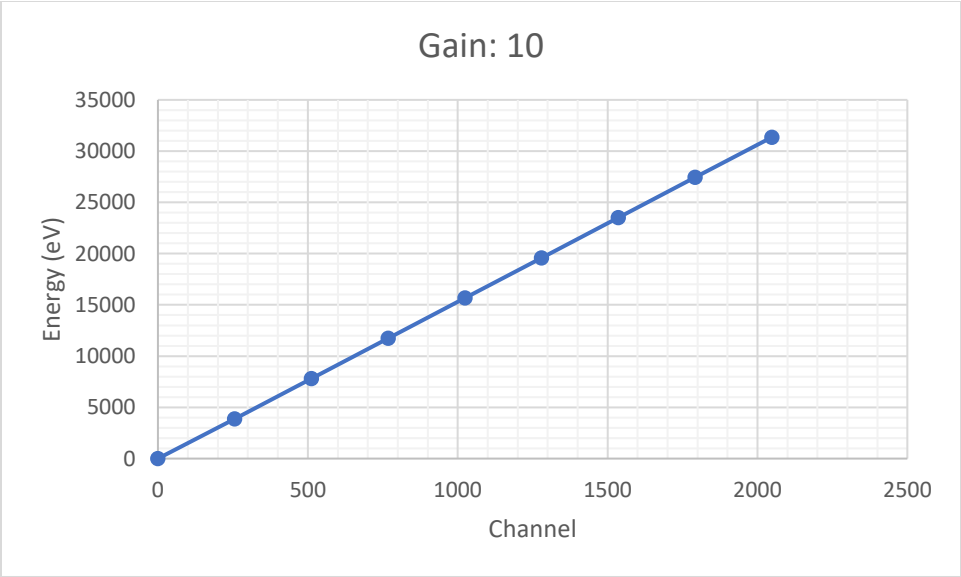


Figure (28). Gain = 10, Energy vs. Channel Number.

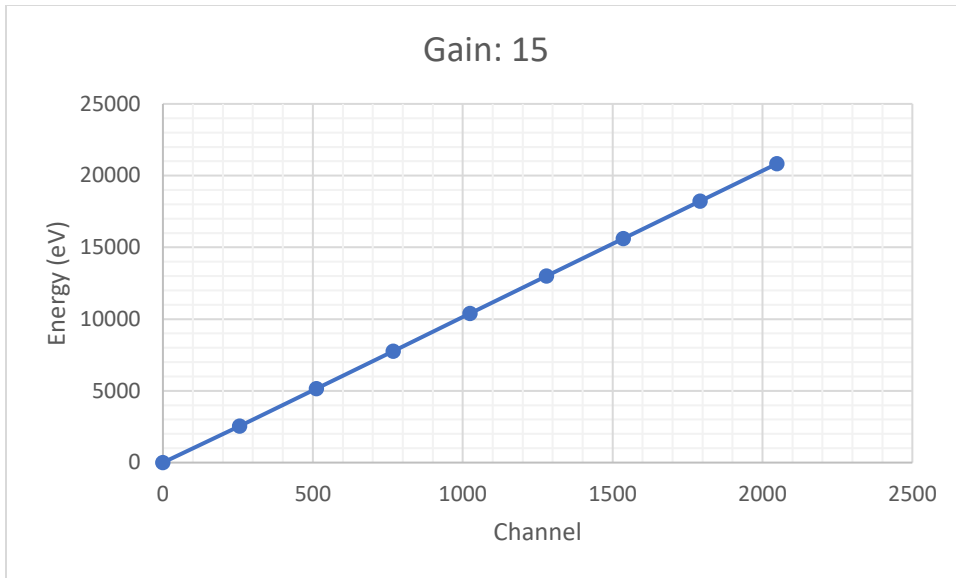


Figure (29). Gain = 15, Energy vs. Channel Number.

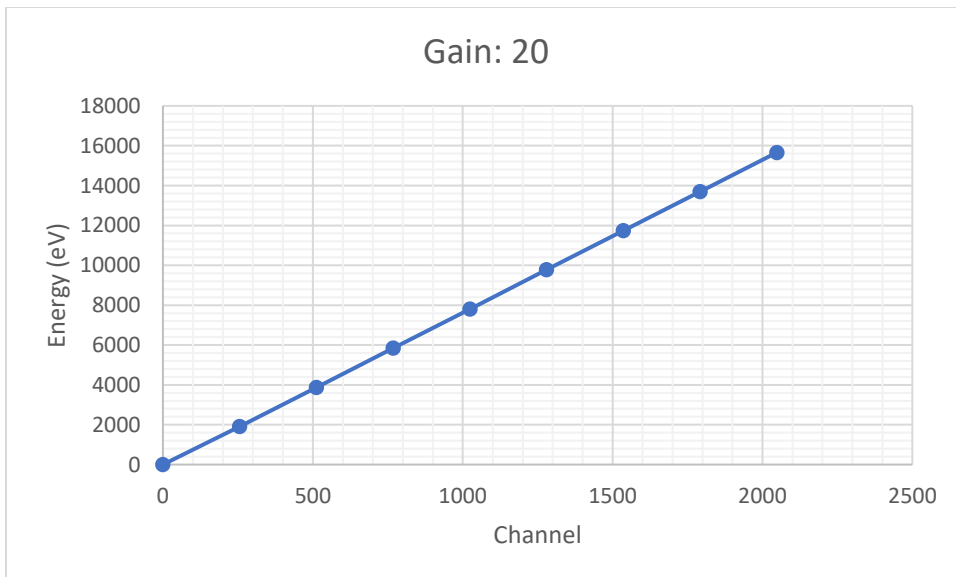


Figure (30). Gain = 20, Energy vs. Channel Number.

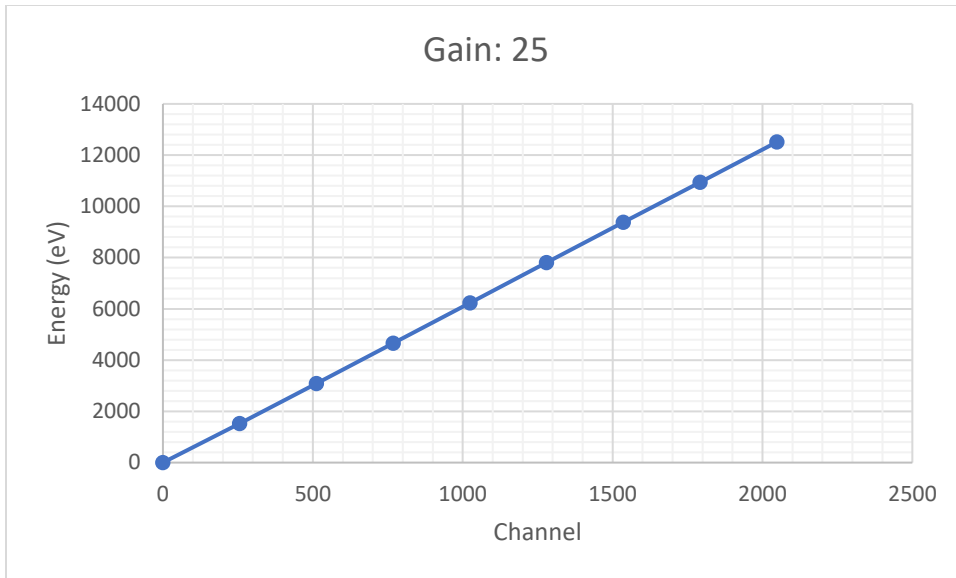


Figure (31). Gain = 25, Energy vs. Channel Number.

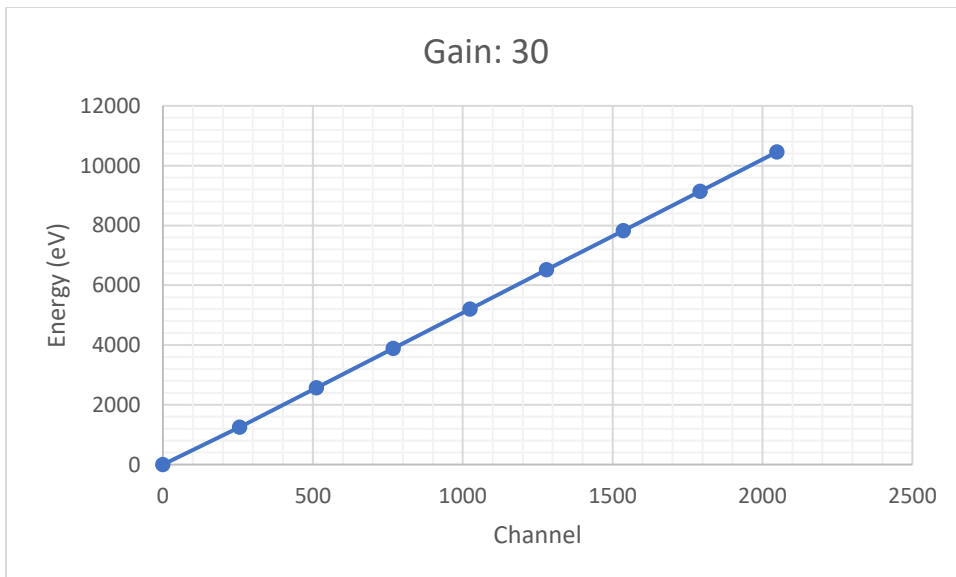


Figure (32). Gain = 30 Energy vs. Channel Number.

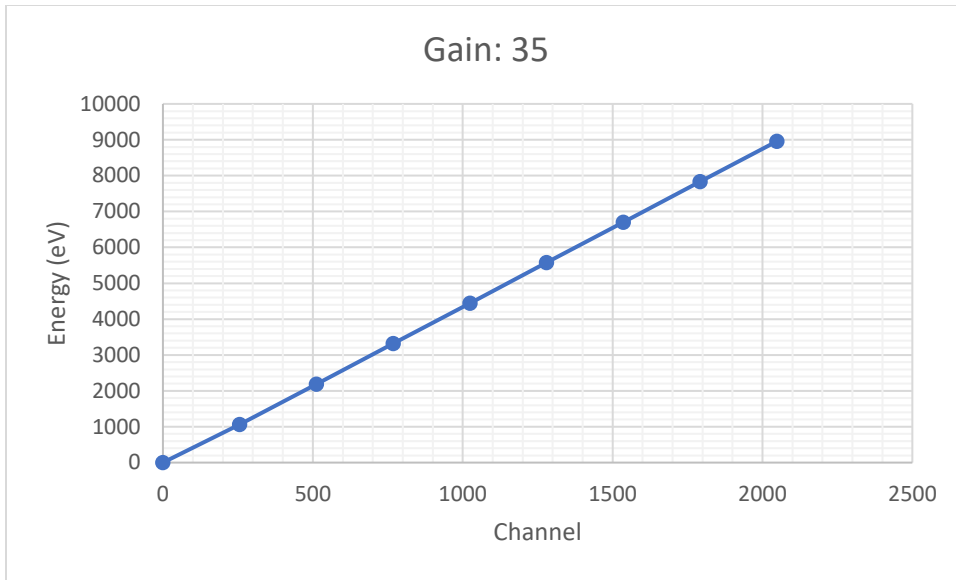


Figure (33). Gain = 35, Energy vs. Channel Number.

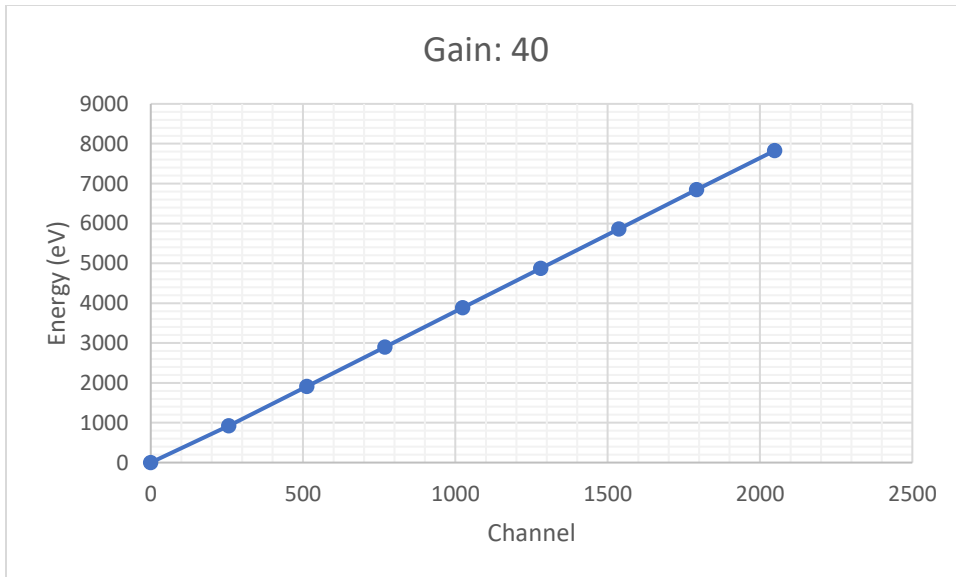


Figure (34). Gain = 40, Energy vs. Channel Number.

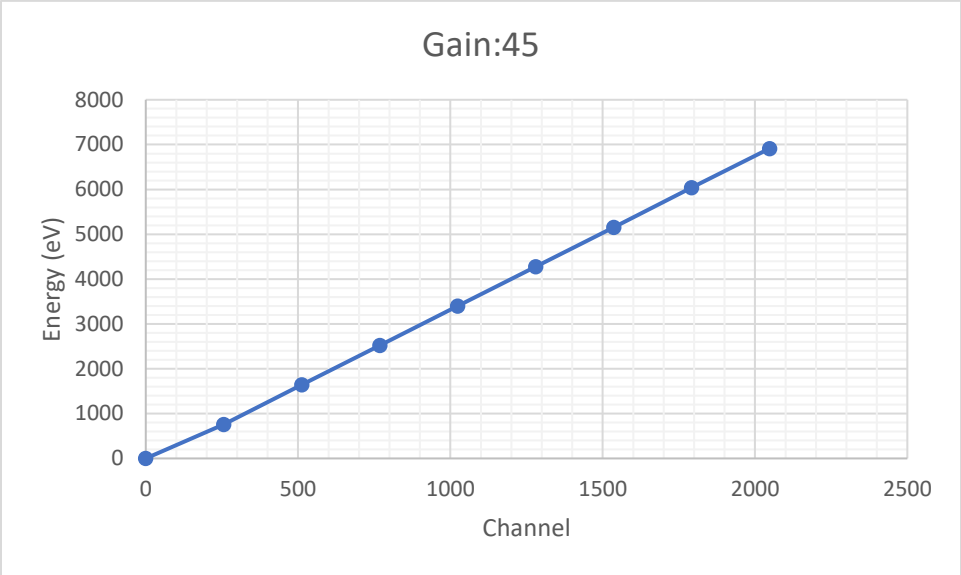


Figure (35). Gain = 45, Energy vs. Channel Number.

### 2.3.7.1 Pulse Shaping

The Digital Pulse Processor identifies pulses by using thresholds. The DPP has parallel signal processing paths known as “slow” and “fast” channels, they both gather inbound pulse train data. The independent thresholds can be set for both the slow and fast channels. Optimal performance for the DPP depends greatly on proper slow and fast threshold settings. Thresholds should be set just above the noise in each channel. The fast channel will encounter more noise, so both thresholds should be different. The DPPMCA software provides an “Auto Tune” function to automatically set slow and fast thresholds. Thresholds should only be tuned when no x-rays are being emitted by a source; only background should be “seen” by the detector when setting thresholds. Thresholds should be reset any time a setting in DPPMCA software is changed. [32]

The pulse shaper’s main output is the peak values for each pulse permitted by the slow channel threshold. The slow channel threshold is used to distinguish pulses that should be included in the spectrum. The Digital Pulse Processor’s slow channel, with its relatively long time constant, acts as a low-level discriminator. All the events that are recorded in the spectrum are totaled with the slow channel counter. The channel determines accurate pulse heights; pulses having amplitudes below the slow channel threshold do not appear in the spectrum. In contrast to analog shapers, the DPP’s slow channel relies on trapezoidal pulse shaping. Trapezoidal shaping reduces pulse pile-up and electronic noise.

If the peaking time is short compared to the slow channel risetime (too long for a full charge collection), the accuracy of outgoing pulses will be adversely affected by

ballistic deficit. Pulses can also be totally dismissed if the threshold is set to high on the slow channel. [36]

Like the slow channel, the fast channel uses trapezoidal shaping, but the peaking time is much faster – approximately 0.1 to 0.4  $\mu\text{s}$ . This means that the fast channel noise is typically higher. One of the fast channel's functions is to act as the "fast channel counter". The fast channel counter records and increments every incident where an x-ray exceeding the threshold is detected and increments the event in the input count. Another primary function of the fast channel is to activate pile-up rejection logic. Events in the slow channel that occur in a very short separation of time, or "pile-up", are indistinguishable by the slow channel. The fast channel identifies these peaks and serves to reject the pulses that pile-up. If pile-up rejection (PUR) logic is activated, and the threshold is set too low on the fast channel, every event will be rejected – no signal will appear.

The pile-up rejection and rise time discrimination logic serves to reject events that do not clear certain thresholds. If no pulses are being recorded, it is possible that the thresholds are improperly configured. The rise time discrimination circuit should always be disabled for the purposes of ECU's PIXE system, but the Pile-up Rejection circuit should be enabled *after* all other system configurations have been set. PUR logic should always be activated while taking data with the PIXE system. [36]

The purpose of PUR circuitry is to identify events that occur faster than the pulse pair resolving time. This means pulses that occur so closely together in time that they appear as a single pulse with an invalid amplitude. If the electronics fail to see pulses

separated by less than the peaking time as two discrete events, pile-up logic will trigger. The symmetric trapezoidal pulse causes the pile-up interval, and the dead time, to be considerably faster relative to analog systems. The DPP calculates dead time and pile up rejection time intervals by summing the risetime and flat-top duration of the shaped pulse. X-rays that pile-up are not placed in the total count. [36]

Dead Time refers to the time interval that a series of pulses cannot be detected, and, therefore, are not included in the output count data. A higher count rate leads to a greater amount of dead time. Random pulses inevitably occur during the period of dead time, so the input count rate is always higher than the output count rate. Unlike analog multi-channel analyzers, The DPP encounters no dead time during peak acquisition, in addition to a significantly diminished dead time per pulse. Real time and accumulated time are both based on dead time. For example, if the real time reads 60 seconds, but the accumulated time reads 50 seconds, this means that 10 seconds worth of pulses were not counted; this would equate to a dead time value of approximately 17%. For good spectral data the dead time should be maintained below 60%. [36]

### **2.3.7.2 PX5 Electronics**

The SDD's charge sensitive preamplifier has an output voltage signal that is proportional to the time integral of current – input charge. The output of the charge sensitive preamplifier provides input to the PX5. The PX5 input signal is prepared for digitization with the filtering and pulse shaping functions implemented by the prefilter. The prefilter uses a 3.2  $\mu\text{s}$  high pass filter to prevent pulse “ride up”, and it applies appropriate gain and DC offset to optimize the analog to digital converter resolution.

The output of the analog prefilter is digitized at 80 MHz by the 12-bit ADC, and then sent to the digital pulse shaper where the signal encounters the fast and slow parallel processing channels.

The multichannel analyzer (MCA) receives the digital input and detects the peak amplitude of the shaped pulses; If the pulse selection logic recognizes the pulse as legitimate the data is incremented in a memory location (channel) that corresponds with the peak amplitude. The MCA creates a histogram that contains the number events per channel (energy range). This is the energy spectra. The MCA accommodates 256-8192 channels. ECU's MCA is configured at 2048 channels.

### **2.3.8 Detector Specifications and Construction**

Amptek SDD detectors require negative HV (-135 V by default). The FAST SDD has a very high peak to background ratio – 26000/1. Set at a peaking time of 4  $\mu$ s the XR-100 FAST SDD housed in ECU's PIXE apparatus was benchmark tested with Fe – 55 to have a 131.8 eV full width half max (FWHM) resolution at the Mn 5.895 keV  $K_{\alpha}$  line.

The detector was manufactured with a 12.5  $\mu$ m beryllium window, behind it is a 25  $mm^2$  active Silicon Drift Detector diode that has a thickness of 500  $\mu$ m. A multilayer collimator that uses a base metal of 100  $\mu$ m of tungsten (W). The subsequent layers of collimators consist of 35  $\mu$ m of chromium (Cr), 15  $\mu$ m of titanium (Ti), and 75  $\mu$ m of aluminum (Al), that collimate the active diode area to 17  $mm^2$ . The FAST SDD is

sensitive to magnetic fields, but the detector is far away from significant magnetic fields while housed in the target chamber.

The XR-100 FAST SDD is fastened with two mounting holes onto an aluminum stand within the PIXE chamber. This not only allows for a correct positioning of the detector but securing the detector with the mounting holes increases the contact area of the FAST SDD, this creates a better heat sync for the detector while under vacuum. This allows the detector to run approximately 4-6 degrees cooler.

The PX5 is used to set the temperature control point of the 2-stage cooler. In calibration, it is suggested to set the cooler to maximum cooling, let it stabilize then set it two degrees above the minimum observed temperature, so no temperature variations occur during data acquisition.

The PX5 includes a digital pulse shaping amplifier and multichannel analyzer. It can sustain high count rates while maintaining outstanding baseline stability, throughput, and pile-up rejection. Peaking times can be selected from 0.05 to 102  $\mu m$ . The multichannel analyzer can accommodate 256 to 8192 channels at 3 bytes, or 16.7  $M$  counts, per channel. Acquisition time is adjustable from 10  $ms$  to 466 days. The unit can be preset to measure time, total counts, counts in a region of interest (ROI), or counts in a channel. The PX5 uses a Silicon Labs 8051F340 8051 microprocessor with 512 kb SRAM external memory, the unit is controlled by Amptek DPPMCA display and acquisition software. This software fully configures, controls, downloads, and displays spectral data.

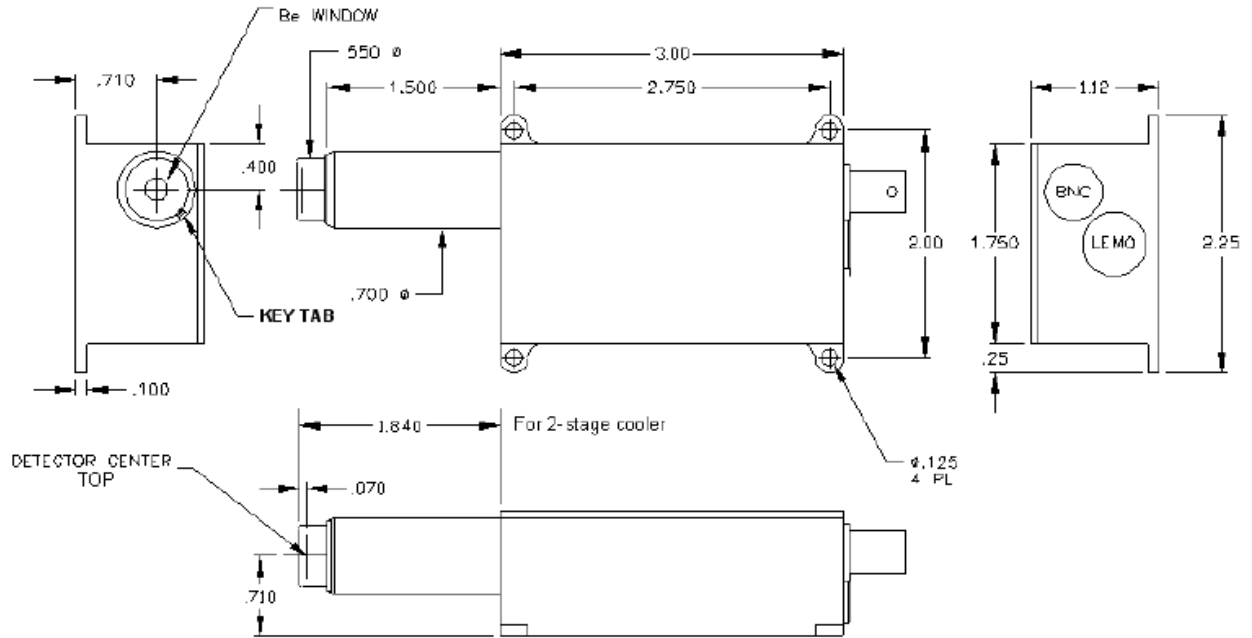


Figure (36). Fast SDD Dimensions (units in inches). [33]



Figure (37). Photograph of the XR-100 Fast SDD detector. [21]

### **2.3.9 Data Display and Analysis**

The spectrum, counts, and accumulation time are automatically displayed as data are acquired. If a region of interest is defined and selected, its net area and other properties are also shown. To zoom in on a portion of the spectrum, use the arrows at lower right. To return to the full screen view, use the full range arrows on the toolbar.

To toggle between a linear and logarithmic vertical scale click on the spectrum and press “L” on the keyboard or select the scale from the Display menu. The primary data from the SDD are the spectrum and the count rates. To toggle between channel number and energy press F7.

A region of interest, or ROI, is an area marked as a potential peak in a spectrum. To select a ROI. Place the cursor at the left edge (lowest channel) of desired region and then press and hold the “U” key until the peak is highlighted and the upper edge is reached. You can also select the right side of the peak and select to the left by pressing the “Y” key.

For each ROI, DPPMCA computes the total counts (gross area), subtracts the background, and with the difference computes the net area, centroid, peak width, and FWHM resolution.

### **2.3.10 Electrical and Software Interfaces**

There are three main elements to the electrical interface: communications, power, and auxiliary. The communications interfaces are the primary means to control

the PX5 and to acquire the data. The PX5 supports a USB interface. With all three interfaces, commands are issued to set the many configuration parameters. The unit sends three classes of data packets back to the computer: status packets (which include the counter outputs), Spectral data packets (which contain the MCA output array), and oscilloscope packets.

DPPMCA software provides the quickest way to control and readout the PX5. It provides access to all the configuration parameters in the DPP, lets one start and stop data acquisition, reads and displays the data, performs very simple analysis, and saves the data in an ASCII format. The files saved by DPPMCA can be read by many spectral processing software packages including GUPIX.

### **2.3.11 System Gain**

The system gain is used to assign channel numbers certain energy designations. The gain is stated in units of *channels/keV*, and it gives the MCA channel number a designation for certain energy peaks. The gain consists of the product of the conversion gain of the MCA (*channels/mV*), the total gain of the voltage amplifier, and the conversion gain of charge sensitive preamplifier (*mV/keV*). The preamp conversion gain is approximately  $1 \text{ mV/keV}$ , while the MCA's conversion gain is the number of channels (say, 2048) divided by the corresponding peak channel voltage ( $\sim 950 \text{ mV}$ ), while the digital pulse processor gain is the product of the coarse and fine gains. However, these values are simply estimates and the actual gain can fluctuate by a few percent. These approximations are good for find a starting point for initial calibration, but every detector will have a different energy scale per gain as they are dominated by the engineering

tolerances of the individual electrical components found within the system. Therefore, every detector should be calibrated by the operator. [21]

<b>Gain</b>	<b>eV/channel</b>	<b>Full Scale Energy (eV)</b>
5	30.77944336	63036.3
7.5	20.39575195	41770.5
10	15.31064453	31356.2
15	10.16967773	20827.5
20	7.646972656	15661
25	6.108642578	12510.5
30	5.10546875	10456
35	4.3734375	8956.8
40	3.821972656	7827.4
45	3.375952148	6913.95
46.5	3.266918945	6690.65

Table (5). Gain adjusted parameters.

### 2.3.12 Standard Operating Procedure

The following section highlights methods used for gathering spectral data with ECU's PIXE system.

PIXE samples are prepared and mounted inside the 24-position sample carousel. One space is left open, so accurate current readings may be taken by the Faraday cup located at the back of the target chamber. A blank position in the filter wheel allows for unattenuated x-ray collection. After the steel retaining rings for both the sample and filter wheels are replaced, they are mounted inside the chamber.

The chamber pressure is optimal for PIXE analysis at  $10^{-6}$  Torr ( $10^{-3} - 10^{-4}$  Pa), so the seal associated with the chamber lid is thoroughly cleaned. The track running around the top of the chamber is cleaned with alcohol to rid rough spots left from vacuum grease and particulates that may allow air to pass through into the evacuated chamber. The O-ring for the lid is cleaned with alcohol then lightly lubricated with high vacuum grease. After the O-ring is laid in the track, the lid is cleaned with alcohol and placed on top of the chamber.

The pressure valve on the side of the chamber is closed, and the collimator and fore-line valves are opened, the roughing pump is activated. Pumping the chamber down to  $10^{-3}$  Torr takes  $\sim 10$  min. The turbomolecular pump is turned on after the chamber is down to rough vacuum. After the chamber is at the desired vacuum, beam is placed in the Faraday cup at the back of the PIXE chamber.

The CCD Camera is used by the commercially available "EZ Grabber software" and is useful when controlling motors and lining up samples. To initiate the Lab View

motor control software the following steps are taken in sequence: the USB X-Series Multifunction DAC is turned on, the motor control module is turned on, then the Lab View software is opened. The motors will not operate if initiated out of sequence. Once control of the motors is established, the filter and sample wheels are adjusted to their blank positions. After opening the gate valve to PIXE line (L-45). Ion beam can enter the Faraday cup in the back of the chamber. After adjusting source and accelerator parameters for the desired experimental current, the PX5 Digital Pulse Processor is turned on.

If the PX5 power button is pressed quickly, a single chirp will be heard, and the detection parameters will go to the factory default settings. If the power button is held in, a multiple chirp will be heard, and the PX5 will be adjusted to the settings of its last use. The DPPMCA software is opened and connected to the PX5 Digital Pulse Processor. If the software is opened before the PX5 is turned on, there will be no connection established with the PX5 or XR-100 Fast SDD detector.

Acquisition parameters are chosen with the MCA tab or the acquisition setup button. This is where acquisition time, preset count, and number of channels can be set. The PX5 can be set to stop acquisition after a fixed time, after a fixed number of counts are collected, or both. It is recommended to keep the channels set to 2048 or 1024, as GUPIX can only accommodate 2048 channels. Under the shaping tab, peaking time can be adjusted (the noise corner for ECU's detector is  $4.0 \mu\text{s}$ ). Pile-up Rejection (PUR) should be turned off until all adjustments are made. The baseline reduction (BLR) mode is set at 1, with 3 down and 1 up, or with 3 down 0 up (the latter is factory

recommended). Clock speed is set to 80 *MHz*. The desired gain and cooler temperature (~210 *K*) is adjusted along with the high voltage bias (-135 *V*).

To start background adjustments, data acquisition (“traffic-light” button) begins with the beam only striking the Faraday cup. If there is an x-ray source it is removed. After a few seconds the “tune slow/fast thresholds” button is clicked, and the system is ready for data acquisition. After power is applied, or after a configuration change, it can take minutes for an Amptek detector to stabilize.

You can tell that data are being acquired if (a) the spectrum appears in the window, (b) the input and total counts are increasing (c) the accumulation time is increasing, and (d) the “status” in the right-hand info panel reads “acquiring.”

### **2.3.12.1 Energy/Channel Calibration**

After data acquisition of a known material, the cursor is placed to the leftmost edge of a known peak and the ROI is marked. An ROI is made with another known energy peak, and a third if applicable. The “calibrate” button is selected, and the cursor is placed on the first energy peak. The “centroid” button in the calibration dialogue box is selected and the centroid number appears in the channel box. A known energy associated with the peak is entered in the value box to the right of the channel box then added to the list of ROIs. This process is repeated with at least one other peak, for a minimum of two ROIs. Click “Ok”. The gain specific energy range is calibrated, and the system is ready for materials analysis

### 3. Results

#### 3.1 Target Chamber Results

The target chamber is made of materials that interfere very little, if at all, with the PIXE analysis process. It is also constructed to withstand high pressure differentials. The chamber typically reaches a vacuum of magnitude of  $10^{-6}$  Torr within 12 hours of beginning evacuation with the turbomolecular pump. Successful PIXE analysis can be performed at this pressure. A magnitude of  $10^{-7}$  Torr is usually reached within six days. Failure to reach the above pressures in these times, may indicate an air leak in the chamber.

The sample and filter wheels are operationally functional. The sample wheel moves in both directions of rotation like the sample wheel, and the translational motion of the sample wheel allows for the beam to be placed anywhere on a given target position on the sample wheel. All the motors housed within the chamber are successfully operational with the use of the customized Lab View PIXE motor control software. Additionally, the pneumatic valves that control the faraday cup and fore-line valve are both operational,

The drift lines and chamber are in very good alignment, and proton beam with currents as high as 160 nA have been measured with the Faraday cup located in the back of the PIXE chamber. Successful PIXE analysis only requires 1 nA of beam current.

Accurate materials analysis has been performed with East Carolina University's Particle Induced X-Ray Emission system.

### 3.2 Fe-55 data

For initial energy calibration, a  $Fe - 55$  x-ray source was used to generate control data.

The x-ray energies produced from known  $Mn_{K\alpha 1}$  (5.985 keV),  $Mn_{K\alpha 1}$  (6.49 keV) transitions the energy spectrum was calibrated with the visible manganese. The gain was set to allow for a larger energy range, and the  $Fe - 55$  energy calibration was verified with a  $Cs - 137$  source that emitted (31.81 Ba  $K\alpha 2$  and 36.38 Ba  $K\beta 1$ ).

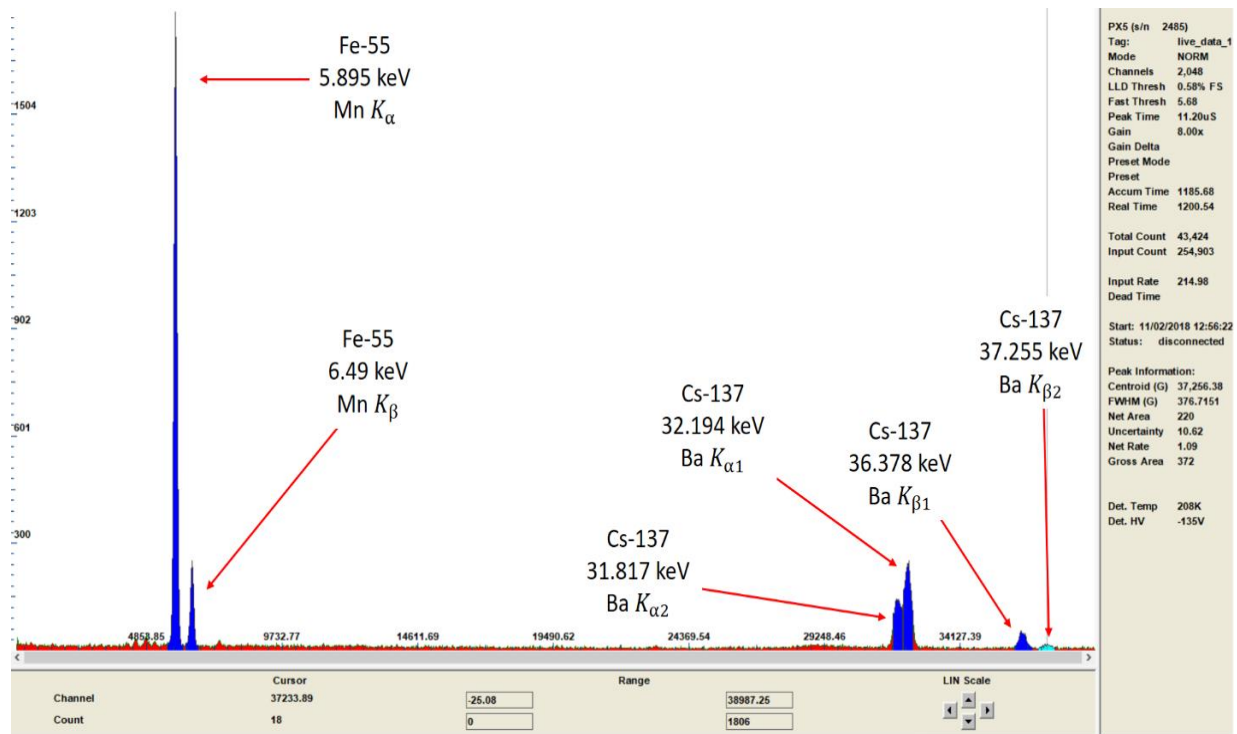


Figure (38). *Fe* – 55 and *Cs* – 137 Energy Calibration Data.

Gain settings change the spectral energy scale. Using  $Fe - 55$ , the full-scale energy range was compared to gain settings. Although it is not probable that a high energy x-ray will be completely attenuated in the Silicon diode, it has been suggested to set the energy scale to accommodate those energies; neglecting to do so may increase dead time.

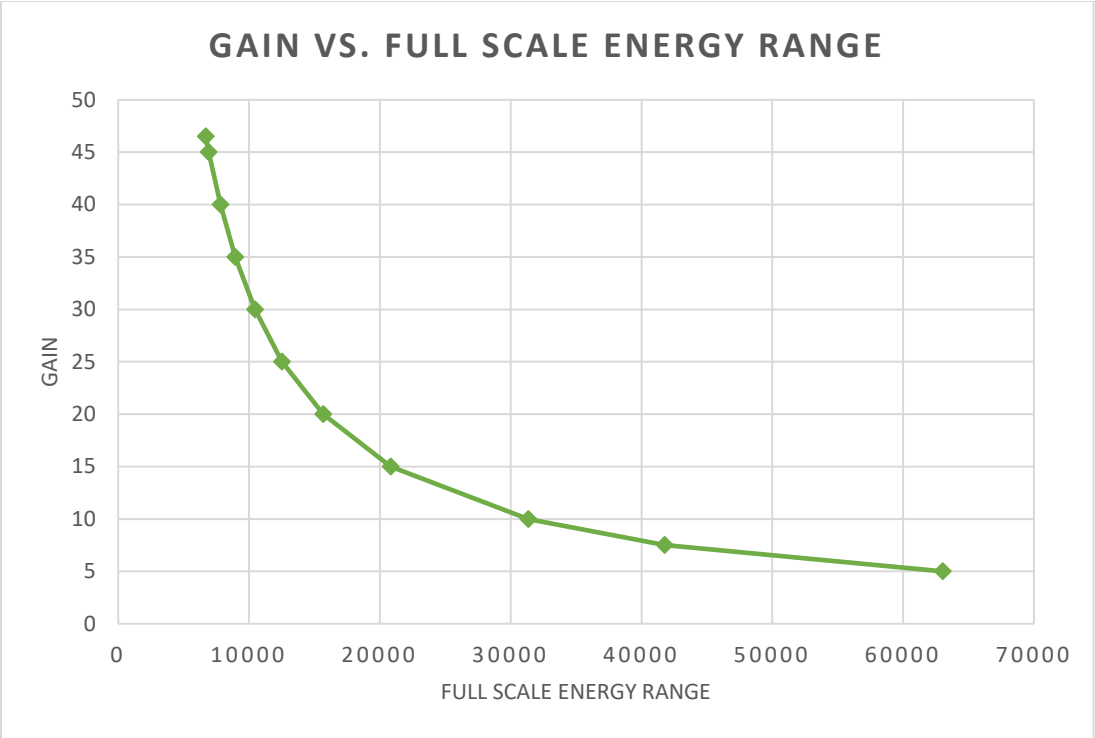


Figure (39). Gain vs. Full Scale energy range.

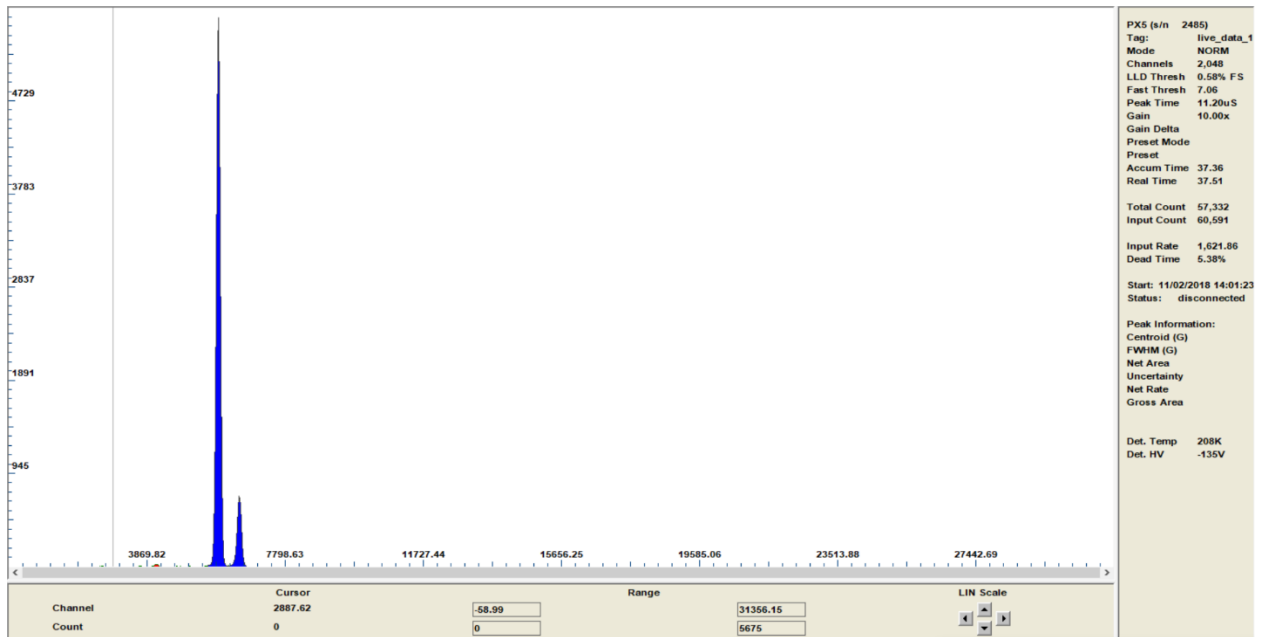


Figure (40).  $Fe - 55$ , Gain 5 (top). Figure (41).  $Fe - 55$ , Gain 10 (bottom).

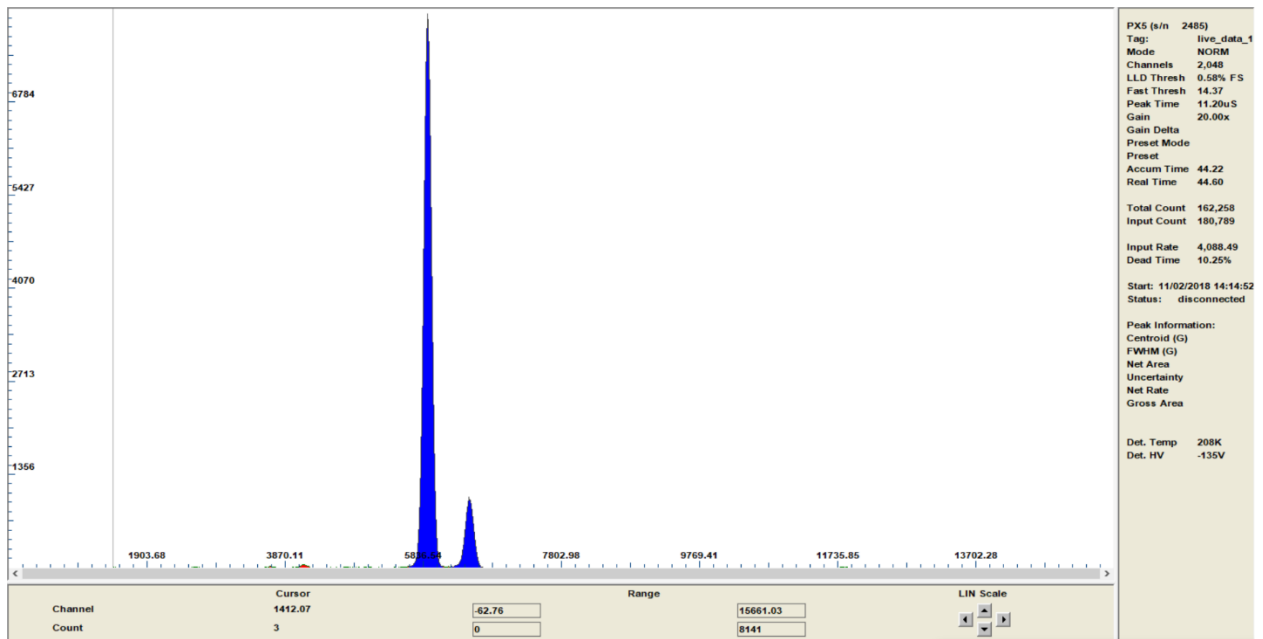
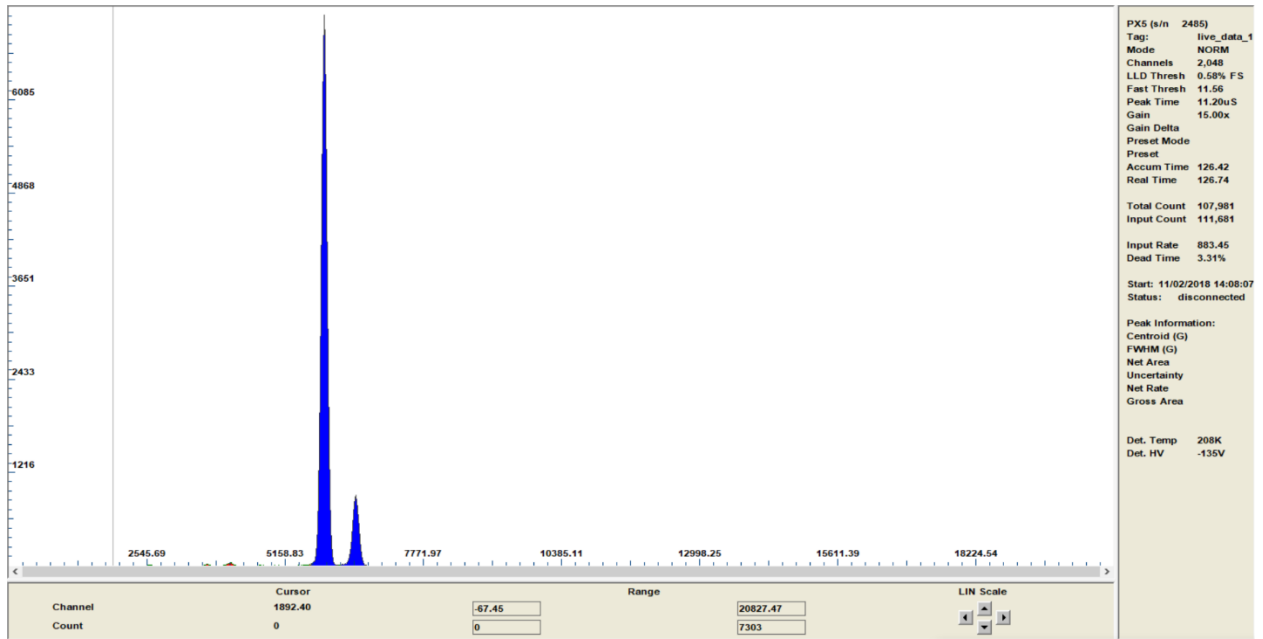


Figure (42).  $Fe - 55$ , Gain 15 (top). Figure (43).  $Fe - 55$ , Gain 20 (bottom).

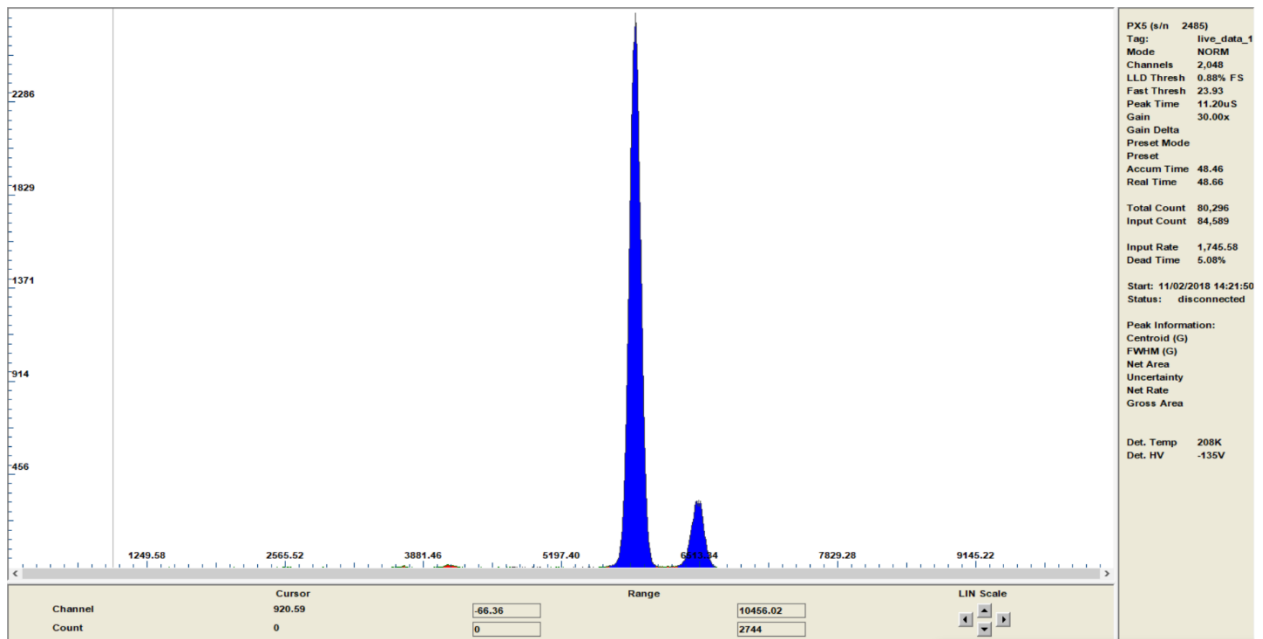
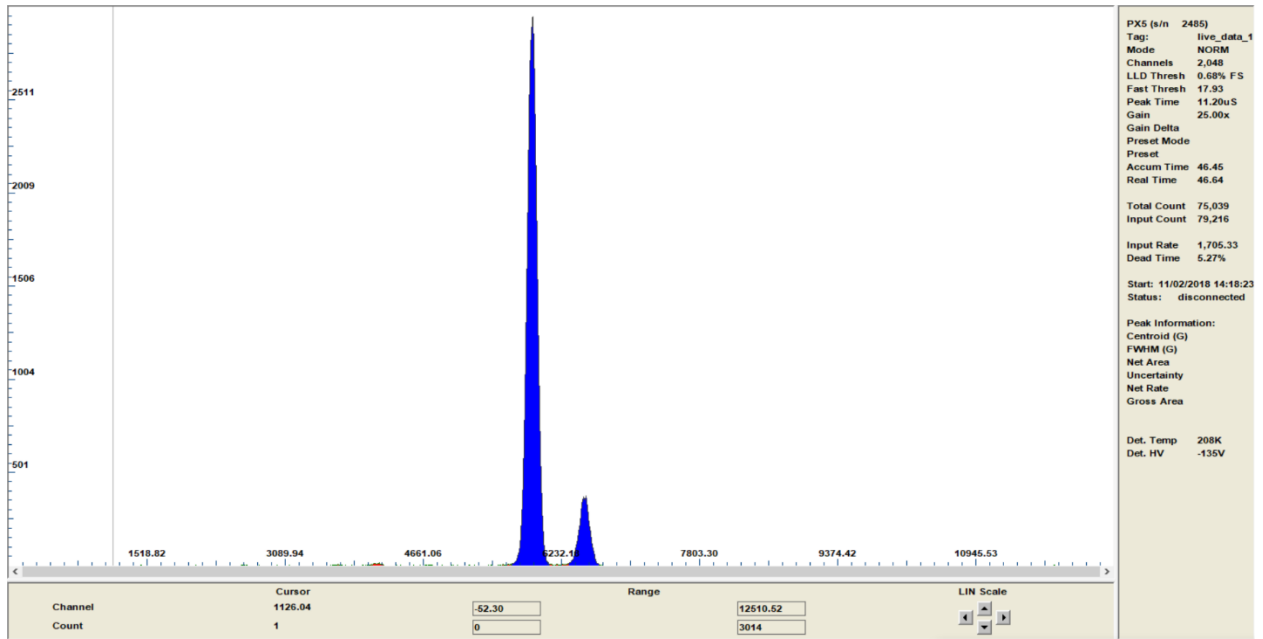


Figure (44).  $Fe - 55$ , Gain 25 (top). Figure (45).  $Fe - 55$ , Gain 30 (bottom).

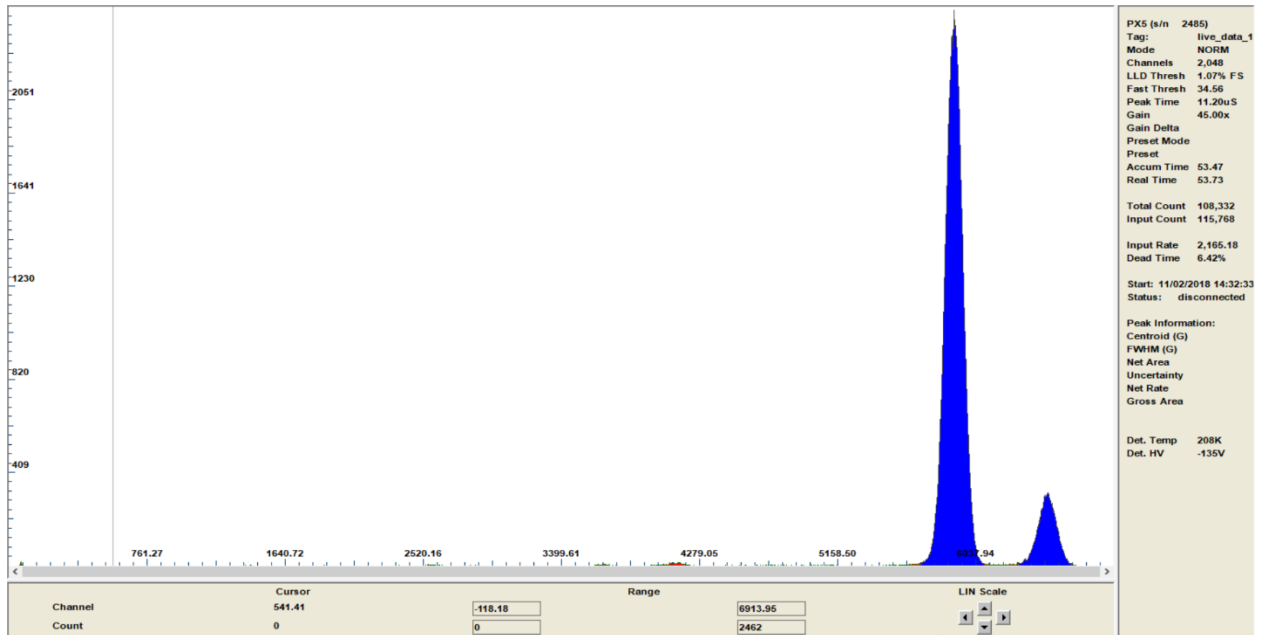
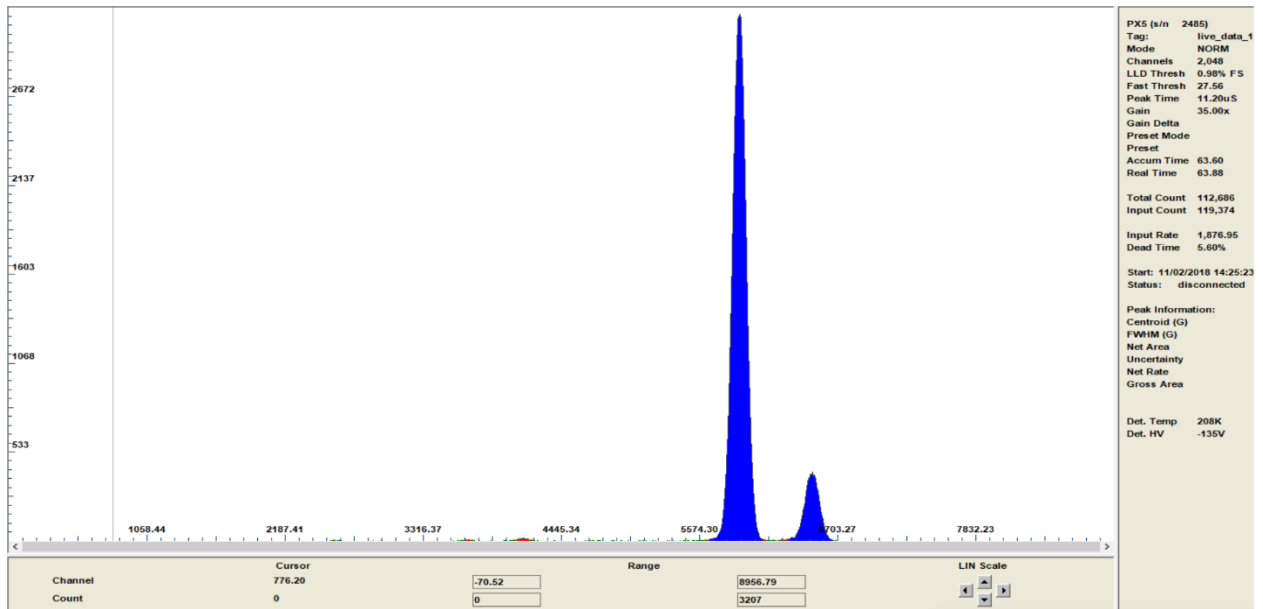


Figure (46).  $Fe - 55$ , Gain 35 (top). Figure (47).  $Fe - 55$ , Gain 45 (bottom).

<b>Gain</b>	<b>eV/channel</b>	<b>Full Scale Energy (eV)</b>
5	30.77944336	63036.3
7.5	20.39575195	41770.5
10	15.31064453	31356.2
15	10.16967773	20827.5
20	7.646972656	15661
25	6.108642578	12510.5
30	5.10546875	10456
35	4.3734375	8956.8
40	3.821972656	7827.4
45	3.375952148	6913.95
46.5	3.266918945	6690.65

Table (6). Gain – *eV/channel*.

An increase in peaking time causes an increase in parallel noise, but a decrease in series noise. Pink, or  $1/f$ , noise is independent of peaking time. This means that there is a time where noise is at its least – the noise corner. The data was taken with peaking times ranging from 1 – 25.6  $\mu\text{s}$ , and it showed that the least amount of noise was found at 4  $\mu\text{s}$  when taking  $Fe - 55$  data.

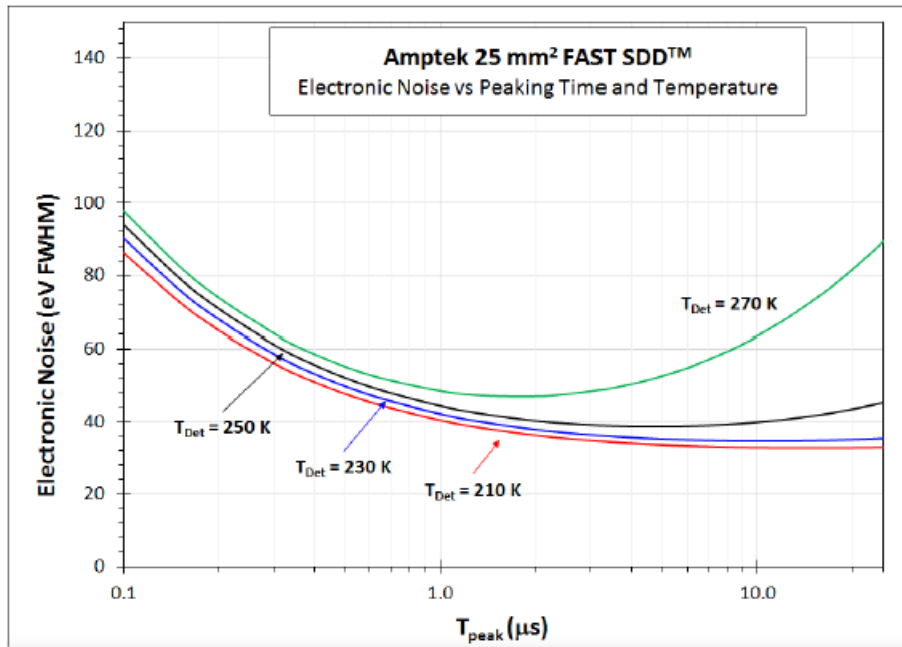
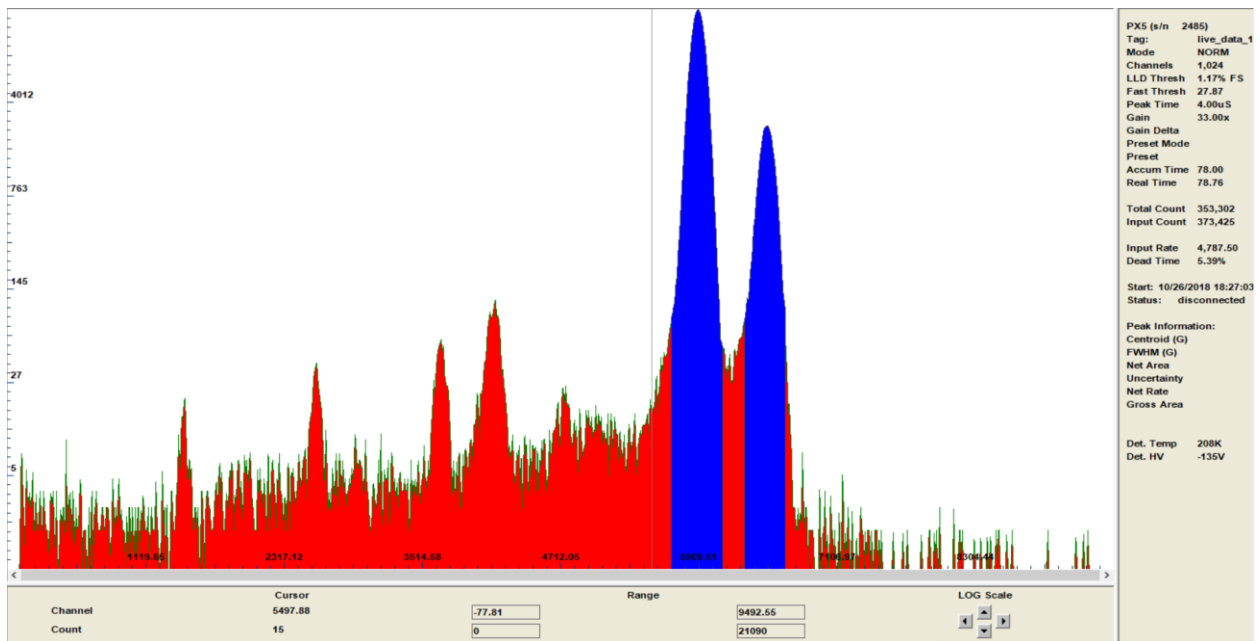
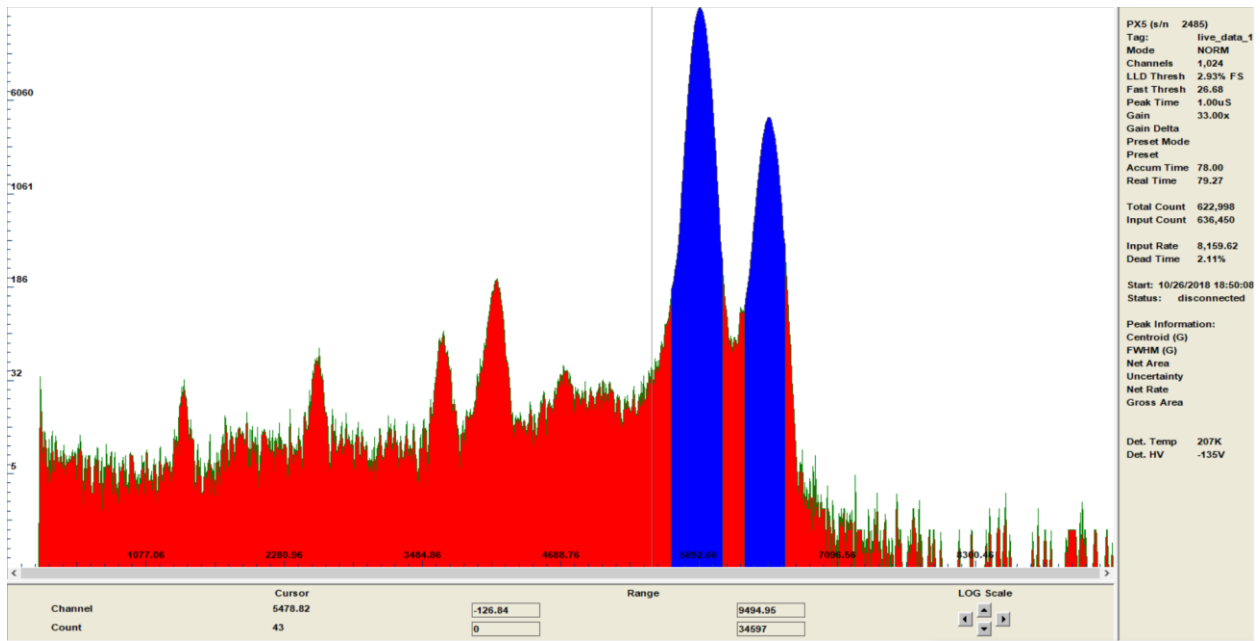
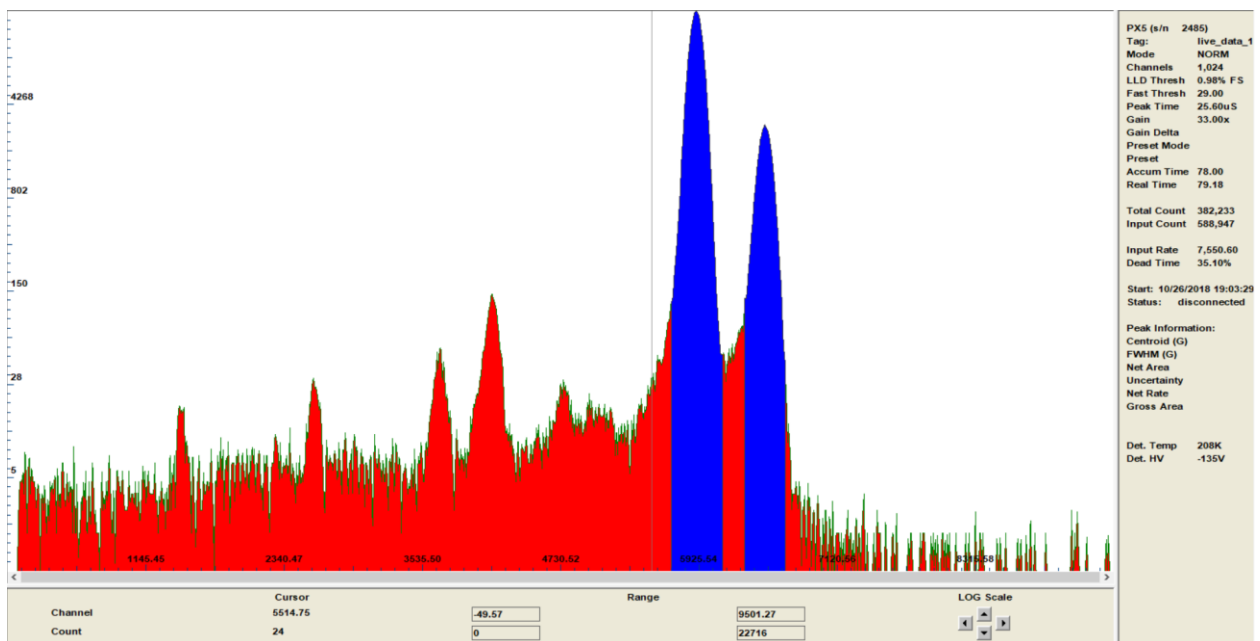
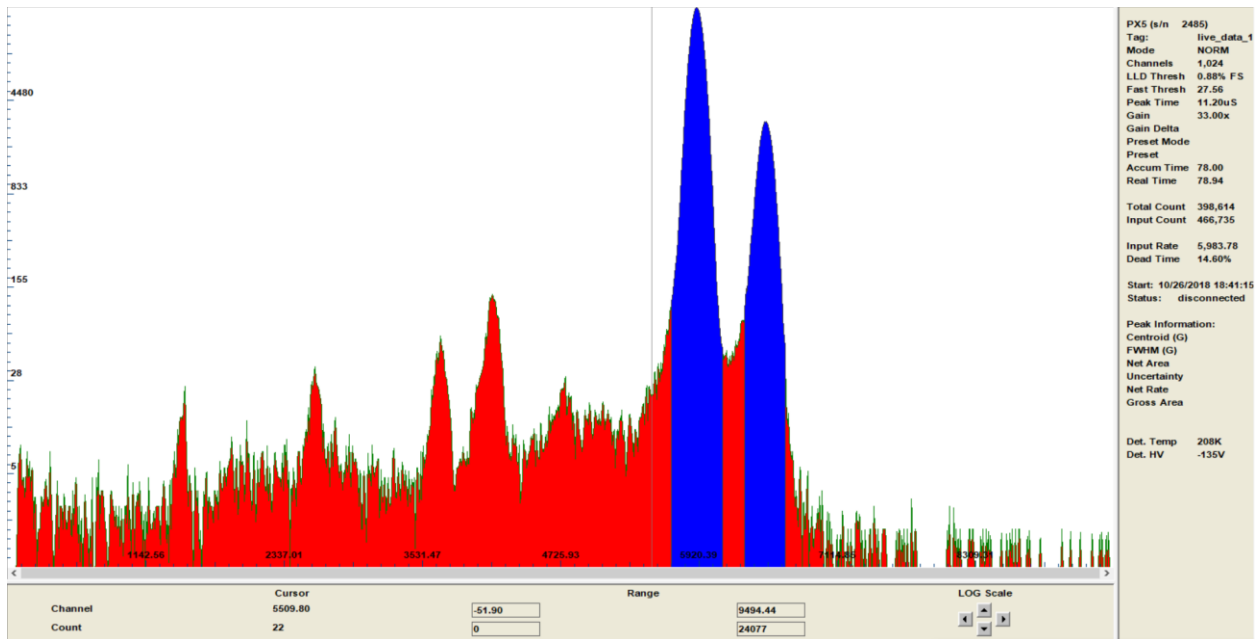


Figure (48). Electronic noise vs. peaking time. [21]



The following  $Fe - 55$  spectrum is peaking time to noise data, the figures are (49) top and (50) bottom.



The following  $Fe - 55$  spectrum is peaking time to noise data, the figures are (51) top and (52) bottom.

The last  $Fe - 55$  data was taken to relate count rate to the dead time of the detector, this data was taken with a peaking time of  $11.2 \mu s$  and at  $78 s$  of acquisition time. The data shows that the highest resolution can be obtained with lower count rates and lower dead times. To get defined peaks, however, the data accumulation time should be longer. The  $Fe - 55$  source was weak and as close as possible to the detector, so a higher count rate could not be achieved, but the data shows that a count rate below  $10000 cps$  keeps the resolution below  $2.2\%$ .

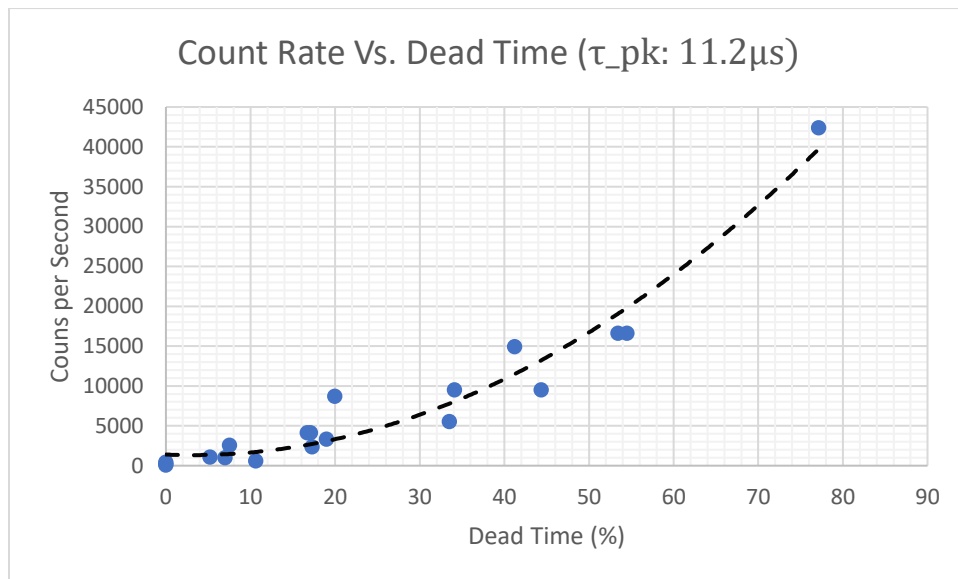


Figure (53). Count Rate Vs. Dead Time (peak time  $11.2 \mu s$ ).

### 3.3 PIXE Spectral Data

During this calibration, Au (Z=79) was used as the standard at which all other spectral data was taken. The gold that was used was a thin foil and was 99.9% pure. All the data was run at 2-2.6 nA and 12 nA at 2 MeV, and at 3 MeV with 1 nA of current. During test runs, the gain was set to 10 (~31 keV full scale) to accommodate the x-ray energies emitted by the other target elements used in the trial.

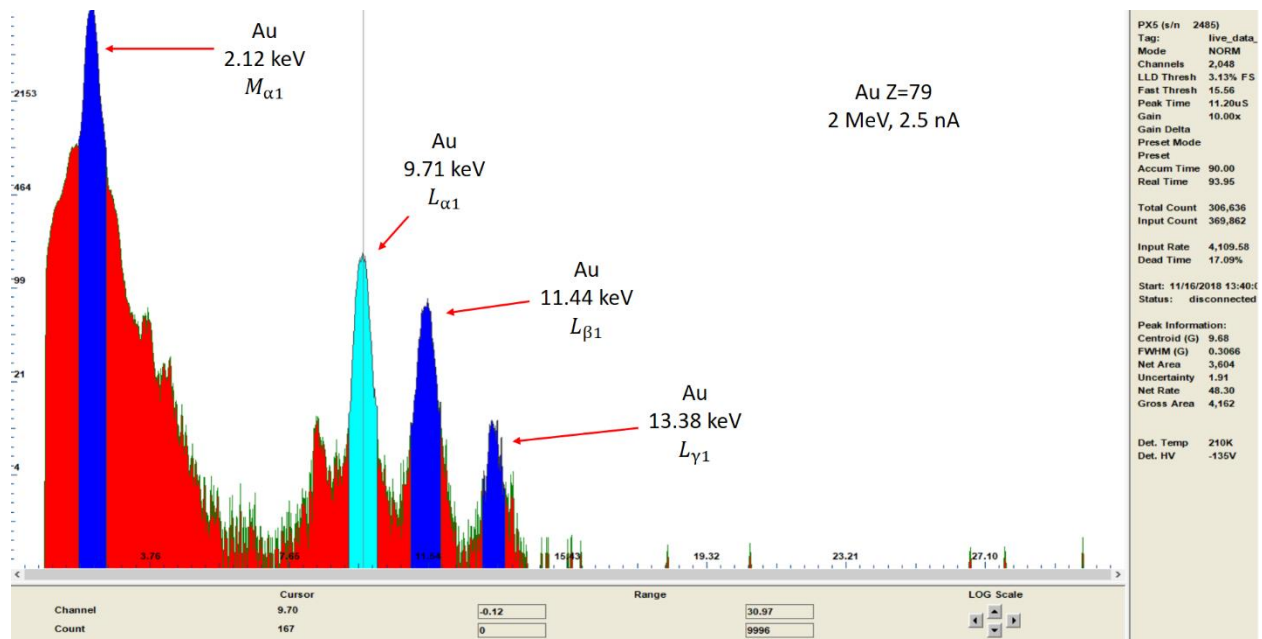


Figure (54). Gold x-ray spectra at 2 MeV with a current of 2.5 nA.

With all three beam settings, specific test elements were accurately identified based on their x-ray spectral lines. Additionally, the energy scale provided with the gold calibration agreed with the peaks produced by all the test elements. Through all three run parameters, simultaneous multi-elemental analysis was verified using a *GaP* (Gallium Phosphide) foil and a thick disk of  $YBa_2Cu_2O_7$ .

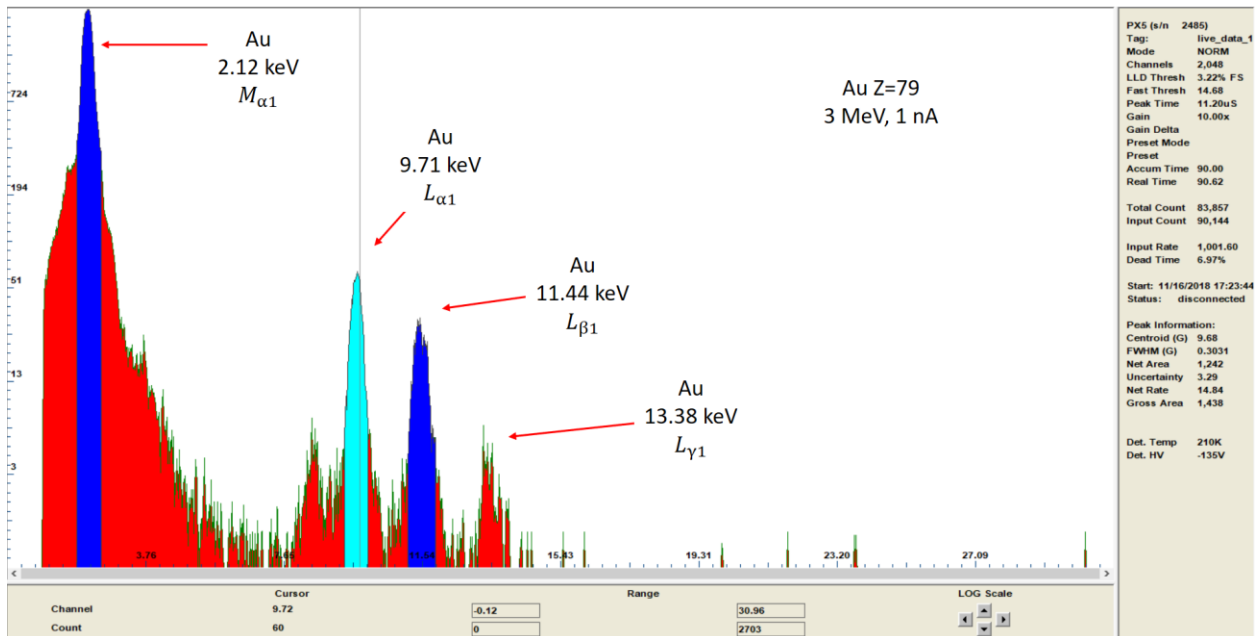
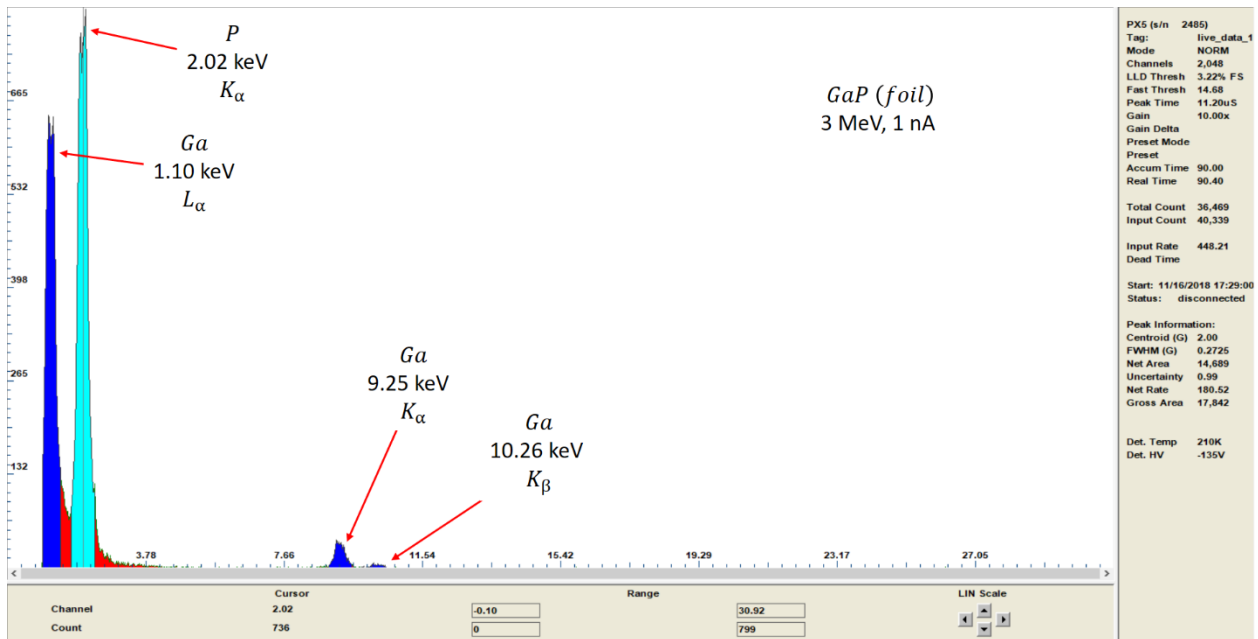
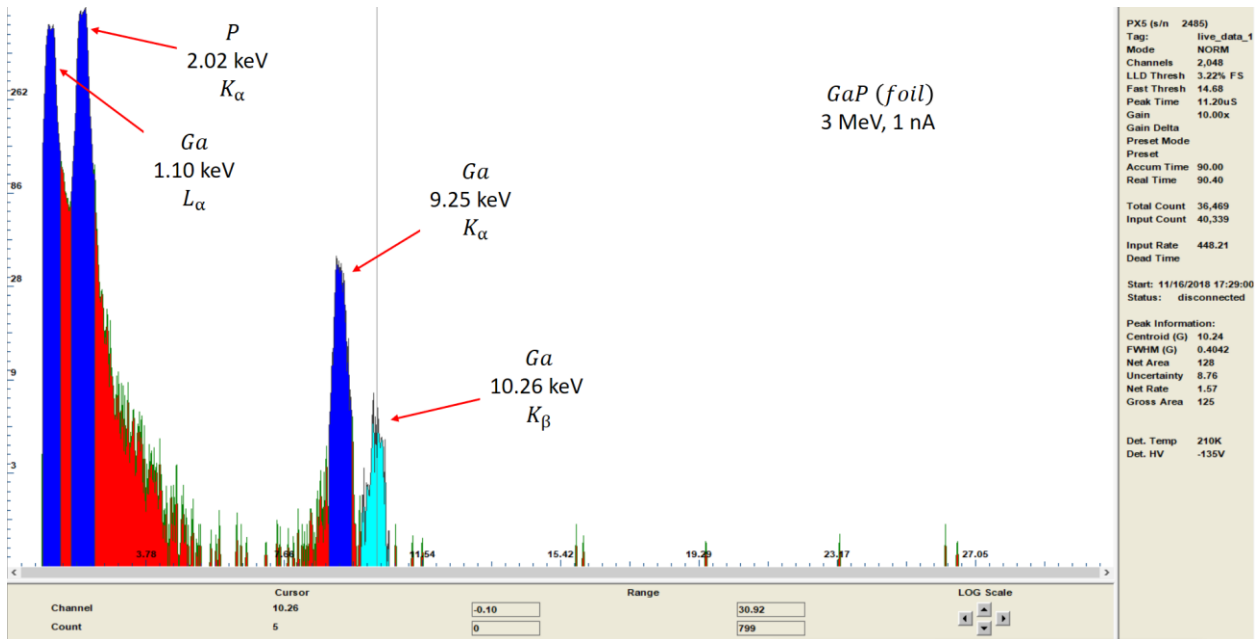
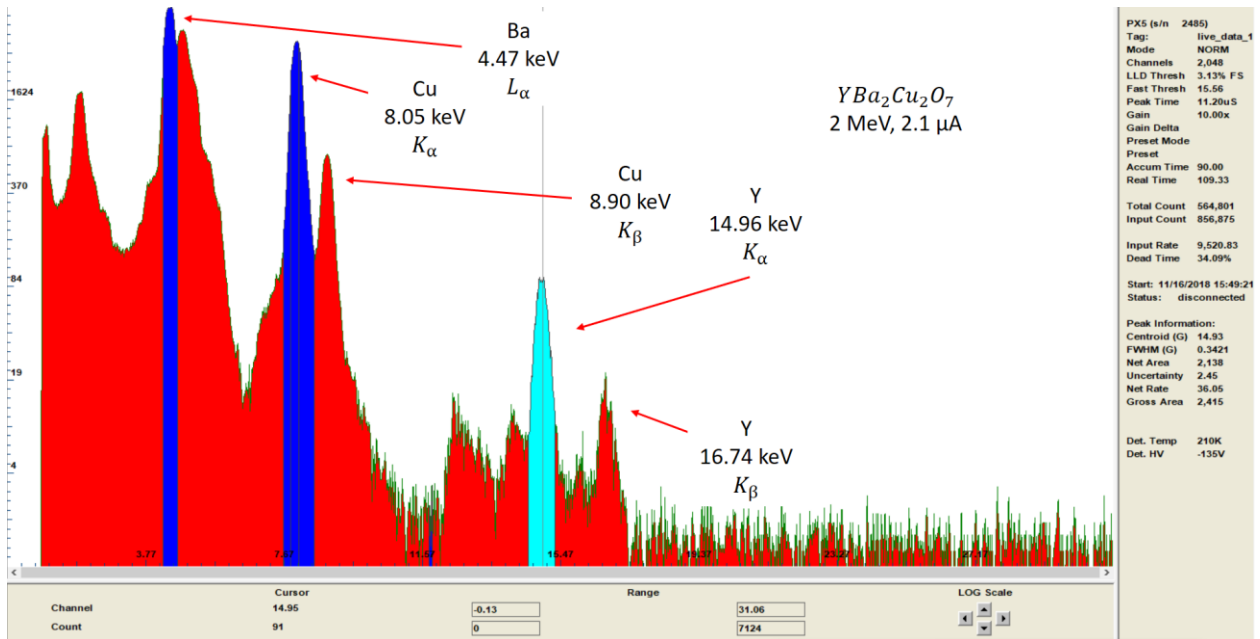


Figure (55). Gold x-ray spectra at 3 MeV with a current of 1 nA.



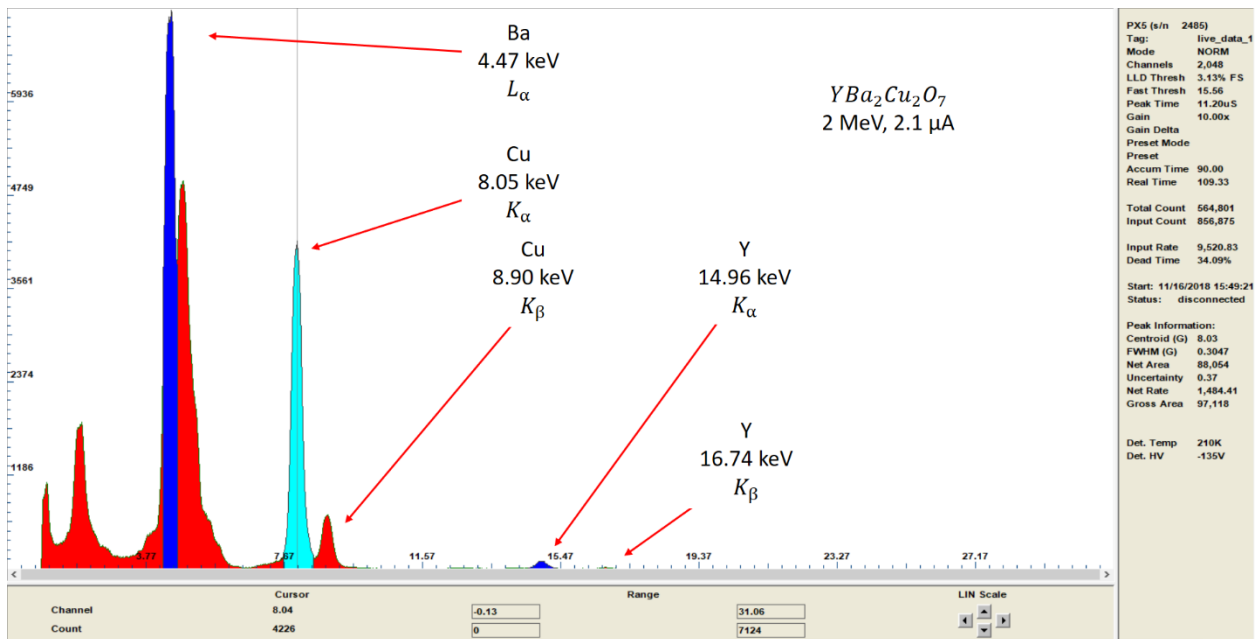
Figures (56) and (57). Gallium Phosphide x-ray spectra at 3 MeV with a current of 1 nA.



PXS (s/n 2485)  
 Tag: live\_data\_1  
 Mode: NORM  
 Channels: 2,048  
 LLD Thresh: 3.13% FS  
 Fast Thresh: 15.56  
 Peak Time: 11.20uS  
 Gain: 10.00x  
 Gain Delta  
 Preset Mode  
 Preset  
 Accum Time: 90.00  
 Real Time: 109.33  
 Total Count: 564,801  
 Input Count: 856,875  
 Input Rate: 9,520.83  
 Dead Time: 34.09%  
 Start: 11/16/2018 15:49:21  
 Status: disconnected

Peak Information:  
 Centroid (G): 14.93  
 FWHM (G): 0.3421  
 Net Area: 2,138  
 Uncertainty: 2.45  
 Net Rate: 36.05  
 Gross Area: 2,415

Det. Temp: 210K  
 Det. HV: -135V



PXS (s/n 2485)  
 Tag: live\_data\_1  
 Mode: NORM  
 Channels: 2,048  
 LLD Thresh: 3.13% FS  
 Fast Thresh: 15.56  
 Peak Time: 11.20uS  
 Gain: 10.00x  
 Gain Delta  
 Preset Mode  
 Preset  
 Accum Time: 90.00  
 Real Time: 109.33  
 Total Count: 564,801  
 Input Count: 856,875  
 Input Rate: 9,520.83  
 Dead Time: 34.09%  
 Start: 11/16/2018 15:49:21  
 Status: disconnected

Peak Information:  
 Centroid (G): 8.03  
 FWHM (G): 0.3047  
 Net Area: 88,054  
 Uncertainty: 0.37  
 Net Rate: 1,454.41  
 Gross Area: 97,118

Det. Temp: 210K  
 Det. HV: -135V

Figures (58) and (59). Superconductor x-ray spectra at 2 MeV with a current of 2.1 nA.

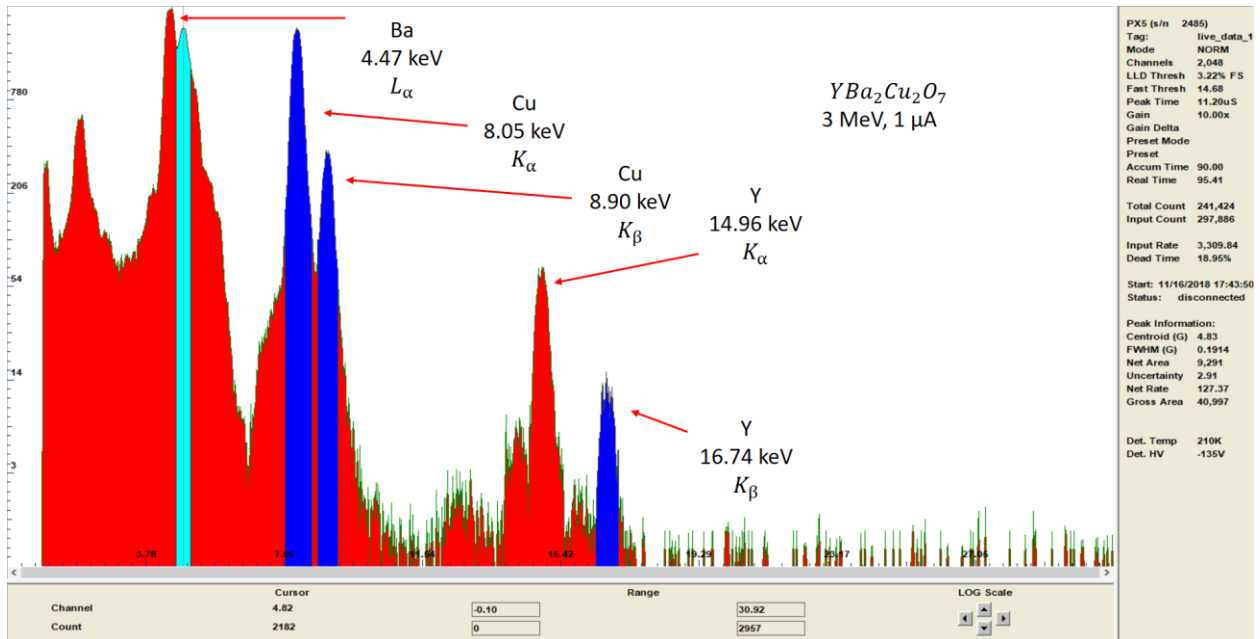
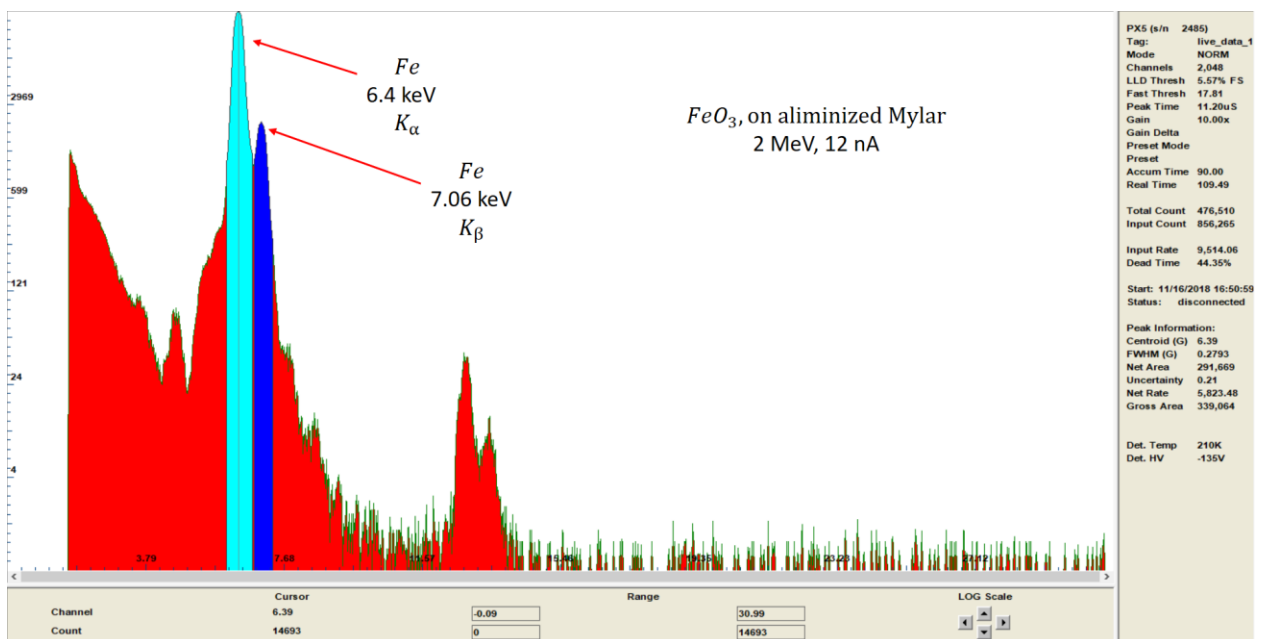
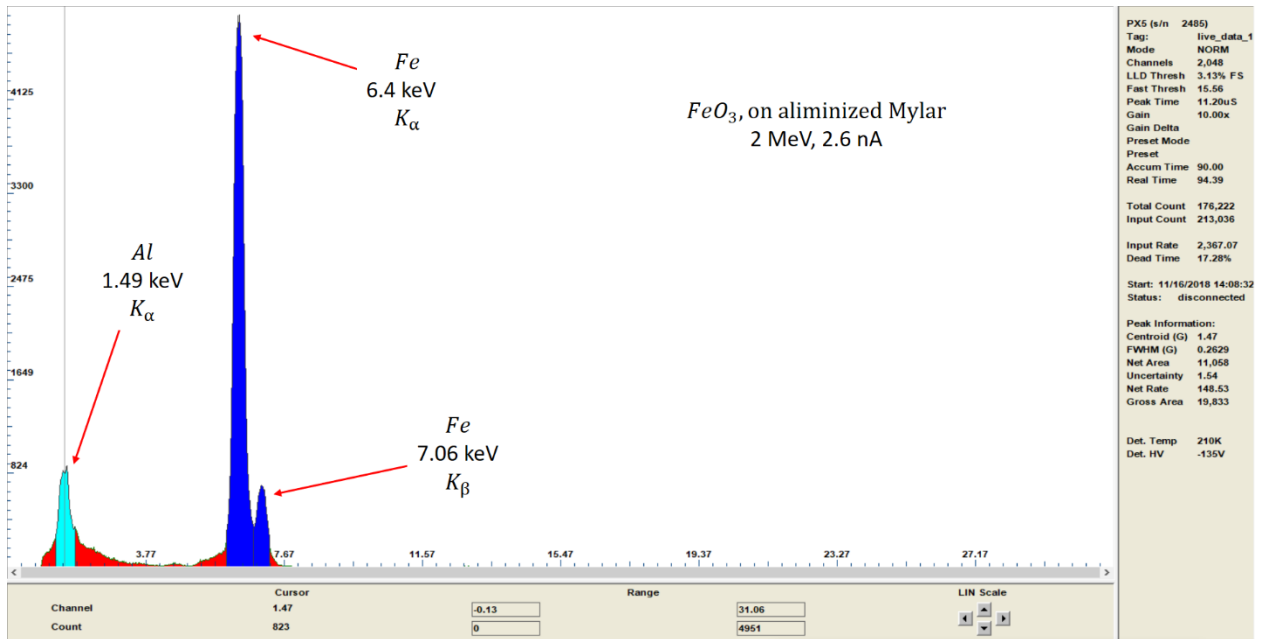


Figure (60). Superconductor x-ray spectra at 3 MeV with a current of 1 nA.



Figures (61) and (62)  $FeO_2$  on Al Mylar.

By comparing the iron oxide data, it is clear that dead time is directly related to beam current, but with the XR-100 Fast SDD detector the results are still acceptable at maximum of 60% dead time.

#### **4. Conclusion**

East Carolina University's Particle Induced X-ray Emission system was redesigned to gather and analyze x-ray spectra generated by the proton irradiation of multielement targets. The x-ray fluorescence spectroscopy system uses a state-of-the-art Amptek XR-100 Fast Silicon Drift Diode detector in conjunction with a digital pulse processor and multi-channel analyzing software. The target analysis chamber can be evacuated below  $10^{-6}$  Torr within a day's time, and it houses a remotely automated 24 position sample changer that can be operated while under vacuum.

ECU's PIXE system was operations checked, calibrated, tested, and operationally verified using known spectral data and reconciling them with known x-ray sources or targets. After this work the PIXE system is to be augmented with GUPIX spectral analysis software.

## 5. References

1. S.A.E. Johansson, in *Particle-Induced X-Ray Emission Spectrometry (PIXE)*, edited by S.A.E. Johansson, J.L. Campbell and K.G. Malmqvist (Wiley, New York, 1995), pp. 1 – 17.
2. J. Chadwick, *The London, Edinburgh, and Dublin Philosophical Magazine and Journal of Science*, **24**, 594 (1912).
3. H.G.J. Moseley, *The London, Edinburgh, and Dublin Philosophical Magazine and Journal of Science*, **26**, 1024 (1913).
4. A. Hadding, *Zeitschrift Für Anorganische Und Allgemeine Chemie*, **122**, 195 (1922).
5. R. Castaing, Ph.D. Dissertation, *Application des sondes electroniques a une methode d'analyse poncuelle chimique et cristallographique*, (University of Paris, 1951).
6. D.M. Khan, D.L. Potter, and R.D. Worley, *Physical Review*, **145**, 23 (1966).
7. D.M. Poole and J.L. Shaw, in *Proceedings of the Fifth International Conference on X-Ray Optics and Microanalysis*, edited by G. Mollenstedt and K.H. Gaukler (Springer Verlag, Berlin, 1969), pp. 319.
8. T.B. Johansson, K.R. Axelsson, and S.A.E. Johansson, *Nuclear Instruments and Methods*, **84**, 141 (1970).
9. S.A.E. Johansson and T.B. Johansson, *Nuclear Instruments and Methods*, **137**, (1976), pp. 473 -- 516.
10. P. Auger, *Journal of Physics*, **6**, 205 (1925).
11. E.H.S Burhop, *The Auger Effect and Other Radiationless Transistions*, (Cambridge University Press, New York, 1952).
12. A.E. Sandtröm, in *Encyclopedia of Physics*, **30**, edited by S. Flügge, (Springer-Verlag, Berlin, 1957), pp. 78.
13. R.W. Fink, *Handbook of Spectroscopy*, edited by J.W. Robinson, (CRC Press, Cleveland, 1974), pp 219.
14. W. Bambynek, B. Crasemaa, R.W. Fink, H.U. Freund, H. Mark, C.D. Swift, R.E. Price, and P. Venugopala Rao, *Review of Modern Physics*, **44**, 716 (1972).
15. A.A. Markowicz, in *Handbook of X-Ray Spectrometry*, edited by R.E. Van Grieken and A.A. Markowicz, (Marcel Dekker, Inc., 1993), pp. 54.
16. W. Brandt and G. Lapicki, *Physical Review A*, **20**, 465 (1979); **23**, 1717 (1981).
17. D.D. Cohen and M. Harrigen, *At Data Nucl. Data Tables*, **3**, 255 (1988).

18. J.L. Campbell, in *Particle-Induced X-Ray Emission Spectrometry (PIXE)*, edited by S.A.E. Johansson, J.L. Campbell and K.G. Malmqvist (Wiley, New York, 1995), pp. 19 – 99.
19. S.A.E. Johansson, *Int. J. PIXE*, **2**, 33 (1992).
20. International Atomic Energy Agency, Instrumentation for PIXE and RBS, IAEA-TECDOC-1190, IAEA, Vienna (2000).
21. Amptek - X-Ray Detectors and Electronics. *FAST SDD® Ultra High Performance Silicon Drift Detector*.
22. J.L. Campbell, R.D. Lamb, R.G. Leigh, B.G. Nickel, and J.A. Cookson, *Nucl. Instr. Meth.*, **B12**, 402 (1985).
23. H. Dahlmann, Q. Fazly, H. Mommsen, and A. Weber, *Nucl. Instr. Meth.*, **B1**, 41 (1984).
24. W. Maenhaut, *Scan. Microsc.*, **4**, 43 (1990).
25. R. Middleton, *A Negative Ion Cookbook* (University of Pennsylvania, 1989).
26. R. Middleton, *Nuclear Instruments and Methods in Physics Research*, **214**, 2-3 (1983), pp. 139-150.
27. R. Middleton, *Nuclear Instruments and Methods in Physics Research*, **220**, 1 (1984), pp. 105-106.
28. *Sputtering by particle bombardment*, edited by R. Behrisch and H.H. Anderson, (Springer, Berlin, 1981).
29. J.A. Ferry, *Nuclear Instruments and Methods in Physics Research Section A: Accelerators, Spectrometers, Detectors and Associated Equipment*, **328**, 1-2 (1993), pp. 28-33.
30. G. Norton, *Pramana*, **59**, 5 (2002), pp. 745-751.
31. R.J. Van de Graaff, *Nuclear Instruments & Methods*, **8**, (1960).
32. *Application Note AN-SDD-003: Amptek Silicon Drift Detectors*. Amptek, INC.
33. *XR-100SDD User's Manual*, Amptek, INC.
34. *Application Note: AN-SDD-001 REV B0*, Amptek, INC.
35. *Detector Efficiency FAQ*, Amptek, INC.
36. *PX5 User Manual Rev A3*, Amptek, INC.

